

Multi-scale structural and kinematic analysis of a Neoproterozoic shear zone in northeastern
Minnesota: Implications for assembly of the southern Superior Province

A DISSERTATION
SUBMITTED TO THE FACULTY OF
UNIVERSITY OF MINNESOTA
BY

Jonathan Dyess

IN PARTIAL FULFILLMENT OF THE REQUIREMENTS
FOR THE DEGREE OF
DOCTOR OF PHILOSOPHY

Vicki L. Hansen

August 2014

UMI Number: 3643607

All rights reserved

INFORMATION TO ALL USERS

The quality of this reproduction is dependent upon the quality of the copy submitted.

In the unlikely event that the author did not send a complete manuscript and there are missing pages, these will be noted. Also, if material had to be removed, a note will indicate the deletion.



UMI 3643607

Published by ProQuest LLC (2014). Copyright in the Dissertation held by the Author.

Microform Edition © ProQuest LLC.

All rights reserved. This work is protected against unauthorized copying under Title 17, United States Code



ProQuest LLC.
789 East Eisenhower Parkway
P.O. Box 1346
Ann Arbor, MI 48106 - 1346

© Jonathan Dyess 2014

Acknowledgements

I would like to extend a large thanks to my advisor Dr. Vicki L. Hansen for being the most knowledgeable and enthusiastic scientists that I have ever had the pleasure of working with. This work would not have been possible without her support, and I would not be the geologist I am today without all of the invaluable guidance and knowledge that she has so generously given over the last four years. To my committee Dr. John Goodge, Dr. Christian Teyssier, and Dr. Carlos Carranza-Torres, I also offer my gratitude and appreciation for many great conversations and well-reviewed manuscripts. Funding for this project came from many sources and covered a variety of field travel and laboratory expenses. Specifically, I would like to thank the McKnight Foundation (funds awarded to Vicki Hansen), the University of Minnesota Duluth Department of Geological Sciences, the Precambrian Research Institute, the Institute on Lake Superior Geology, and the Harry and Margret Walker Foundation for generously funding this research. I would also like to thank the National Forest Service and Ontario Parks Service for allowing me to conduct research within the BWCAW and Quetico Provincial Park. Thanks to my field assistants Chris Goscinak, Evan Elderbrock, Andrew Choquet, and Josh Zoellmer for paddling many miles and carrying large rocks over long portages. Thanks Bryan Bandli for spending long hours working with me on the SEM with some very frustrating samples. To my friends and family back in Texas, thanks for your supporting me through this extended college career. Finally, I would like to express my eternal gratitude to my loving wife Kelli for supporting and encouraging me throughout

the last four years. Without her love and support, this work would not have been possible.

Dedication

This work is dedicated to my loving wife and family, without whose support this research would not have been possible.

Abstract

This dissertation is a multi-scale structural and kinematic analysis of the Shagawa Lake shear zone in northeastern Minnesota (USA). The Neoproterozoic Shagawa Lake shear zone is an ~70 km long ~7 km wide subvertical package of L-S tectonites located within the Wawa Subprovince of the Archean Superior Province. In this dissertation, I (1) discuss a new method for mapping regional tectonic fabrics using high-resolution LiDAR altimetry data; (2) examine the geometric relationships between metamorphic foliation, elongation lineation, vorticity, and non-coaxial shear direction within individual L-S tectonites; and (3) incorporate LiDAR, field, and microstructural data sets into a comprehensive structural and kinematic analysis of the Western Shagawa Lake shear zone. Lastly, I discuss implications for assembly of the southern Superior Province.

In Chapter one I examine an Archean granite-greenstone terrane in NE Minnesota to illustrate the application of high-resolution LiDAR altimetry to mapping regional tectonic fabrics in forested, glaciated areas. I describe the recognition of lineaments and distinguishing between tectonic and glacial lineament fabrics. I use a 1-m posted LiDAR derived bare-earth digital elevation model (DEM) to construct multiple shaded-relief images for lineament mapping with sun elevation of 45° and varying sun azimuth in 45° intervals. Two suites of lineaments are apparent. Suite A has a unimodal orientation, mean trend of 035, and consists of short (> 2 km long) lineaments within sediment deposits and bedrock. Suite B lineaments, which are longer (1-30 km) than those of suite A, have a quasi-bimodal orientation distribution, with maximum trends of 065 and 090. Only one lineament suite is visible in areas where suites A and B are parallel. I interpret

suite A as a surficial geomorphologic fabric related to recent glaciation, and suite B as a proxy for the regional tectonic fabric. Field measurements of regional tectonic foliation trajectories are largely consistent with suite B lineaments across the study area. Although not all suite B lineaments correlate to mapped structures, our analysis demonstrates that high-resolution LiDAR altimetry can be useful in mapping regional tectonic fabrics in glaciated terrane.

In Chapter two I present a detailed kinematic study of seven Neoproterozoic L-S tectonite samples in order to determine vorticity and non-coaxial shear direction relative to foliation and elongation lineation. Samples are from L-S tectonites of the Wawa Subprovince, more specifically the Vermilion District of NE Minnesota, a NE-trending belt of greenschist grade supracrustal rocks and granitoid bodies. Supracrustal rocks host multiple L-S tectonite packages with a well-developed sub-vertical metamorphic foliation and elongation lineation; elongation lineation generally plunges steeply to obliquely although rare zones of shallow plunge occur locally. The Wawa Subprovince is widely interpreted as a transpressional margin with shear zones recording unidirectional dextral strike-slip, an interpretation held up as fundamental evidence for Archean plate-tectonic processes. However vorticity and shear direction within the Vermilion District L-S tectonites remain unconstrained. I compare data from thin-sections, x-ray computed tomography, and quartz crystallographic fabric analysis to monoclinic shear models to determine vorticity and better understand geometric relationships between vorticity, non-coaxial shear direction, foliation, and elongation lineation. Kinematic indicators in thin-section and image slices from X-ray computed tomography consistently record

asymmetric microstructural fabrics in foliation-normal lineation-parallel planes, whereas planes normal to foliation and elongation lineation display dominantly symmetric microstructural fabrics. Mantled porphyroblast 3D-shapes and star-volume distribution analyses indicate that porphyroblast short-axes are normal to foliation and long-axes parallel elongation lineation. Quartz crystallographic preferred orientation data show a-axes maxima sub-parallel to foliation-normal lineation-parallel planes. Kinematic data are consistent with a vorticity axis within the foliation plane and normal to elongation lineation; thus non-coaxial shear direction is sub-parallel to elongation lineation. Data are inconsistent with shear models in which non-coaxial shear direction is normal to lineation, or vorticity axis is normal to foliation. Data indicate that tectonites record non-coaxial shear broadly parallel to elongation lineation regardless of lineation geographic orientation.

In Chapter three I present a detailed structural and kinematic study of the eastern Shagawa Lake shear zone. A subvertical metamorphic foliation strikes NE; elongation lineation forms a splayed orientation distribution; however 70% of elongation lineations pitch $\geq 60^\circ$ to the NE or SW. Strike-parallel elongation lineations occur within localized zones. Non-coaxial shear direction is sub-parallel to elongation lineation. Kinematic indicators record N-side-up and S-side-up shear, and local strike-slip shear—with both right-lateral and left-lateral shear sense recorded. Elongation lineation and kinematic indicators appear consistent within individual outcrops, but can vary significantly between outcrops. I recognize no strain partitioning, crosscutting relationships between multiple shear events, or metamorphic overprinting within the study area. L-S tectonites

record roughly isobaric/isothermal greenschist facies metamorphic conditions across the Shagawa Lake shear zone. The Shagawa Lake shear zone records a broad deformation event characterized by dominantly dip-slip shear in varying directions with multiple shear-senses. Structural and kinematic data indicate that the Shagawa Lake shear zone records deformation within a rheologically weak crust. These data are inconsistent with existing sagduction-diapirism/crustal overturn models and with plate-tectonic/terrane accretion scenarios for assembly of the southern Superior Province. Channel flow induced collapse and exhumation of high-grade crustal material during regional shortening provides a plausible mechanism for assembly of the southern Superior Province and is consistent with the rheological implications of this study.

Table of Contents

Acknowledgements.....	i
Dedication.....	iii
Abstract.....	iv
Table of Contents.....	viii
List of Tables.....	x
List of Figures.....	xi
Introduction.....	1
1. Application of LiDAR to resolving tectonic and glacial fabrics in glaciated terrain: An example from an Archean granite-greenstone belt, NE Minnesota.	
1.1. Introduction.....	7
1.2. Geologic setting.....	8
1.3. Data acquisition.....	9
1.4. LiDAR as a field mapping tool.....	10
1.5. Surface cover types.....	12
1.6. Lineament suites.....	13
1.7. Interpretation of lineament fabrics.....	15
1.8. A new view of the regional tectonic fabric.....	18
1.9. Factors limiting recognition of tectonic fabric in glaciated terrane.....	19
1.10. Suggested methods for lineament mapping.....	21
1.11. Summary.....	23
2. Determination of vorticity in Neoproterozoic L-S tectonites	
2.1. Introduction.....	37
2.2. Background.....	38
2.2.1 <i>Geologic Setting</i>	38
2.2.2 <i>Vorticity within L-S tectonites</i>	39
2.2.3 <i>Techniques for determination of vorticity</i>	41
2.2.3.1 <i>Petrographic microstructural techniques</i>	41
2.2.3.2 <i>X-ray computed tomography (XRCT) techniques</i>	42
2.2.3.3 <i>Quartz crystallographic preferred orientation (CPO) analyses</i>	43
2.3. Sample description.....	44
2.3.1 <i>Sample SB191</i>	44
2.3.2 <i>Sample SB245</i>	45
2.3.3 <i>Sample SB141</i>	46
2.3.4 <i>Sample SB293</i>	47
2.3.5 <i>Sample SB104</i>	48
2.3.6 <i>Sample KS6U</i>	48
2.3.7 <i>Sample KS7J</i>	49

2.4. Determination of vorticity.....	49
2.4.1 <i>Model 1: Vorticity axis parallel to Le and parallel to Fm; VNS normal to Fm and normal to Le.....</i>	50
2.4.2 <i>Model 2: Vorticity axis normal to Le and parallel to Fm; VNS normal to Fm and parallel to Le.....</i>	51
2.4.3 <i>Model 3: Vorticity axis normal to Le and Fm; VNS parallel to Fm.....</i>	53
2.5. Le as a proxy for non-coaxial shear direction.....	54
2.5.1 <i>Lc striations vs Ls lineations.....</i>	54
2.5.2 <i>General shear in sample KS7J.....</i>	55
2.6. Summary and conclusions.....	56
3. Structural and kinematic analysis of the western Shagawa Lake shear zone, NE Minnesota: Implications for assembly of the southern Superior Province	
3.1. Introduction.....	66
3.2. Geologic Setting.....	68
3.3. Shagawa Lake Shear Zone (SLSZ).....	69
3.3.1 <i>Study area.....</i>	70
3.3.2 <i>Kinematic Analysis.....</i>	72
3.4. Discussion.....	80
3.4.1 <i>Western Shagawa Lake shear zone.....</i>	80
3.4.2 <i>Kawishiwi Lake shear zone.....</i>	80
3.4.3 <i>Mud Creek shear zone.....</i>	81
3.4.4 <i>Murray shear zone.....</i>	82
3.5. Implications and evaluation of tectonic models.....	83
3.5.1 <i>Sagduction-diapirism and crustal overturn.....</i>	84
3.5.2 <i>Plate-tectonic/terrane accretion models.....</i>	86
3.5.3 <i>Rheological implications.....</i>	88
3.5.4 <i>Channel flow induced collapse during regional shortening.....</i>	90
3.6. Summary and conclusions.....	92
4. Bibliography.....	105

List of Tables

Table 1.1	LiDAR data acquisition details.....	25
Table 2.1	Sample locations and orientations.....	58
Table 3.1	Microstructural and kinematic data.....	95

List of Figures

Figure 1.1	Simplified geologic map of Minnesota.....	26
Figure 1.2	1-meter resolution shaded-relief image of the study area.....	27
Figure 1.3	Raw DEM vs shaded-relief image.....	28
Figure 1.4	Shaded-relief images at varying sun azimuth.....	29
Figure 1.5	Surface cover types.....	30
Figure 1.6	Lineament fabric maps.....	31
Figure 1.7	Shaded-relief images and lineament map of suite A lineaments.....	32
Figure 1.8	Shaded-relief images and lineament map of intersecting suite A and suite B lineament fabrics.....	33
Figure 1.9	Shaded-relief images and lineament map of parallel suite A and suite B lineament fabrics.....	34
Figure 1.10	Suite B lineaments and corresponding structural trajectories.....	35
Figure 1.11	Interpreted tectonic fabric.....	36
Figure 2.1	Selected subprovinces of the Superior Province.....	59
Figure 2.2	Orientation of L-S tectonite elements in three monoclinic shear models.....	60
Figure 2.3	Photomicrographs of sample SB191 and SB245.....	61
Figure 2.4	Photomicrographs and XRCT slices of sample SB141, SB293, and SB104.....	62
Figure 2.5	3D-surfaces and orientations of porphyroclasts in SB141 generated from BLOB3D.....	63
Figure 2.6	3D-rose diagrams showing relative SVD component magnitudes and eigenvectors representing strain axes generated in QUANT3D for porphyroclasts from SB141.....	64
Figure 2.7	Fm-normal Le-parallel photomicrographs of quartz-rich samples.....	64
Figure 2.8	Quartz c- and a-axis CPO data for KS6U and KS7J.....	65
Figure 3.1	Selected subprovince of the Superior Province.....	96
Figure 3.2	Regional geologic map of the Shagawa Lake shear zone showing regional structural trajectories interpreted from LiDAR altimetry.....	97
Figure 3.3	Geologic map of the study area.....	98
Figure 3.4	Structural elements of an L-S tectonite.....	100
Figure 3.5	Elongation lineation and non-coaxial shear direction pitch domains.....	101
Figure 3.6	Photomicrographs of thin sections cut parallel to the vorticity-normal-section.....	102
Figure 3.7	Schematic diagram of an L-S tectonite showing consistent NW-down shear parallel to Lc.....	103
Figure 3.8	Channel flow induced collapse during regional shortening.....	104

Introduction

Mechanisms governing assembly of the Archean Superior Province remain highly contested. The North American Superior Province is comprised of a series of ENE-trending linear subprovinces with juxtaposed regions of low-grade granite-greenstones against regions of high-grade gneiss and schist. Proposed models for the assembly of the Superior province can be broadly grouped into three categories from older to more recent: (1) plate tectonics scenarios involving accretion of oceanic, volcanic arc, or ocean plume terranes, and/or volcanic arc and/or plume magmatism (e.g., Drury et al., 1984; Windley, 1984; Davis et al., 1988; Card, 1990; Williams, 1990; Desrochers et al., 1993; Kimura et al., 1993; de Wit, 1998; Kusky, 1998; Kusky and Polat, 1999; Lowe, 1999; Daigneault et al., 2002; Chown et al., 2002; Percival et al., 2004); (2) vertical tectonic scenarios involving crustal convective overturn or coupled granitoid diapirism and greenstone sagduction (e.g., Lin, 2005; Parmenter et al., 2006; Bedard et al., 2003, 2006; Harris and Bedard, 2014); and (3) channel flow induced collapse within a ductile lower crust (Perchuk and Gerya, 2011; Harris et al., 2012). Differing models make different predictions with regard to structural and kinematic data, non-coaxial displacement direction, and shear zone vorticity during subprovince assembly. Therefore structural and kinematic histories of shear zones along subprovince boundaries might provide critical clues to the processes responsible for crustal assembly of the Superior Province.

The Vermilion District of NE Minnesota contains multiple shear zones within the Wawa subprovince in close proximity to the boundary between the Quetico and Wawa subprovinces. The subprovince boundary is difficult to locate in the field, and shear

zones exist within the Wawa subprovince. The displacement history of several of these shear zones remains unconstrained. These shear zones generally form NE- to ENE-striking, sub-vertical zones of L-S tectonites with metamorphic foliation generally parallel to their host zone (near vertical with ENE strike) and steep to moderately-plunging elongation lineation. These shear zones have been variably interpreted as recording (1) unidirectional dextral strike-slip shear (Hudleston et al., 1988; Bauer and Bidwell, 1990; Schultz-Ela and Hudleston, 1992) or (2) dominantly dip-slip shear parallel to elongation lineation with local subsidiary strike-parallel shear, with either or both right- and left-lateral shear (Erickson, 2008, 2010; Goodman, 2008, Karberg, 2009; Johnson, 2009). Interpretation of non-coaxial shear direction and shear-sense has first-order implications for mechanisms governing subprovince assembly within the southern Superior Province.

The topic of this contribution is the Shagawa Lake shear zone (SLSZ), an ~70 km-long and ~7 km-wide subvertical package of L-S tectonite, south of, and in close proximity to, the Quetico-Wawa subprovince boundary. Previous studies of the SLSZ, which spatially overlapped in part, arrived at different conclusions from each other, with regard to non-coaxial shear direction and shear-sense. The earlier and spatially more focused study concluded that SLSZ L-S tectonites, defined by a NE-striking subvertical Fm and moderately SW-plunging elongation lineation, record unidirectional dextral shear (Bauer and Bidwell, 1990). In contrast, a more recent study, partially overlapping spatially with the earlier study, but extending further to the east, described a NE-striking subvertical Fm and a fanning in the orientation distribution of elongation lineation

(Erickson, 2008, 2010). Elongation lineation plunge varies from steep, to moderately to the NE, and moderately to the SW; gently-plunging elongation lineation occurs locally. SLSZ L-S tectonites record N-side-up and S-side-up dip- to oblique-shear parallel to elongation lineation with localized left-lateral shear parallel to gently-plunging elongation lineation. These previous studies highlight the need for a detailed examination of the SLSZ; such a study should both focus on L-S tectonite formation, and take a broad regional view of the shear zone.

This dissertation represents a multi-scale structural and kinematic analysis of the SLSZ aimed at understanding the structural architecture and kinematic history of the SLSZ at regional, outcrop, and microscopic scales. Chapter one outlines a new method for application of high-resolution Light Detection and Ranging (LiDAR) altimetry data to resolving tectonic fabrics in forested, continentally glaciated terrain. Chapter two presents a microstructural vorticity analysis of seven Neoproterozoic L-S tectonites from the Wawa subprovince. Chapter three puts the research into a regional context, presents a detailed structural and kinematic analysis of a portion of the eastern SLSZ, and discusses implications for assembly of the southern Superior Province.

The first chapter introduces a new method for application of high-resolution LiDAR altimetry data to resolve tectonic fabrics in forested, continentally glaciated terrain. Tectonic fabrics commonly have an associated topographic expression that may be identified via remote sensing (Chardon et al., 2002, 2008, 2009; Bedard et al., 2003). In glaciated terrains the vegetation, sediment cover, low overall topographic relief, and overprinting of glacial fabrics can variably obscure tectonic topographic expression and

hinder identification via traditional remote sensing data sets such as satellite imagery and aerial photography. Therefore, remote sensing-based approaches to mapping tectonic fabrics in forested, glaciated terrain are commonly not feasible. Airborne LiDAR systems provide high-resolution altimetry in vegetated areas (e.g., Haugerud et al., 2003). However the use of LiDAR altimetry to map regional tectonic fabrics in continentally glaciated terrain remains unexplored. Chapter 1 is a regional structural evaluation of the SLSZ aimed at illustrating the application of high-resolution LiDAR altimetry to mapping regional tectonic fabrics in forested, continentally glaciated regions.

The second chapter presents a vorticity analysis of seven Vermilion District L-S tectonite samples. Five of these samples are from SLSZ and two are from the Kawishawi shear zone, a zone that contains a subvertical metamorphic foliation and a dominantly dip-parallel elongation lineation (Goodman, 2008). As documented within the published literature, in the case of L-S tectonites shear direction and magnitude is genetically linked to vorticity; vorticity can be described within the vorticity-normal-section and/or as a vorticity axis—the pole to the vorticity-normal-section (e.g., Passchier, 1998; Xypolias, 2010 and references therein). However, geometric relationships between shear direction and macroscopic structures, such as foliation and elongation lineation can vary depending on the mechanisms governing L-S tectonite formation (Passchier, 1998). Elongation lineation can occur parallel, perpendicular, or oblique to shear direction during L-S tectonite formation. Therefore robust determination of vorticity within a family of L-S tectonites requires careful consideration before interpretation of shear direction. The determination of the vorticity axis and characterization of the geometric relations

between the vorticity-normal-section, foliation, and elongation lineation can allow for the use of foliation and elongation lineation as an indicator for non-coaxial shear direction during L-S tectonite formation. In chapter two, the vorticity axis for seven L-S tectonites is determined using a combination of petrographic microstructural, X-Ray Computed Tomography (XRCT), and quartz crystallographic preferred orientation data. These data both collectively and individually indicate that in all cases the vorticity-normal-section lies within the foliation-normal elongation lineation-parallel plane and that the displacement direction is sub-parallel to elongation lineation, regardless of elongation lineation geographic orientation of individual samples. There is no evidence for non-coaxial displacement within the plane normal to foliation and normal to elongation lineation. This vorticity analysis is fundamental to understanding the kinematic history of the eastern SLSZ.

The third chapter presents a detailed structural and kinematic analysis of a portion of the eastern SLSZ, and places the SLSZ into a tectonic context based on the results of the kinematic data. Key questions include: (1) What displacement direction and shear-sense(s) are recorded in the eastern SLSZ? (2) Does the SLSZ record unidirectional shear or multiple shear-senses? (3) Does the SLSZ record over-printing or cross-cutting relationships between multiple shear events? Foliation and elongation lineation orientation measurements combined with microstructural kinematic data and the results from the previous vorticity analysis (chapter 2), indicate that the SLSZ records a broad deformation event characterized by dominantly dip-slip shear in varying directions with multiple shear-senses. Structural and kinematic data indicate that the Shagawa Lake

shear zone records deformation within a rheologically weak crust. In light of this new data, existing tectonic models are evaluated and implications of these results for assembly of the southern Superior Province are discussed.

Understanding the kinematic history of the eastern SLSZ is necessary to evaluate proposed tectonic models for assembly of the southern Superior Province. The conclusion that non-coaxial shear direction is parallel to elongation lineation combined with the steeply plunging elongation lineation data presented in chapter three indicates that the eastern SLSZ records a broad dip-parallel shear. There is no evidence for dominantly right-lateral strike-parallel shear. Steep to obliquely plunging elongation lineations from other Vermilion District shear zones indicate that broad dip-parallel shear is not limited to the eastern SLSZ (Erickson, 2008, 2010; Goodman, 2008; Karberg, 2009; Johnson, 2009). Existing plate tectonic models requiring the formation of unidirectional strike-slip shear zones either within subprovinces or along subprovince boundaries are inconsistent with structural and kinematic data presented in this dissertation. Vertical tectonic models requiring the formation of L-S tectonite with a consistent granitoid-up/greenstone-down shear sense are also inconsistent with structural and kinematic data presented herein. Assembly of the southern Superior Province by channel flow induced collapse during regional shortening is consistent with structural and kinematic recorded by the eastern SLSZ.

1. Application of LiDAR to resolving tectonic and glacial fabrics in glaciated terrain: An example from an Archean granite-greenstone belt, NE Minnesota.

1.1. Introduction

Regional tectonic fabrics commonly define the broad structural architecture of an area. Tectonic fabrics commonly have an associated topographic expression that may be identified via remote sensing (Chardon et al., 2002, 2008, 2009; Bedard et al., 2003). In glaciated terrains the vegetation, sediment cover, low overall topographic relief, and overprinting of glacial fabrics can variably obscure tectonic topographic expression and hinder identification via traditional remote sensing data sets such as satellite imagery and aerial photography. Therefore, mapping tectonic fabrics in glaciated terranes commonly does not lend itself to rapid, remote sensing-based approaches. A remote sensing method for mapping regional tectonic fabrics within and across glaciated terranes could prove valuable in providing a regional structural framework, complimenting and expediting subsequent field mapping.

Airborne LiDAR (light detection and ranging) systems provide high-resolution altimetry in vegetated areas (e.g., Haugerud et al., 2003). Widespread geoscience applications of airborne LiDAR involve mapping of geomorphic features (typically beneath dense vegetative cover) including landslides, stream channels, alluvial fans, and fault scarps (e.g., Haugerud et al., 2003; Collins and Sitar, 2008; Roering, 2008; Notebaert et al., 2009). Applications of LiDAR altimetry in structural geology include identifying structural fabrics via analysis of (1) morphometric features (e.g., slope, aspect, and curvature) (Wallace et al., 2006) and (2) via analysis of micro-topography

(e.g., Pavlis and Bruhn, 2011). However the use of LiDAR altimetry to map regional tectonic fabrics in continentally glaciated terrain remains unexplored.

In this contribution, I examine a portion of an Archean granite-greenstone terrane in NE Minnesota (USA), and illustrate the application of high-resolution LiDAR altimetry to mapping regional tectonic fabrics in forested, continentally glaciated regions. I discuss lineament recognition using LiDAR and distinguish between tectonic and glacial lineament fabrics. I also discuss potential applications and LiDAR data limitations.

1.2. Geologic setting

The study area is within the within Vermilion District granite-greenstone terrane of northeastern Minnesota (Fig. 1.1). The Vermilion District includes from, north to south: the Vermilion Granitic Complex, various greenschist facies metavolcanic and metasedimentary sequences, and the quartz monzonite Giant's Range Batholith (Sims, 1976). Granite, granite-rich and biotite-rich migmatites, biotite and amphibolite schists, metagabbro, metabasalt, and trondhjemite characterize the Vermilion Granitic Complex. Greenschist facies metavolcanic and metasedimentary sequences, which include protoliths of basalt, diabase, pyroxenite, basalt flows, felsic to intermediate volcanic tuff, felsic volcanic rocks, conglomerate, graywacke, shale, and banded iron formation are cut by ovoid granitoid bodies (Sims, 1976). Volcanic and plutonic rocks range in age from 2.75 to 2.69 Ga and from 2.74 to 2.65 Ga, respectively (Card, 1990 and references therein). Paleoproterozoic plutonic rocks intrude along the southeastern margin of the study area (Gruner, 1941; Jirsa and Miller, 2004).

The Vermilion district volcano-sedimentary sequence hosts several ENE-striking

subvertical ductile shear zones. These shear zones extend up to ~70 km long and with width of 7-10 km, although shear zone boundaries are diffuse. An anastomosing metamorphic foliation is present across the shear zones with an average orientation of 065, 90 (Bauer and Bidwell, 1990; Erickson, 2008, 2010; Wolf, 2006; Goodman, 2008). Layering, where notable, is parallel to local foliation. Narrow areas of well-developed C-foliation mark high strain zones typically parallel to the regional foliation (Bauer and Bidwell, 1990; Wolf, 2006). High strain zones have been recognized locally within an individual shear zone and may exist throughout the various zones; however, the extent of these high strain zones remains unconstrained (Bauer and Bidwell, 1990; Wolf, 2006). High strain zones, ~1.5 km apart, are postulated to accommodate significant deformation relative to areas containing only the regional foliation.

The study area is part of the Superior Uplands geomorphic province, a glacially scoured peneplain characterized by level-to-rolling uplands and hills (McNab and Avers, 1994). Dense coniferous and deciduous forests cover the study area in addition to numerous swampy areas and lakes. Glacially scoured bedrock with areas of thin till or other sediments dominates the surficial geology of the study area. Glacial geomorphologic features include flutes, drumlins, and eskers (Hobbs and Goebel, 1982; Sharp, 1953).

1.3. Data acquisition

In 2011 LiDAR altimetry data were collected over the study area as part of the Minnesota Elevation Mapping Program (Fig.1.2). Data were collected during leaf-off conditions to maximize beam penetration. Full data acquisition details are provided in

Table 1. The principle products of the LiDAR survey were classified LAS formatted point cloud data, a 1-m digital elevation model (DEM), and edge of water breaklines. Secondary products produced by the Minnesota Department of Natural Resources include 2 ft (~0.6 m) topographic contours and building outlines. The LiDAR derived 1-m filtered bare-earth DEM, based on last return data, is the primary raw data set for this study. A pixel resolution of 1 m coupled with sub-meter vertical accuracy allowed for the detection of relatively small-scale topographic features.

1.4. LiDAR as a field mapping tool

In order to determine an efficient way to recognize linear features, I analyzed the raw data in three different forms using ESRI ArcGIS™ software. I analyzed the original bare-earth DEM and LiDAR-derived shaded-relief images, and draped the shaded relief images over the DEM to create 3D-perspective views of the field area. Linear ridges, valleys, shorelines, islands, or elongate ellipsoidal hills define topographic lineaments; I map lineaments by tracing these features or associated long axes. Due to the subvertical nature of the regional structural architecture of the study area, certain lineaments may represent structural trends. This analysis would be inappropriate for areas dominated by gently dipping structures.

Lineament mapping is an iterative process and need not be completed in the sequence described below. Lineament identification was done manually, and in order to recognize lineaments within a given area, it is best to repeatedly analyze areas using all available forms of the data. Lineament mapping was conducted at multiple scales, ranging from a regional scale (~1:250,000) to a single DEM tile (~1:24, 000). The goal

of this analysis was to identify lineaments of any orientation and observe what patterns or subsets naturally emerged. First author, Jonathan Dyess, carried out lineament mapping for this study.

I initially created a single DEM mosaic covering the entire study area; however due to the large size of the study area and high resolution of the data, I opted to create three smaller mosaics in order to reduce file size and processing time. I applied a stretched color ramp to the data utilizing both grayscale and full color symbolization. Full color symbolization revealed more linear features than grayscale. Within the DEM visible lineaments commonly correspond with shorelines, cliffs, and ridges (Fig. 1.3a). Pronounced lineaments correspond to features with relatively high topographic relief; however subtle topographic features are obscured and many small-scale lineaments are not easily visible in the DEM (Fig. 1.3a).

I next constructed shaded-relief images from the original DEM (Fig. 1.3b). A shaded-relief image is a raster image showing changes in elevation using light and shadows on terrain based on a given sun-azimuth and sun-elevation (Zhou, 1992). Sun-azimuth and -elevation are critical to lineament mapping using shaded-relief images. Shaded-relief images may be created for any sun-azimuth or -elevation, even unnatural sun-azimuths, which may reveal subtle topographic features not visible in the bare-earth DEM (Henderson et al., 1996; Pavlis and Bruhn, 2011). Lineaments that trend perpendicular to the sun-azimuth are easily visible whereas lineaments that trend parallel to the sun-azimuth are obscured (Fig. 1.4). Relatively small lineaments that trend parallel to the sun-azimuth were commonly obscured to the point of being invisible, and the

recognition of relatively large lineaments in this same trend was greatly reduced. In order to recognize all orientations of lineaments, I constructed shaded relief images for sun-azimuths that varied from 315 to 090 at 45° increments (Fig. 1.4). I examined shaded-relief images with both equalized and unequalized histogram symbolizations. Images with equalized histogram symbolization emphasize relatively large-scale lineaments. Relatively small lineaments within topographically high areas were commonly obscured by highlights within the image. Images with unequalized histogram symbolization commonly captured small-scale lineaments.

In order to better visualize the topographic surface in 3D, I draped shaded relief images over the bare-earth DEM using ESRI ArcScene™ to create a 3D-perspective view (e.g., Pavlis and Bruhn, 2011). Due to the overall low topographic relief across the study area, I applied both 5x and 10x vertical exaggeration to the DEM. Within these oblique views, lineaments appear pronounced with vertical edges; however vertical faces hide structural elements. Surficial features are easily visible within these oblique views.

1.5. Surface cover types

Visible within the shaded-relief images are two surface cover types, each with a distinctive LiDAR signal (Fig. 1.5). Cover-types were recognized and mapped during the lineament-mapping process. Cover type-I (CTI) comprises the vast majority of study area and occurs as bulbous, irregular topographic surface containing various linear and irregular shaped features. Cover type-II (CTII) occurs in elongate patches across the study area and contains relatively smooth topography compared to CTI. Boundaries between CTI and CTII vary from sharp to gradational. At gradational boundaries,

topographic features consistent with CTI are visible beneath CTII, indicating that CTII overlies CTI. This relationship is consistent across the study area. Ground truthing indicates that CTI correlates to areas of scoured bedrock. Long-axis orientations of CTII patches are consistent with long-axis orientations of drumlins (Hobbs and Goebel, 1982); therefore I interpret CTII as areas of glacial sediment cover.

1.6. Lineament suites

Lineament fabrics visible within LiDAR altimetry are inherently geomorphic fabrics. Both pre-existing bedrock structure and erosion processes effect the formation of geomorphic linear features. Lineaments may be surficial (i.e., dominantly controlled by erosion processes) or structural (i.e., dominantly bedrock controlled). Both surficial and structural lineaments are geomorphic features; however surficial lineaments need not reflect the underlying bedrock geologic structure. Structural lineaments may represent the surface expression of a host of planar geologic structures including: bedding, faults, fractures, foliation, or cleavage. Based on lineament shape characteristics, I classify lineaments into different suites and interpret these suites as either surficial or structural. By extracting structural lineaments, I delineate the structural fabric, which can provide insight into the geologic history of the area.

I recognize two distinct lineament suites. I base lineament classification on length, spacing, orientation, regional pattern, and the type of topographic feature defining the lineament. Classification considers all criteria rather than emphasizing an individual criterion. Lineament spacing was calculated by measuring intersection points along transects across representative areas. Both lineament mapping and lineament

classification are iterative processes with the best result emerging after multiple cycles of mapping and classification.

Lineament suite A (Fig. 1.6a) consists of a series of straight, short, parallel lineaments commonly located within topographically high areas. Elongate, rounded hills and narrow elongate valleys define suite A lineaments and range from 50 to >100 m across and 0.02 to 2.5 km long. Suite A lineaments have variable spacing (ranging from ~0.1 to 2 km) and unimodal orientation distribution with a mean trend of 035 (Fig. 1.6a). Areas of sediment cover contain only suite A lineaments at increasingly smaller scales (Fig. 1.7). Suite A lineaments are most visible within sediment cover with the shortest lineaments having lengths of 20 m. A set of narrow curvilinear features occurs within suite A (Fig. 1.6a). These features can be as long as 3.5 km long and approximately parallel the dominant trend of suite A lineaments (Fig. 1.6a).

Lineament suite B forms a pattern of roughly parallel continuous curvilinear features that commonly bound topographically high areas and have varying trend (Fig. 1.6b). Curvilinear shorelines, cliffs, ridges, valleys, and elongate islands define suite B lineaments, and range in length from <1 to 33 km. Linear features may extend for tens of kilometers as a single lineament, or occur as a series of short parallel segments. Suite B lineament trends range from 000 to 110 and show a weakly bimodal orientation distribution with a dominant trend of 065, and a subsidiary trend of 090 (Fig. 1.6b). The suite B lineament fabric includes domains of pervasive parallel lineaments, spaced parallel lineaments, and spaced lineaments with no apparent preferred orientation.

In regions where suite A and B lineaments occur at high angles, a distinctive interference pattern results (Fig. 1.8). In a shaded-relief image with suite A and suite B lineament fabrics and the corresponding lineament map, suite A lineaments grade from well-developed in the west to poorly-developed to nonexistent in the east. Although suite A lineaments do not occur ubiquitously across the area, suite A lineaments consistently define a parallel fabric within topographically high areas. Conversely, suite B lineaments commonly bound topographically high areas and define a relatively spaced fabric. Where both lineament suites trend at relatively high angles to one another, suite A lineaments occur in topographically high areas between individual suite B lineaments (Fig. 1.8).

Where suite A and B lineaments trend parallel to one another, differentiating the lineament sets is difficult. Figure 1.9 shows a shaded relief image and corresponding lineament map; here suite B lineaments trend 050 and a set of nearby suite A lineaments trend 045. Along the SE margin of the image, a single pervasive lineament set trends 050. These lineaments are classified as suite B due to topographic expression and length. However, given that suite A and B lineaments are nearly parallel, it is likely that some suite A lineaments occur within areas dominated by suite B lineaments (Fig. 1.9). Along the NW edge of the image, the angle between suites A and B is 35° , resulting in an interference pattern of relatively pervasive suite A lineaments between relatively spaced suite B lineaments.

1.7. Interpretation of lineament fabrics

I interpret suite A lineaments as reflecting topographic features related to glaciation. Suite A lineaments appear in both areas of sediment cover and exposed bedrock; however areas with interpreted lineated sediment cover contain only suite A lineaments, and lineaments are continuous across the sediment-bedrock interface (Fig. 1.7). Suite A lineaments commonly parallel mapped glacial flutes and drumlins (Hobbs and Goebel, 1982)(Fig. 1.6a). I interpret the narrow sinus ridges as eskers; these features trend roughly parallel to suite A lineaments. Suite A lineaments are relatively consistent in length, spacing, and orientation across the study area regardless of the underlying bedrock geologic structure. This relationship implies that bedrock geologic structure is not the dominant control on suite A lineament orientation. I interpret suite A lineaments as a surficial geomorphic fabric controlled dominantly by glaciation and erosion.

Suite A lineaments do not always parallel glacial features recognized in the field. For example, in Figure 1.6a, glacial flutes trend 055 and 060 at locations iii and iv respectively (Hobbs and Goebel, 1982) whereas suite A lineaments trend 025; at locations iii and iv the lineaments are relatively long and continuous, and correspond to topographic features with relatively high relief compared to typical suite A lineaments. I interpret these lineaments as suite B lineaments accentuated by glaciation.

Suite B lineaments commonly correlate with structural trajectories of bedrock tectonic fabric (Fig. 1.10)(Bauer and Bidwell, 1990; Goodman, 2008; Erickson, 2010; Mulvey et al., 2009; Jirsa et al., 2011). Structures parallel to suite B lineaments include bedding, metamorphic foliation, and faults; however some parts of the suite B lineament fabric may correlate well with structural trajectories. I divide the suite B lineament fabric

into domains based on lineament orientation and density used for illustrative purposes only (Fig. 1.10a); domain boundaries are approximate with no apparent geologic significance. Figure 1.10 shows a portion of the suite B lineament fabric and the corresponding structural trajectories. Closely spaced, pervasive, parallel suite B lineaments mark domains U, V, and W and correlate well with bedding, metamorphic foliation, and fault trajectories collectively. The dominant structural trend in domain U is 065; lineaments trend east and southeast in domains V and W, respectively.

Domain X is largely devoid of lineaments; in this region, conglomerate, sandstone, and shale dominate the local geology and primary structures (sedimentary bedding) are prevalent, whereas mapped secondary structures (i.e. faults and metamorphic foliation) are rare to nonexistent (Fig. 1.10b) (Mulvey et al., 2009). This inverse correlation between suite B lineaments and bedding trajectory implies that bedding orientation has little effect on suite B lineament orientation, at least at this location. Spaced lineaments characterize domain Y, which also records few secondary structures.

Intersecting lineaments with no apparent preferred orientation characterize domain Z (Fig. 1.10a). These lineaments show no correlation with previously recognized primary or secondary structures, however it is possible that other secondary structures (e.g. fractures) control suite B lineament orientation within domain Z. Due to the close correlation between parallel suite B lineaments and secondary structural trajectories, I interpret areas of parallel suite B lineaments as representing the secondary structural

(tectonic) fabric across the study area. I recognize a correlation between parallel suite B lineaments and secondary structures in nearby areas as well (Figs. 1.10c and 1.10d).

1.8. A new view of the regional tectonic fabric

Using suite B lineament fabric in conjunction with field data, I interpret the tectonic fabric across the study area and present a 2D-representation of the regional tectonic fabric (Fig. 1.11). The lack of 3D information is a function of the overall low topographic relief and the dominant subvertical orientation of geologic structures. The regional tectonic fabric represents a structural continuum with gradational variation in orientation and density. Although individual lineaments do not correspond one-for-one with individual structures, the patterns within the lineament fabric track regional foliation trajectory and allow for first-order observations. The regional tectonic fabric is dominantly within and parallel to metavolcanic-metasedimentary sequence boundaries. I distinguish three types of areas within the tectonic fabric: pervasive parallel fabric, spaced parallel fabric, and intersecting fabric. Regions of pervasive parallel fabric form a curvilinear zone across the study area and, based on field observations, correspond with areas of well-developed metamorphic foliation and faults (Fig. 1.11). Regions of spaced parallel fabric correspond with weakly developed metamorphic foliation and a small number of faults, whereas areas of intersecting lineaments do not correspond to any recognized structures, although field access to this area is limited. I interpret areas of pervasive parallel tectonic fabric to represent the extent of shear zones within the metavolcanic-metasedimentary sequence, and areas of spaced lineaments to represent massive to weakly deformed rock.

Interaction of the tectonic fabric with granitoid bodies has implications for the relative timing between deformation and granitoid emplacement. The tectonic fabric is parallel to granitoid boundaries, and excluding the Giant's Range batholith, granitoids are largely devoid of any tectonic fabric (Fig. 1.11). Tectonic fabric commonly diverges around ovoid granitoids, such as around the Snowbank Lake stock, and near the Saganaga tonalite, particularly along the western margin (Fig. 1.11). One interpretation is that granitoids were at least partially emplaced and rheologically strong before formation of the tectonic fabric and that these bodies did not accommodate much (if any) deformation. Alternatively, granitoid emplacement could post-date formation of the tectonic fabric and simply reorient the tectonic fabric. Tectonic fabric appears continuous across the northern margin of the Giant's Range batholith and fades to the south, suggesting that the northern edge of the Giant's Range batholith underwent some amount of solid-state deformation (Fig. 1.11). These differences may be due to the relatively large size of the Giant's Range batholith compared to the Saganaga tonalite and Snowbank stock (Fig. 1.1).

1.9. Factors limiting recognition of tectonic fabric in glaciated terrane

LiDAR shaded-relief images provide a spectacular view of the study area despite ubiquitous vegetative cover. These data provide substantial improvements over aerial photographs and satellite imagery in recognizing bedrock structure. LiDAR shaded-relief images clearly show areas of scoured bedrock and glacial sediment deposits. Sediment cover significantly limits the usefulness of this analysis. All lineaments interpreted as related to tectonic fabric occur within areas of glacially scoured bedrock with effectively

no sediment cover. Significantly large and/or thick glacial deposits will completely obscure the tectonic fabric.

Topographic expression of the tectonic fabric is a function of lithology, geologic structure, and erosion processes. Although LiDAR altimetry records high-resolution topography that may reflect changes in lithology or geologic structures, the rock's ability to form relatively small-scale topography (microtopography) is critical.

Microtopography is the product of relatively delicate water and wind erosion processes that are sensitive to subtle lithologic and/or structural changes (e.g., Pavlis and Bruhn, 2011). Bedrock in the study area underwent glacial scouring and frost wedging; such erosion processes destroy microtopography and result in a relatively coarse topographic surface.

Detailed LiDAR mapping is difficult due to the relatively coarse topography; however regional structural trends and structural zones emerge from the data. For a structural zone to be visible in the LiDAR shaded-relief image, the zone must be large (wide) enough for the rock to preserve a distinct lineament fabric. Relatively narrow structural zones may appear as a single lineament or not at all. In addition, if a narrow structural zone (defined by a single lineament) is sub-parallel to the surficial glacial lineament fabric, distinguishing the non-glacial lineament from the glacial lineament fabric is difficult to impossible. At the outset of this analysis, two major goals were to use LiDAR altimetry to distinguish structural relationships between the tectonic fabric and granitoids and to identify and map high-strain zones (e.g. Bauer and Bidwell, 1990; Wolf, 2006). Although some structural relationships between the tectonic fabric and

individual granitoids are visible, identification of relatively narrow high-strain zones is difficult.

1.10. Suggested methods for lineament mapping and interpretation

First and foremost, lineament mapping is an iterative process. In this study, lineament identification was done manually, and no single image (DEM, shaded-relief, ect.) effectively captured all lineaments within a given area. Repeated mapping using as many images and symbologies as possible yielded the best results. Although no single method applies perfectly to every study area, I outline a suggested mapping method for recognizing lineaments at any orientation.

Depending on the size of the study area, mosaics of individual DEM tiles may be required. Because various shaded-relief images might be constructed and compared, creating a mosaic of the original LiDAR DEM is, perhaps most time efficient; however the need for mosaics is dependent on computer processing power and software. For this study, dividing the study area into smaller mosaic subsets reduced individual file size and decreases the required processing power and time. Future studies using different software or enhanced computing power may not require this step.

LiDAR shaded-relief images provide an efficient means of lineament recognition. Because lineament mapping requires many different shaded-relief images, careful attention to data processing is critical. Lineaments perpendicular to sun azimuth are most visible whereas lineaments parallel to sun azimuth appear obscured. I found that creating multiple shaded-relief images by varying sun azimuth in 45° increments with a sun elevation of 45° to be a good starting point. After some initial mapping, other shaded-

relief images may be created to investigate specific areas and lineament patterns. Examination of both equalized and non-equalized histogram shaded-relief images is useful. Equalized histogram symbolization highlights relatively large-scale lineaments whereas non-equalized histogram symbolization highlights relatively small-scale lineaments. Mapping in ESRI Arcmap™, or similar geographic information system software, accommodates this mapping method quite well because the original DEM and all subsequent shaded-relief images are georeferenced and can be overlain easily. Shaded-relief images with different sun azimuths can be turned on or off during mapping, quickly providing multiple views of a study area.

Lineament interpretation as either surficial or structural is non-trivial, especially if field observations are lacking. Identifying lineaments within known glacial features such as drumlins or glacial sediment can be used to distinguish between surficial and structural lineament suites within bedrock. Lineament orientation, spacing, and length are also critical to lineament interpretation. To achieve the best interpretation, I suggest a feedback loop between lineament mapping and comparison with field observations.

Interpretation of non-glacial lineaments depends largely on the regional geology and structural style of the study area. For this study metamorphic foliation and fault trajectories define the tectonic fabric. Areas of relatively pervasive parallel fabric correlate best with areas of well-developed foliation and faults. In other areas the relationship between the non-glacial lineament fabric and tectonic fabric could be quite different. Careful comparison of field observations and mapped lineaments is critical to making informed interpretations.

1.11. Summary

High-resolution LiDAR altimetry has potential for mapping lineaments related to both glacial geomorphological fabrics and regional tectonic fabrics related to bedrock structural geology. Our analysis shows that application of LiDAR shaded-relief images of glaciated terrane has several applications in structural geology including:

1. Constructing preliminary regional tectonic fabric maps from limited field observations, allowing for the formation and testing of structural models.
2. Directing field work to areas of interest to test structural models, making field work more efficient and decreasing field time.
3. Providing insight into inaccessible areas or areas of poor exposure.
4. Illustrating first-order crosscutting relationships and relative timings.
5. Placing detailed map areas into a broad regional structural context.

Application of LiDAR to this study area provides a 2D map-view of the tectonic fabric. The lack of 3D information is a function of the overall low topographic relief and the dominant sub-vertical orientation of geologic structures. This 2D view limits the usefulness of this analysis and illustrates the need for field mapping to better understand the 3D structural setting.

The techniques outlined herein can be applied to other areas of poorly exposed continentally glaciated terrane. Relatively large areas of bedrock with little to no sediment cover are necessary for LiDAR altimetry to be applicable, because sediment can obscure bedrock lineaments. An important aspect of this study is that the erosion processes of glaciation and frost wedging do not allow the formation of microtopography;

therefore construction of detailed structural maps (i.e., Pavlis and Bruhn, 2011) is difficult to impossible. Geologic setting, structural style, and erosion history directly control the topographic expression of the tectonic fabric and different areas may preserve tectonic fabric at different scales. Our analysis shows that LiDAR altimetry can be used to map regional tectonic fabric, and researchers that use LiDAR altimetry to analyze glaciated terrain should give careful consideration to geologic setting, structural style, and erosion history.

Table 1. Light Detection and Ranging Data Acquisition Details
 Data available at: <ftp://ftp.lmic.state.mn.us/pub/data/elevation/lidar/>

Project vendor	Woolpert Inc.
Flight altitude (above terrain)	1982.2 m
Post Spacing	1 m
Average ground speed	66 m/s
Pulse rate	115.6 kHz
Scan rate	41.8 kHz
Field of view	40 degrees
Side lap (Minimum)	25%
Swath width	variable
Distance between flight lines	variable
Horizontal accuracy	1m
Vertical accuracy RMSE	5cm
Coordinate system	UTM Zone 15
Horizontal Datum	NAD83
Vertical Datum	NAVD88 Geoid09
Horizontal unit	meter

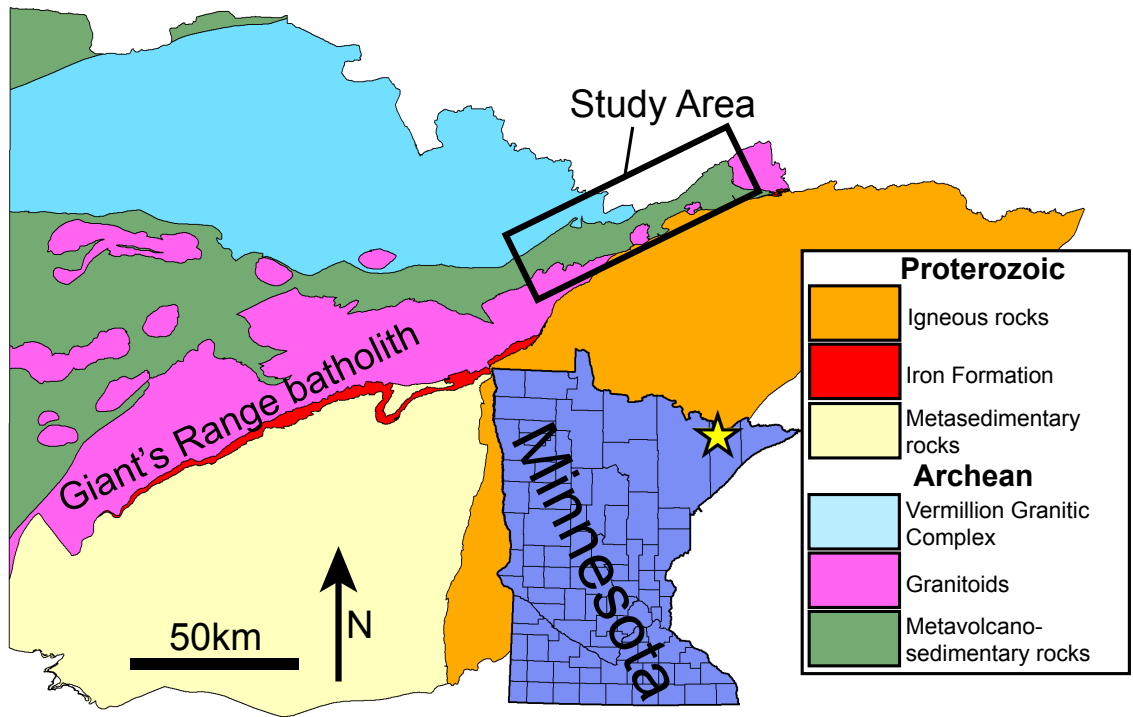


Figure 1.1. Simplified geologic map of NE Minnesota. Rectangle indicates location of Figure 1.2.

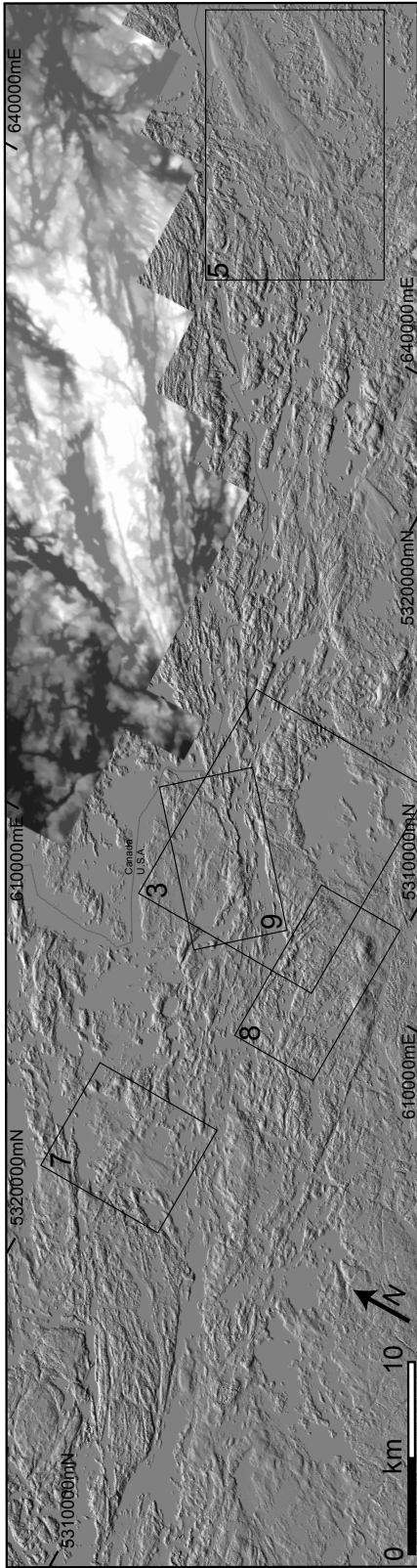


Figure 1.2. 1-meter shaded-relief image of the study area. Rectangles indicate locations of figures 1.3, 1.5, 1.7, 1.8, and 1.9. 15-meter digital elevation model of Ontario included for completeness.

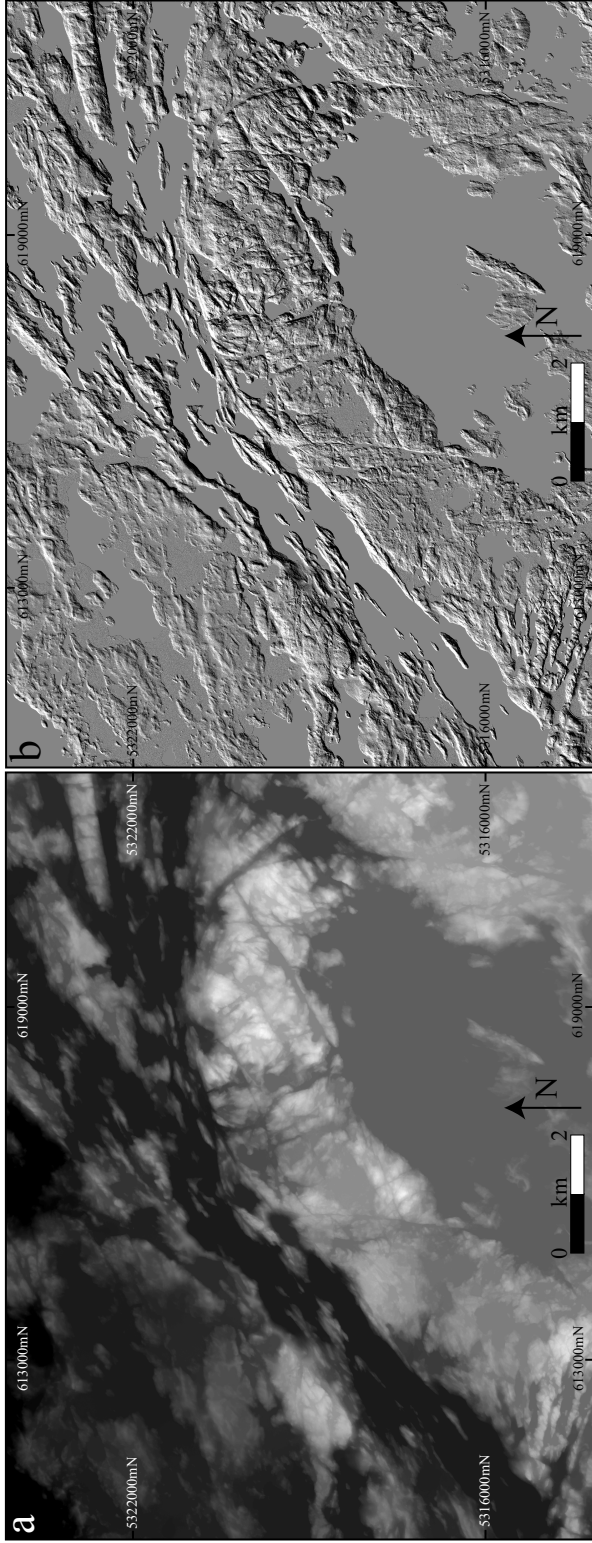


Figure 1.3. (a) Raw 1-meter DEM with grayscale symbolization showing a relatively fuzzy lineament fabric. Although large-scale lineaments are visible, relatively small-scale lineaments are not easily visible. (b) LiDAR-derived shaded relief image showing a distinct lineament fabric with both large-scale and small-scale lineaments easily visible. Sun elevation is 45° and sun azimuth is 315.

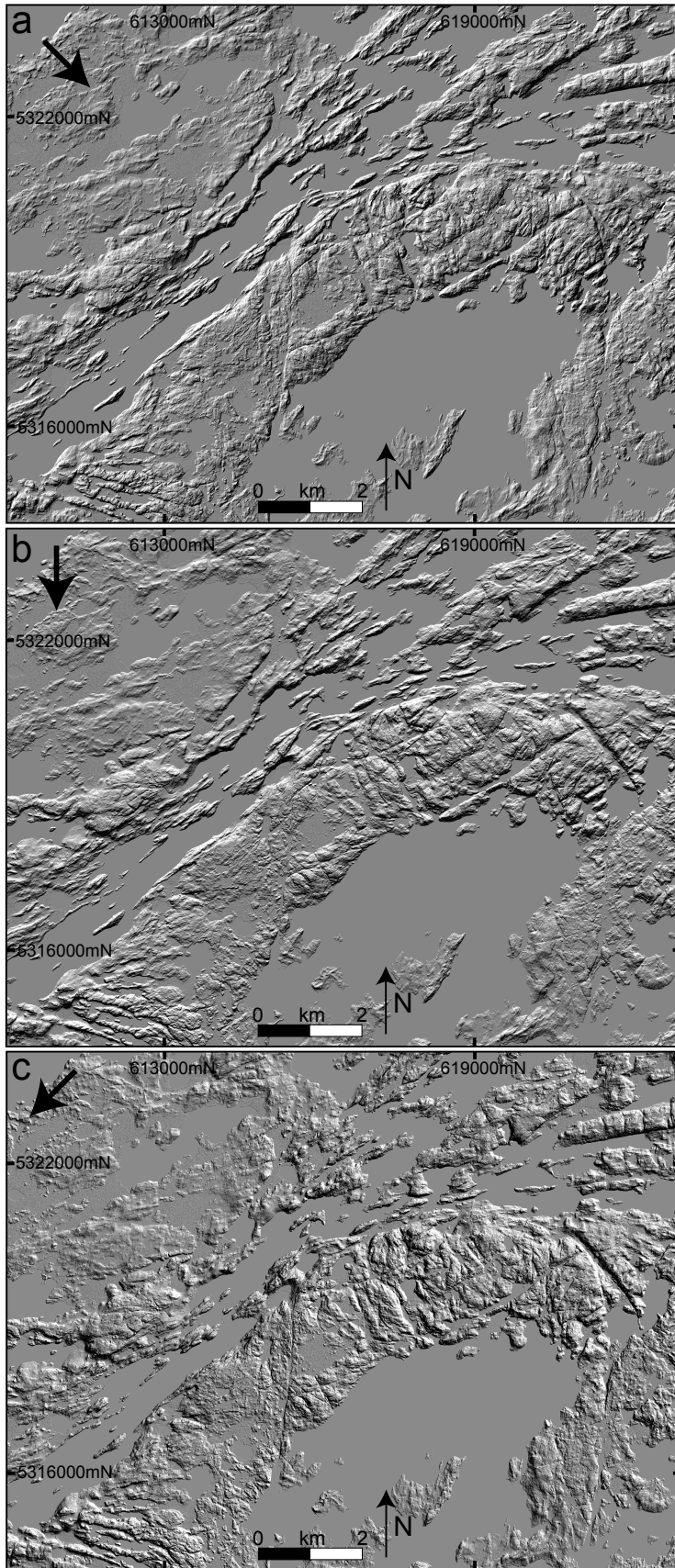


Figure 1.4. Shaded-relief images constructed with a sun elevation of 45 degrees and varying sun azimuth, (a) 315, (b) 000, and (c) 045. Large arrows indicate direction of sun azimuth. Lineaments trending perpendicular to sun azimuth are easily visible, whereas lineaments trending parallel to sun azimuth appear obscured or are invisible.

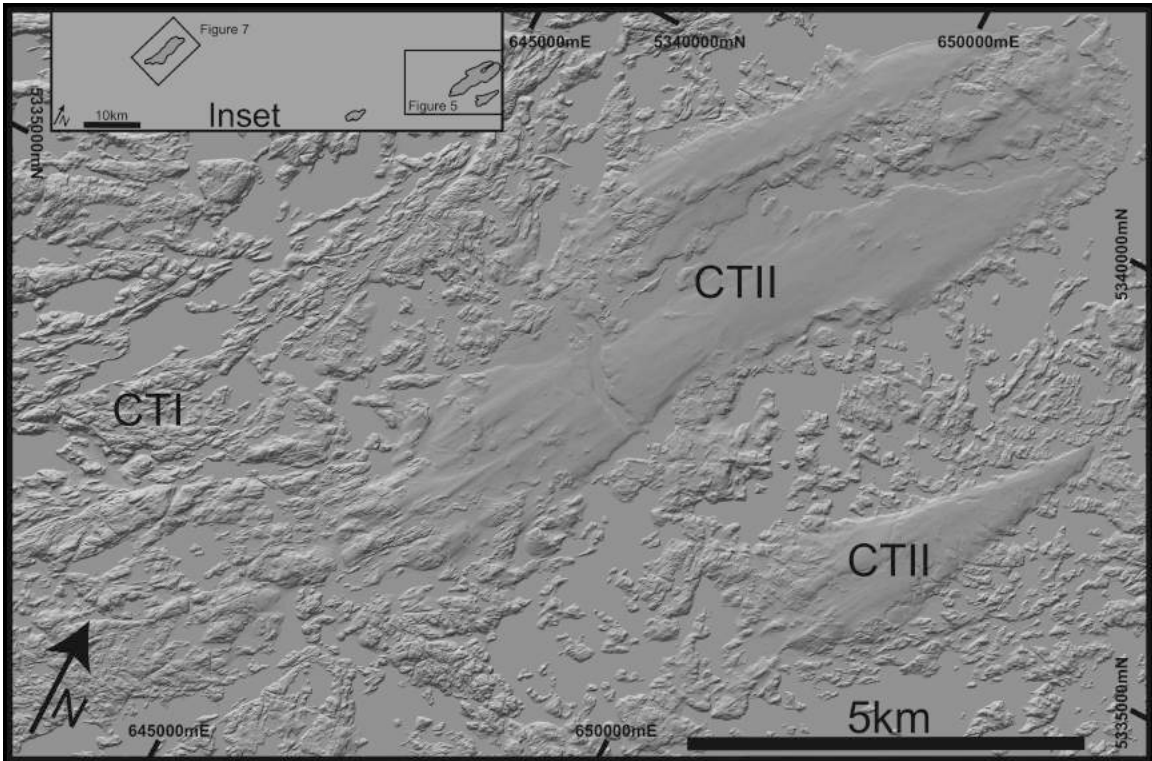


Figure 1.5. Map showing surface cover types (CTI and CTII) and associate LiDAR shaded-relief image. CTI corresponds to scoured bedrock. CTII corresponds to sediment cover. Inset: Cover-type map of the entire study area showing extent of sediment cover. Inset covers the same area as Figure 2. Rectangles mark the locations of Figure 1.5 and Figure 1.7.

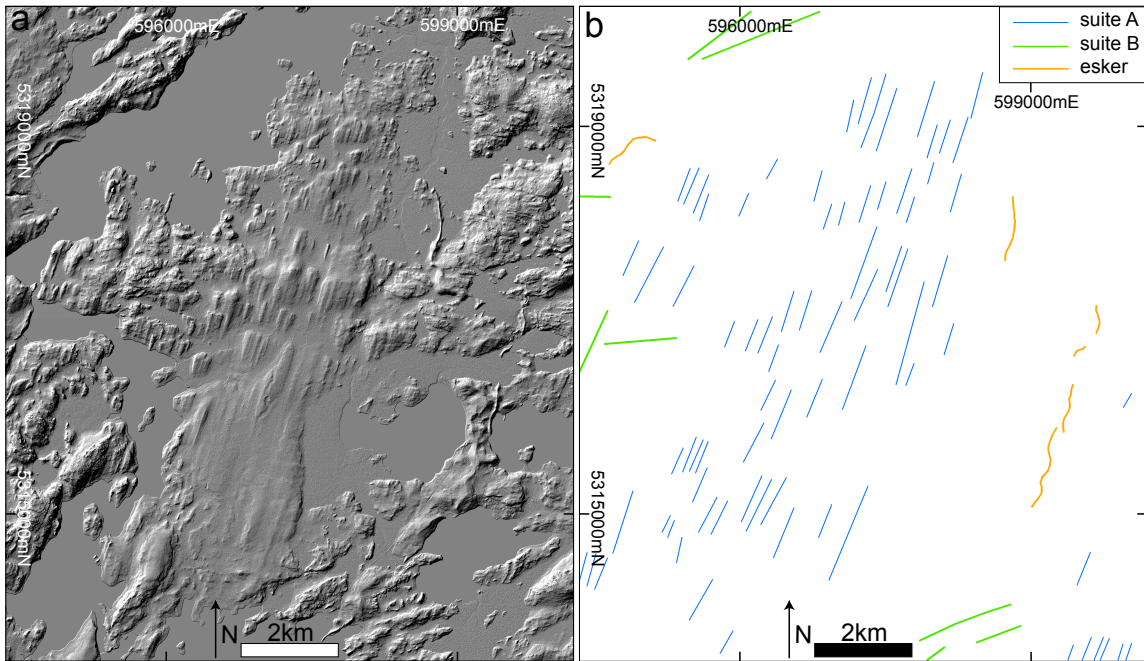


Figure 1.7. (a) 1-meter LiDAR derived shaded-relief image showing the topographic expression of various linear features within areas of scoured bedrock and shallow sediment cover and (b) the corresponding lineament map. Sun azimuth is 315 and sun elevation is 45 degrees.

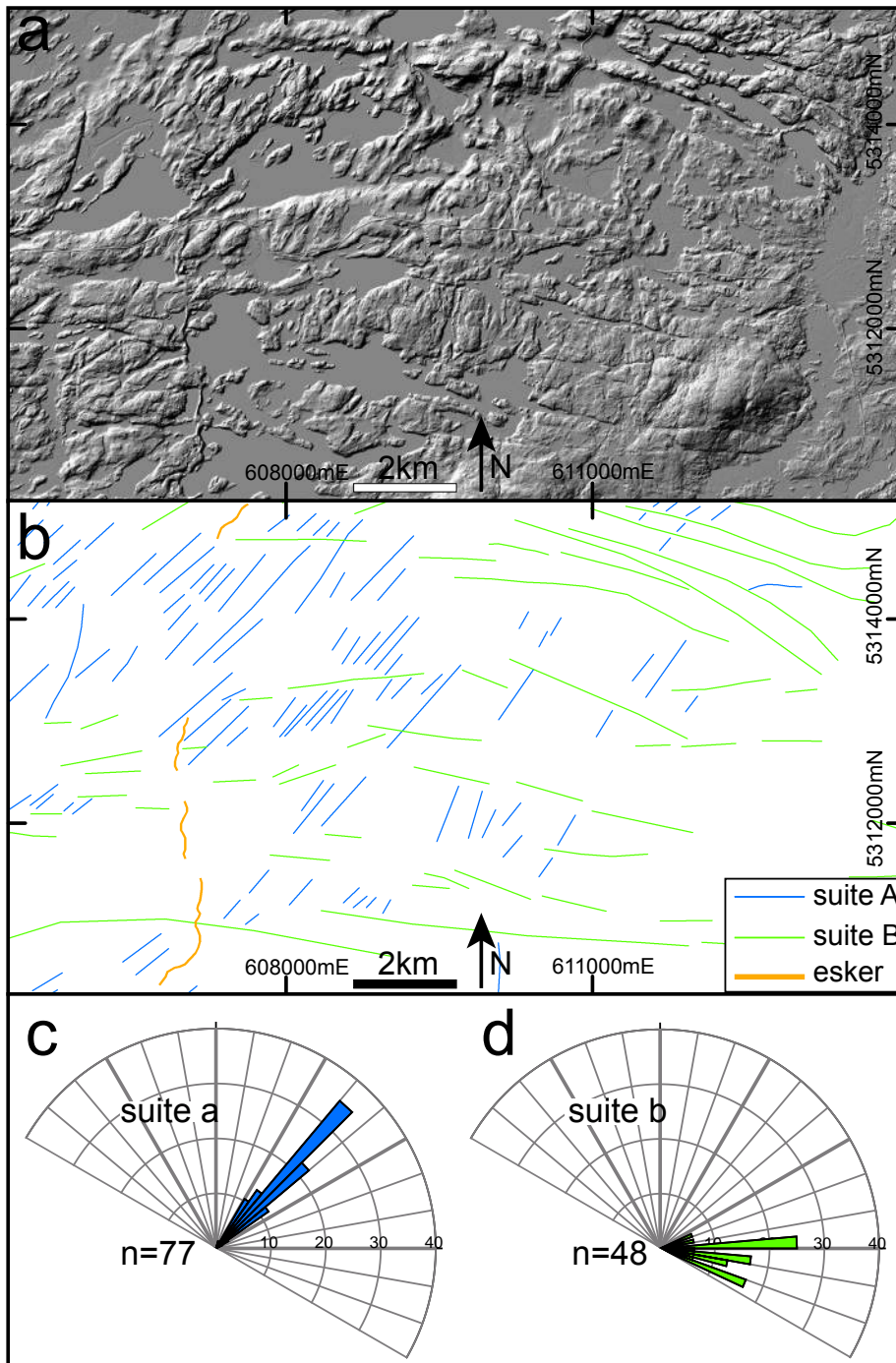


Figure 1.8. (a) LiDAR-derived shaded-relief image and (b) corresponding lineament map showing a localized lineament fabric with suite A and suite B lineaments at high angles to one another. Rose diagrams illustrate the local orientation distribution of (c) suite A and (d) suite B lineaments. Radial axes marked in percent of total data points. Rose-diagrams display average trend of each lineament.

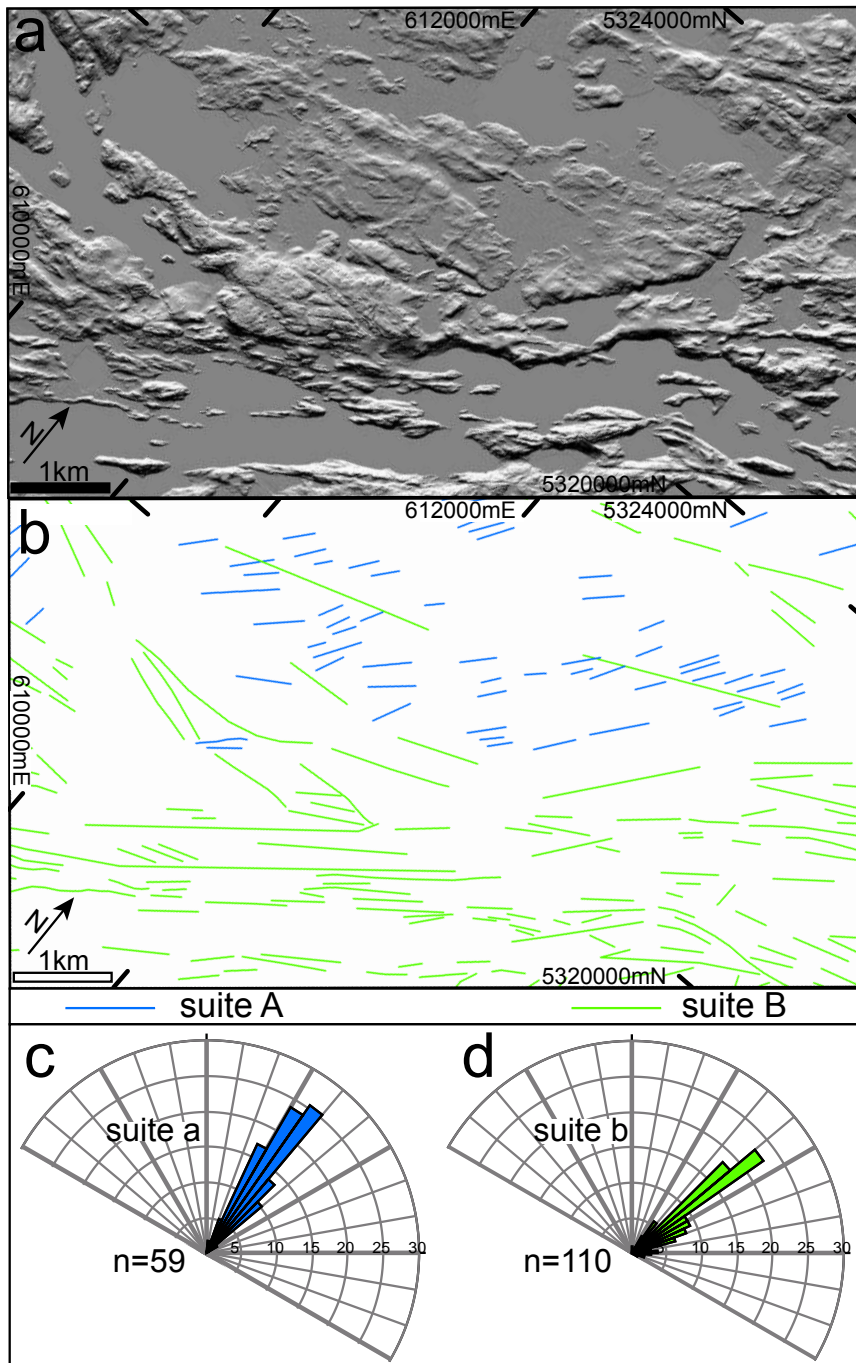


Figure 1.9. (a) LiDAR-derived shaded-relief image and (b) corresponding lineament map showing a localized lineament fabric with parallel suite A and suite B lineaments. Also included are rose diagrams the local orientation distribution of (c) suite A and (d) suite B lineaments. Radial axes marked in percent of total data points. Note north direction. Rose-diagrams display average trend of each lineament.

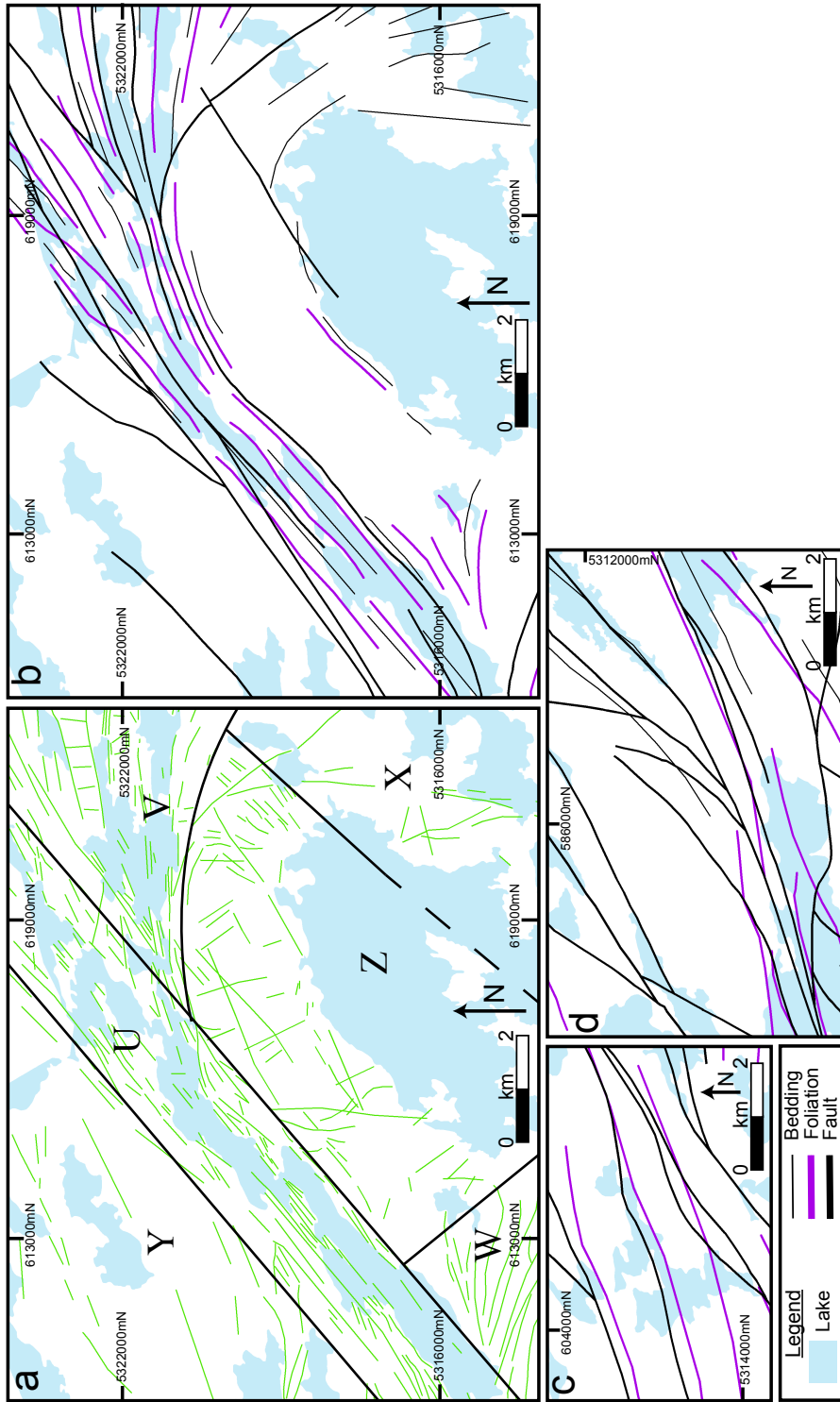


Figure 1.10. (a) Map showing localized suite B lineament fabric divided into six domains and (b) the corresponding structural trajectories. Domains are for illustrative purposes only; (c) and (d) other selected areas showing structural trajectories (see figure 1.6 for map locations). Structural data from Goodman (2008), Erickson (2008), Mulvey et al. (2009), and Jirsa et al. (2011).

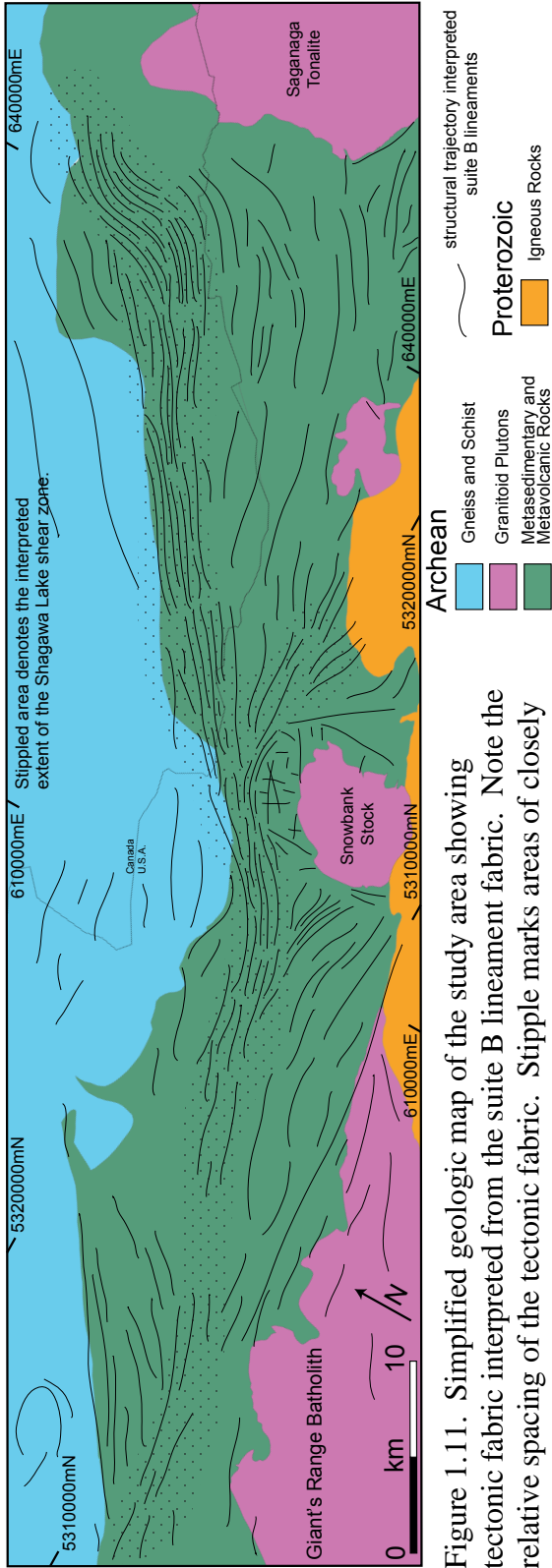


Figure 1.11. Simplified geologic map of the study area showing tectonic fabric interpreted from the suite B lineament fabric. Note the relative spacing of the tectonic fabric. Stipple marks areas of closely spaced, parallel lines define a curvilinear zone (shear zone?) across the map area. The tectonic fabric diverges around granitoid plutons within the metasedimentary and metavolcanic sequence.

2. Determination of vorticity in Neoproterozoic L-S tectonites

2.1. Introduction

There is no consensus about the processes responsible for the formation of Archean crust. The North American Superior Province is widely interpreted as a series of accreted terranes with subprovinces representing individual terranes (Talbot, 1973; Goodwin and Ridler, 1970; Langford and Morin, 1976; Dimroth et al., 1983a, b; Ludden et al., 1986; Sylvester et al., 1987; Percival and Williams, 1989). The Neoproterozoic (2.7-2.5 Ga) Wawa Subprovince forms a NE-trending belt of sub-greenschist to greenschist facies supracrustal rocks cut by multiple L-S tectonite packages marked by a well-developed metamorphic foliation (Fm) and elongation lineation (Le) (Fig. 2.1). The Wawa Subprovince has been interpreted as a transpressional plate-margin recording dextral strike-slip shear (Hudleston et al., 1988; Schultz-Ela and Hudleston, 1991; Jirsa et al., 1992). This interpretation is highlighted as evidence for Archean plate-tectonic processes based on plate-tectonic models that require extensive strike-slip shear zones, with length ≥ 1200 km (Sleep, 1992). Despite apparent broad acceptance of this interpretation, the nature of L-S tectonite formation within the Wawa Subprovince remains poorly constrained.

Within L-S tectonites, shear direction and magnitude is genetically linked to vorticity, marked by the vorticity-normal-section (VNS) and vorticity axis (pole to VNS) (Passchier, 1998; Xypolias, 2010 and references therein). However, geometric relationships between shear direction and macroscopic structures, such as Fm and Le, can vary depending on the mechanism governing L-S tectonite formation (Passchier, 1998).

Le can occur parallel, perpendicular, or oblique to shear direction during L-S tectonite formation. Therefore robust determination of L-S tectonite vorticity requires careful consideration before interpretation of shear direction. The determination of the vorticity axis and characterization of the geometric relations between the VNS, Fm, and Le can allow for the use of Fm and Le as an indicator for non-coaxial shear direction during L-S tectonite formation.

In this contribution, I determine the vorticity axis for seven samples of Neoproterozoic Vermilion District L-S tectonite (Fig. 2.1). I employ a combination of petrographic microstructural, X-Ray Computed Tomography (XRCT), and quartz crystallographic preferred orientation (CPO) data. These data indicate that the VNS lies within the Fm-normal Le-parallel plane and that the displacement direction is sub-parallel to Le for all seven samples. Regional Le orientation varies within the Wawa Subprovince ranging from steep to moderate plunge, with rare local zones of shallow plunge (Hudleston, 1976; Hudleston et al, 1988; Bauer and Bidwell, 1990; Jirsa, et al., 1992; Goodman, 2008; Erickson, 2008, 2010; Johnson, 2009; Karberg, 2009). Non-coaxial shear direction is sub-parallel to Le regardless of Le geographic orientation.

2.2. Background

2.2.1. Geologic Setting

The Vermilion District of NE Minnesota is a NE-trending belt of greenschist facies metavolcanic and metasedimentary rocks with granitoid bodies scattered throughout (Fig. 2.1). The Vermilion District includes from, north to south: the Vermilion Granitic Complex, greenschist facies metavolcanic and metasedimentary sequences, and quartz

monzonite of the Giant's Range Batholith (Sims, 1976). Granite, granite-rich and biotite-rich migmatites, biotite and amphibolite schists, metagabbro, metabasalt, and trondhjemite characterize the Vermilion Granitic Complex. Greenschist facies metavolcanic and metasedimentary sequences, which include protoliths of basalt, diabase, pyroxenite, basalt flows, felsic to intermediate volcanic tuff, felsic volcanic rocks, conglomerate, greywacke, shale, and banded iron formation are cut by ovoid granitoid bodies (Sims, 1976). Volcanic and plutonic rocks range in age from 2.75 to 2.69 Ga and from 2.74 to 2.65 Ga, respectively (Card, 1990 and references therein). To the SE, Paleoproterozoic plutonic rocks intrude the Vermilion District (Gruner, 1941; Jirsa and Miller, 2004).

The Vermilion District volcano-sedimentary sequence hosts several NE-striking subvertical L-S tectonite packages which extend up to ~70 km long and 7-10 km wide, although L-S tectonite boundaries are diffuse. Vermilion District L-S tectonites contain a well-developed anastomosing Fm with an orientation of $065, 90 \pm 15$ (Bauer and Bidwell, 1990; Erickson, 2008, 2010; Wolf, 2006; Goodman, 2008). Bedding marked by compositional layering commonly parallels Fm. Within the Fm plane is a variably developed Le. Le orientation varies within and between individual L-S tectonite packages; however Le typically plunges steeply to obliquely; narrow zones of shallowly plunging Le exist locally (Hudleston, 1976; Hudleston et al., 1988; Bauer and Bidwell, 1990; Jirsa, et al., 1992; Goodman, 2008; Erickson, 2008, 2010; Johnson, 2009; Karberg, 2009).

2.2.2 Vorticity within L-S tectonites

Determination of sample vorticity is fundamental to understanding of sense of shear and shear direction within naturally occurring L-S tectonites. Sample vorticity is marked by vorticity-normal-section (VNS) and vorticity axis (pole to VNS) within L-S tectonites (Passchier, 1998; Xypolias, 2010 and references therein). The vorticity axis is the line about which mineral grains rotate and marks the pole to the VNS. The VNS, the plane that records mineral grain rotation and the maximum asymmetric microstructural fabric, forms parallel to non-coaxial shear direction. Therefore identification of the VNS or vorticity axis should define shear direction within L-S tectonites.

Determination of vorticity of within L-S tectonites can be challenging.

Determination of vorticity within the metavolcanic and metasedimentary rocks of the Vermilion District can be particularly challenging due to low metamorphic grade and the fine-grained nature of the rocks, and geometric relations between vorticity, Fm, and Le vary depending on the shear geometry (Passchier, 1998). In the case of monoclinic shear, the vorticity axis can be parallel to Fm and normal to Le; parallel to Fm and Le; or normal to Fm (Fig. 2.2) (Passchier, 1998). In the case of triclinic shear the vorticity axis can be oblique to Le (Lin et al., 1998). Thus it is important to determine the vorticity axis orientation as a first step in kinematic analysis of L-S tectonites. If the vorticity axis is both parallel to Fm and Le, then planes normal to both Fm and Le should record asymmetric microstructural fabrics (Fig. 2.2 column 1). Conversely, if the vorticity axis is parallel to Fm and normal to Le, then planes normal to Fm and parallel to Le should record asymmetric microstructural fabrics (Fig. 2.2 column 2). If the vorticity axis is normal to Fm, then asymmetric microstructural fabrics should occur within the Fm plane

(Fig. 2.2 column 3)(Passchier, 1998). I determine vorticity axis orientation for seven samples using data derived from petrographic microstructural, XRCT, and quartz CPO analysis and document the spatial relationships between the vorticity axis, VNS, Fm, and Le. A complete listing of samples and applied techniques is given in Table 1.

2.2.3. Techniques for determination of vorticity

2.2.3.1. Petrographic microstructural techniques

A traditional method for determining vorticity and shear sense involves examination of microstructural fabrics in thin-section (e.g. Berthé et al., 1979; Passchier and Trouw, 2005). However, a thin-section represents a single 2D-view of a 3D-microstructural fabric; thus without prior knowledge of the VNS orientation, multiple thin sections from each sample are necessary to discover the vorticity axis and VNS relative to sample Fm and Le. I examined microstructures in sections cut normal to Fm and parallel to Le and normal to Fm and Le; these planes represent two possible VNS orientation expected in the case of monoclinic shear (Fig. 2.2) (Passchier, 1998). I examine microstructural fabrics in each thin-section using a petrographic scope; microstructures are classified according to the classification scheme defined by Passchier and Trouw (2005). I use the two thin-section views to approximate the shape of the 3D-microstructural fabric in each sample. One drawback to petrographic microstructural analysis is that a complete 3D characterization of the microstructural fabric requires many thin-sections, which are both costly and destructive to the sample. Also multiple thin-sections at different orientations cannot be easily cut from the same billet. Despite these challenges, information can be gleaned from this approach.

2.2.3.2. X-Ray Computed Tomography (XRCT) techniques

XRCT analysis is a nondestructive imaging process that allows for the characterization and quantification of the 3D-microstructural fabric of individual samples (Ketchum, 2005). Samples SB141, SB293, and SB104 were scanned at the University of Minnesota using the X5000 high resolution microCT system with a twin head 225 kV x-ray source and a Dexela area detector. A scan voltage of 110 kV and focal spot size of 6 μm were used to image samples with a minimum slice thickness of 13 μm . Volume reconstruction for all samples was completed using the system-supplied North Star Imaging software with a minimum voxel size of 13 μm . Reconstructed 3D-data were then down-sampled to a 30 micron voxel size to aid in processing time and analyzed in Avizo 8 Fire software for image processing. Image processing included contrast enhancement and filtering to aid segmentation of the desired phases and to produce image slices for subsequent object-based and fabric-based kinematic analysis.

Kinematic analysis performed using XRCT data is similar to petrographic microstructural analysis. Using the 3D-reconstruction, image slices can be created for any view within the sample volume, allowing for visualization of the 3D-microstructural fabric. Ortho-slices were created in Fm-normal Le-parallel and Fm-normal Le-normal views. Ortho-slices directly link petrographic microstructural and XRCT observations. Individual high-contrast microstructures were segmented and used to create 3D-surfaces for subsequent object-based analysis.

Object-based analysis was completed using BLOB3D software (Ketcham, 2005). After segmentation of the desired phase, 3D-surfaces were captured, and the EXTRACT

module calculated grain location, volume, shape, long-axis orientation, and short-axis orientation. Of particular interest to this study are the orientation of the 3D-fabric long- and short-axes. Orientations are output as directional cosines, which are converted to trend and plunge for projection onto a lower hemisphere equal area stereonet.

Grain-shape fabric analysis was carried out using QUANT3D software (Ketcham and Ryan, 2004). Three methodologies are available: (1) star-volume distribution (SVD) (Cruz-Orive et al., 1992; Karlsson and Cruz-Orive, 1993); (2) star-length distribution (SLD) (Odgaard et al., 1997; Smit et al., 1998); and (3) mean intercept length (MIL) (Cowin, 1986; Harrigan and Mann, 1984; Launeau and Robin, 1996; Whitehouse, 1974). Among these analyses, the first, SVD, shows the highest shape contrast and has the best visualization potential.

SVD analysis includes two products, a fabric tensor and 3D-rose diagrams (Ketcham, 2005). The fabric tensor is defined by a set of eigenvectors and eigenvalues that mark three orthogonal principal axes; the fabric tensor is similar to a strain tensor with eigenvectors marking principal strain axes. 3D-rose diagrams are created by projecting each star volume analysis direction from the origin, according to its corresponding star component measurement; values are then normalized by dividing by the maximum measurement value. Eigenvectors can also be plotted on the 3D-rose diagrams (Ketcham, 2005).

2.2.3.3. *Quartz crystallographic preferred orientation (CPO) analysis*

Quartz CPO data were acquired using electron backscatter diffraction (EBSD) via the scanning electron microscope (SEM) at the University of Minnesota Duluth Research

Instrumentation Laboratory. Quartz c- and a-axis orientations were obtained with a HKL EBSD detector and Channel 5 software suite (Schmidt and Olesen, 1989). Sample KS6U and KS7J were analyzed in the Fm-normal Le-normal and Fm-normal Le-parallel views, respectively. Samples were prepared by polishing commercial microprobe-polished 30 μ m thick thin-sections for approximately three additional hours in a colloidal silica suspension. The samples were not carbon coated. Samples were analyzed with a tilt of 70° and a chamber pressure of 1 Pa. EBSD patterns were collected in automatic mapping mode with a step size greater than the mean sample grain size. Operating parameters include: an accelerating voltage of 15 kV, working distance of 25 mm, and a 3.5 nA beam current. Channel 5 acquisition and indexing settings were 2x2 binning, Hough resolution = 80, 8 bands, and 70 reflectors. Accepted data points were limited to those with a mean angular deviation $\leq 1^\circ$.

2.3. Sample description

I examined seven L-S tectonite samples from the Vermilion District of northeastern Minnesota. Five samples originate from a L-S tectonite package commonly referred to as the Shagawa Lake shear zone (SLSZ), and two samples originate from a L-S tectonite package commonly referred to as the Kawishiwi shear zone (KSZ) (Fig. 2.1). All samples contain a well-developed Fm and Le. Fm and Le orientation for each sample is indicated in Table 1.

2.3.1. Sample SB191

Sample SB191, a fine-grained mica schist, consists of an undifferentiated matrix of white-mica, chlorite, calcite, plagioclase, and quartz, containing pyrite and plagioclase

clasts. A grain-shape preferred orientation of white-mica, chlorite, and calcite defines Fm; within the Fm-normal Le-parallel section S-C fabrics occur (Fig. 2.3a-1). Elongate plagioclase feldspar clasts (up to 1 mm long) are surrounded by calcite mantles of σ -geometry (Fig. 2.3a-1). Pyrite clasts (up to 0.5 mm across) display asymmetric quartz-fiber strain fringes. Overall the Fm-normal Le-parallel section contains an asymmetric microstructural fabric with fabric asymmetry consistent with top-to-the-right non-coaxial shear within this plane.

The Fm-normal Le-normal section exhibits a symmetric microstructural fabric (Fig. 2.3a-2). Within this view white-mica defines a parallel planar foliation. Plagioclase feldspar clasts lack obvious calcite mantles, and pyrite clasts lack obvious strain fringes. Microstructural fabrics in the Fm-normal Le-normal view are consistent with a flattening normal to Fm and coaxial shear.

2.3.2. *Sample SB245*

Sample SB245, a fine-grained mafic metavolcanic rock, consists of an undifferentiated matrix of chlorite, plagioclase feldspar, amphibole, and calcite, containing pyrite clasts (Fig. 2.3b). A grain-shape preferred orientation of chlorite, and calcite defines Fm. There are no obvious asymmetric microstructural fabrics within the dark matrix-material in either the Fm-normal Le-parallel or Fm-normal Le-normal sections. Sample SB245 contains pyrite clasts (up to 2mm across) with strain fringes in the form of quartz and calcite fibers. Within the Fm-normal Le-parallel section, strain fringes occur adjacent to multiple pyrite grains; asymmetric fringe shapes are consistent with top-to-the-left non-coaxial shear within this plane (Fig. 2.3b-1). Within the Fm-

normal Le-normal section, strain fringes are relatively small and show no obvious pattern (Fig. 2.3b-2).

2.3.3. *Sample SB141*

Sample SB141, an iron-carbonate schist, consists of a fine undifferentiated matrix of white-mica, carbonate, plagioclase feldspar, and quartz, with white-mica defining Fm. This rock includes mantled iron oxide replaced porphyroclasts (Fig. 2.4a). Within the Fm-normal Le-parallel section porphyroclasts replaced by iron oxide, range from 0.5 – 2 mm long and show σ -geometry with top-to-the-left shear sense (Fig. 2.4a-1).

Asymmetric white-mica halos, adjacent the porphyroclasts, also record top-to-the-left shear. Within the Fm-normal Le-normal section, porphyroclasts are ovoid in shape with diameter ranging from 0.5 - 1 mm; porphyroclasts long- and short-axes are parallel and normal to Fm, respectively (Fig. 2.4a-2). White-mica halos form a symmetric pattern around porphyroclasts. XRCT slices in the Fm-normal Le-parallel view show mantled porphyroclasts with rounded cores and mantles that display σ -geometry consistent with top-to-the-left shear (Figs. 2.4a-3 and 2.4a-4). Mantles in the Fm-normal Le-normal view are symmetric about porphyroclast cores and elongate parallel to C-foliation. White-mica halos do not show up within the XRCT data because white-mica does not mark a significant difference in local density.

Porphyroclast 3D-surfaces, generated using BLOB3D, reveal that the porphyroclasts exhibit a consistent σ -geometry in 3D, with long-axis orientations within or near the C- or S-foliation and parallel to Le. Short-axes are roughly normal to C-foliation (Fig. 2.5). SVD analysis, generated using QUANT3D, plotted as a 3D-rose

diagram illustrates the shape anisotropy of the porphyroclasts. The porphyroclasts are elongate in the Fm-normal Le-parallel view and relatively ovoid in the Fm-normal, Le-normal view (Fig. 2.6). Eigenvectors produced by the SVD analysis correlate to finite strain axes. The direction of maximum elongation parallels Le and S-foliation, and the direction of minimum elongation is normal to S-foliation (Fig. 2.6a). Grain shape calculations from BLOB3D and QUANT3D, petrographic microstructural, and XRCT observations are all consistent with top-to-the left non-coaxial shear in the Fm-normal Le-parallel view and coaxial shear normal to Fm in the Fm-normal Le-normal view.

2.3.4. Sample SB293

Sample SB293, a white-mica schist, consists of an undifferentiated matrix of white-mica, chlorite, calcite, quartz, and plagioclase feldspar. This rock includes pyrite clasts (<0.5 mm) and quartz and plagioclase feldspar clasts (< 3 mm). Within the Fm-normal Le-parallel section, a grain-shape preferred orientation of chlorite and calcite define an asymmetric S-C fabric (Fig. 2.4b-1). Quartz-fiber strain fringes occur adjacent to several pyrite grains; fringe shapes are consistent with top-to-the-right non-coaxial shear. Quartz also occurs as rounded clasts; these clasts contain numerous subgrains and display undulose extinction or occur as elongate or sigmoidal shapes that are incorporated into the S-C fabric (Fig. 2.4b-3 and 4b-4). Plagioclase clasts are ovoid with fine-grain calcite and quartz mantles that are consistent with top-to-the-right non-coaxial shear. Within the Fm-normal Le-normal section, no obvious asymmetric microstructural fabrics occur; regions of elongate quartz and mantled plagioclase feldspar grains display no obvious consistent asymmetry (Fig. 2.4b-2).

2.3.5. *Sample SB104*

Sample SB104, an iron-carbonate schist, consists of a fine-grained matrix of undifferentiated white-mica, chlorite, carbonate, plagioclase feldspar, and quartz. This rock includes mantled porphyroclasts that have been replaced by calcite (Fig. 2.4c). Within the Fm-normal Le-parallel section a grain-shape preferred orientation of white-mica defines a S-C fabric consistent with top-to-the-right non-coaxial shear (Fig. 2.4c-1). Porphyroclasts range from 0.5 – 1 mm across with mantles of fine white-mica and quartz. Mantles are of σ -geometry consistent with top-to-the-right shear sense (Figs. 2.4c-1 and 2.4c-4). Although these mantles are obvious in thin-section; the mantles are not easily distinguishable in the XRCT image due to the similarity in density of the mantle and matrix material (Fig. 2.4c). Within the Fm-normal Le-normal section, white-mica defines Fm with no obvious S-C fabric; mantled porphyroclasts exhibit no obvious consistent asymmetric patterns (Fig. 2.4c-2).

2.3.6. *Sample KS6U*

Sample KS6U is characterized by deformed quartz vein material with a strike-parallel Le (Fig. 2.7a). The quartz vein parallels local Fm, individual grains (250 μ m across) are polygonal with sharp straight euhedral grain boundaries; grain show moderate undulose extinction. These characteristics record subgrain rotation recrystallization, corresponding to regime II of Hirth and Tullis (1992), and deformation temperatures ranging from 390 to 490 °C (Stipp et al., 2002).

Quartz c-axes define a single girdle containing a maximum population within Fm (Fig. 2.8a). Quartz a-axes data display a maxima girdle along the primitive circle with

two maxima within the C-foliation plane (Fig. 2.8a). The pole to the a-axis maxima girdle is normal to Le and lies within Fm. This CPO fabric is consistent with slip along the prism $\langle a \rangle$ slip system within plane strain non-coaxial shear (i.e., simple shear) (Lister and Hobbs, 1980; Schmid and Casey, 1986). EBSD data collected in this study are broadly consistent with the c-axis patterns derived using a universal stage (Goodman, 2008)

2.3.7. *Sample KS7J*

Sample KS7J is from a quartz vein that parallels Fm and contains a dip-parallel Le (Fig. 2.7b). Quartz grain size ranges from 50-1000 μm with a mean grain size of 500 μm . Quartz grains display undulose extinction, diffuse ragged boundaries, well-defined subgrains, and a grain-shape preferred orientation within the Fm-normal Le-parallel section (Fig. 2.7b). Collectively these characteristics record bulging recrystallization, corresponding to regime I of Hirth and Tullis (1992), and deformation temperatures of 270 to 390 $^{\circ}\text{C}$ (Stipp et al., 2002).

Quartz c-axes data display a rough cross-girdle containing populations associated with the basal $\langle a \rangle$, rhomb $\langle a \rangle$, \pm prism $\langle a \rangle$ slip systems (Fig. 2.8b). Quartz a-axes data define a maxima girdle oblique to the primitive circle within the Fm-normal Le-parallel view (Fig. 2.8b). The a-axis maxima girdle pole is normal to Le and at a low angle to Fm. This CPO fabric is indicative of non-coaxial general shear (Lister and Hobbs, 1980; Schmid and Casey, 1986). EBSD data collected in this study are broadly consistent with the c-axis patterns derived using a universal stage (Goodman, 2008)

2.4. Determination of vorticity

Vorticity determination relies on identifying the orientation of the vorticity axis or VNS. Understanding vorticity is key to unlocking Le as an indicator for non-coaxial shear direction in Vermilion District L-S tectonites. Below I compare observations from this study to the monoclinic shear models of Passchier (1998) in order to better understand the relationship between vorticity and Le in the Vermilion District. I test three models: vorticity axis parallel to Fm and Le (Model 1; Fig. 2.2 column 1; X1-shear zone of Passchier (1998)); vorticity axis parallel to Fm and normal to Le (Model 2; Fig. 2.2 column 2; X2-shear zone of Passchier (1998)); and vorticity axis normal to Fm and Le (Model 3; Fig. 2.2 column 3; Z1-shear zone of Passchier (1998)).

2.4.1. Model 1: Vorticity axis parallel to Le and parallel to Fm; VNS normal to Fm and normal to Le

Model 1 predicts: (1) the formation of Le normal to non-coaxial shear direction, (2) asymmetric microstructural fabrics in a Fm-normal Le-normal section, and (3) a lack of asymmetric microstructural fabrics in a Fm-normal Le-parallel section (Fig. 2.2a-1). These predictions are in stark contrast to the data for the samples in this study. Thin-sections and XRCT slices consistently show well-developed asymmetric microstructural fabrics in Fm-normal Le-parallel sections. Asymmetric microstructures include S-C fabrics, σ -geometry mantled porphyroclasts, mica halos, and quartz-fiber strain fringes; all indicate a coherent sense of shear within Fm-normal Le-parallel sections within individual samples (Figs. 2.3 and 2.4). In contrast, Fm-normal Le-normal sections lack obvious visible asymmetric microstructural fabrics. Furthermore, in sample SB141, mica

halos occur in four roughly-symmetric mattes around the porphyroclasts, describing a symmetric, rather than asymmetric, fabric (Figs. 2.3 and 2.4).

Both object-based and fabric-based XRCT analysis reveals 3D-mantled porphyroclast geometries inconsistent with model 1 predictions (Figs. 2.5 and 2.6). Model 1 predicts the formation of mantles with long-axes parallel to Le and intermediate-axes normal to Le, forming a cross-like shape when viewed into Fm (Fig. 2.2b-1). 3D-surfaces of mantled porphyroclasts and the orientation long- and short-axes show mantled-porphyroclast long-axes that parallel Le, yet these forms lack the distinctive 3D cross-like shape predicted by model 1 (Fig. 2.5). 3D-rose diagrams also illustrate that the long-axes of the mantled-porphyroclasts parallel Le; however principal strain axes calculated by SVD analysis indicate that minimum elongation and intermediate elongation have similar magnitudes, which is inconsistent with model 1 (Fig. 2.6).

Quartz c-axis CPO data (Fig. 2.8) are inconsistent with c-axis orientations predicted by model 1 (Fig. 2.2c-1). Quartz a-axis CPO data plot along the primitive circle within the Fm-normal Le-parallel view (Fig. 2.8a). The pole to the a-axis maxima girdle represents the vorticity axis (Lister and Hobbs, 1980; Schmid and Casey, 1986). Thus the vorticity axis is normal to the Fm-normal Le-parallel view in sample KS6U and at a high angle to the Fm-normal Le-parallel view in sample KS7J, both of which are inconsistent with model 1.

2.4.2. Model 2: Vorticity axis normal to Le and parallel to Fm; VNS normal to Fm and parallel to Le

Model 2 predicts: (1) the formation of Le parallel to non-coaxial shear direction, (2) vorticity axis parallel to Fm and normal to Le, (3) asymmetric microstructural fabrics in the Fm-normal Le-parallel view, and (4) a lack of asymmetric microstructural fabrics in the Fm-normal Le-normal view (Fig. 2.2a-2). These predictions are broadly consistent with the data for samples in this study. Thin-sections and XRCT slices consistently show well-developed asymmetric microstructural fabrics within Fm-normal Le-parallel sections (Figs. 2.3 and 2.4). Asymmetric microstructures (S-C fabrics, σ -geometry mantled porphyroclasts, mica halos, and quartz-fiber strain fringes) all indicate a coherent sense of shear within Fm-normal Le-parallel sections within individual samples (Figs. 2.3 and 2.4). Fm-normal Le-normal sections display symmetric microstructural fabrics indicating that mineral grains record flattening normal to Fm. (Figs. 2.3 and 2.4)

Both object-based and fabric-based XRCT analyses display 3D-mantled-porphyroclast shapes consistent with model 2 predictions (Figs. 2.5 and 2.6). Model 2 predicts the formation of mantles with long-axes parallel to Le and relatively equant intermediate- and short-axes (Fig. 2.2b-2). 3D-surfaces of mantled porphyroclasts and the orientations of long- and short- axes show mantled porphyroclast long-axes parallel to Le and a 3D-porphyroclast geometry similar to that predicted by model 2 (Fig. 2.2b-2). 3D-rose diagrams illustrate that the long-axes of the mantled-porphyroclasts are broadly parallel to Le. Principal strain axes calculated via SVD analysis indicate that the minimum elongation and intermediate elongation axes have similar magnitudes, which is consistent with model 2 (Fig. 2.6b).

Quartz c-axis CPO data are broadly consistent with c-axis orientations predicted by model 2 (Fig. 2.2c-2). Within the Fm-normal Le-parallel view, quartz a-axis CPO data plot along the primitive circle (Fig. 2.8a). I interpret the pole to the a-axis maxima girdle as the vorticity axis (Lister and Hobbs, 1980; Schmid and Casey, 1986), which is normal to the Fm-normal Le-parallel view in sample KS6U and at a high angle to the Fm-normal Le-parallel view in sample KS7J, both of which are consistent with model 2 (Fig. 2.2c-2). Complications regarding quartz CPO data and general shear are discussed in section 5.

2.4.3. Model 3: Vorticity axis normal to Le and Fm; VNS parallel to Fm

Model 3 predicts: (1) the formation of Le parallel to non-coaxial shear direction, (2) vorticity axis normal to Fm and Le, (3) asymmetric microstructural fabrics within the Fm plane, and (4) a lack of asymmetric microstructural fabrics in either Fm-normal Le-parallel or Fm-normal Le-normal sections (Fig. 2.2a-3). These predictions are in stark contrast to the data for the samples in this study. As previously stated, asymmetric microstructures (including S-C fabrics, σ -geometry mantled porphyroclasts, mica halos, and quartz-fiber strain fringes) occur within Fm-normal Le-parallel sections (Figs. 2.3 and 2.4). Furthermore, no consistent asymmetric microstructural fabrics occur within the Fm plane.

Both object-based XRCT analyses display 3D-mantled-porphyroclast geometries inconsistent with model 3 predictions (Fig. 2.5). Model 3 predicts the formation of mantles with asymmetry in the Fm plane and long-axes inclined to Le within Fm (Fig. 2.2b-3). 3D-surfaces of mantled-porphyroclasts and the orientations of long- and short-

axes of mantled-porphyroclast are roughly symmetric within the Fm with porphyroclast long-axes parallel to Le (Fig. 2.5).

Quartz c-axis CPO data (Fig. 2.8) are inconsistent with c-axis orientations predicted by model 3 (Fig. 2.2c-3). As previously stated, the pole to the a-axis maxima girdle represents the vorticity axis (Lister and Hobbs, 1980; Schmid and Casey, 1986). The vorticity axis is normal to the Fm-normal Le-parallel section in sample KS6U (Fig. 2.8a) and at a high angle to the Fm-normal Le-parallel view in sample KS7J (Fig. 2.8b).

2.5. Le as a proxy for non-coaxial shear direction

2.5.1. Lc striations vs. Ls lineations

Within the samples discussed herein, Le occurs in two forms, stretching lineations on S-surfaces (Ls) and ridge-in-groove striations on C-foliation surfaces (Lc) (Lin and Williams, 1992; Lin et al., 2007). Deformed markers such as elongated grains, mineral aggregates, and or pebbles define Ls (Lin and Williams, 1992; Lin et al., 2007). Lc striations, which occur on the C-plane, are commonly of the “ridge-in-groove” type and have the appearance of ductile slickensides (Lin and Williams, 1992; Lin et al., 2007). Though Lc and Ls both develop during non-coaxial shear, the relationship between Lc and Ls formation and displacement direction can be difficult to uniquely determine. Within simple shear, Ls forms parallel to shear direction, and within general shear, Ls progressively rotates away from shear direction (Lin et al., 2007). In contrast, Lc forms parallel to the shear direction on individual C-planes in both the monoclinic and general shear cases. In the situation in which I recognize both Lc and Ls in the same sample, Lc

parallels L_s within F_m . I interpret non-coaxial shear direction broadly parallel to either L_c or L_s respectively for a given sample (Lin and Williams, 1992; Lin et al., 2007).

2.5.2. General shear in sample KS7J

Sample KS7J displays quartz CPO fabrics interpreted as the result of general shear (Fig. 2.8b). Under general shear conditions, L_e need not form parallel or normal to non-coaxial displacement direction as in monoclinic shear geometries (Lin et al., 1998). However, quartz a-axis patterns display a maxima girdle with a pole normal to L_e and at a low angle to F_m , indicating that sample KS7J has a vorticity axis that lies at a low angle to F_m , and oriented near normal to L_e . The results of sample KS7J do not strictly adhere to one of the three monoclinic shear models. However the shear model that best fits the data can be determined by making some key observations. Sample KS7J records a vorticity axis normal to L_e . Model 1 predicts that the vorticity axis forms parallel to L_e and is not consistent with the data. Models 2 and 3 both predict a vorticity axis normal to L_e ; however models 2 and 3 each predict a vorticity axis either parallel or normal to F_m , respectively. In the case of sample KS7J, the vorticity axis, as given by the pole to the a-axis maxima girdle, is normal to L_e and within 20° from F_m . This geometry is inconsistent with model 3 and broadly consistent with model 2 (Fig. 2.8b). These data record general shear deformation that accommodated broad L_e -parallel non-coaxial shear and F_m -normal shortening. The slip vector of the non-coaxial component of deformation is sub-parallel to L_e (e.g. Sullivan et al., 2011). Furthermore, KS7J records asymmetric microstructural fabrics in the form of a grain-shape preferred orientation within the F_m -

normal Le-parallel view (Fig. 2.7b). Thus I interpret the oblique shear component as relatively minor compared to Le-parallel non-coaxial shear component.

Data collected in this study are most consistent with a vorticity axis within Fm and normal to Le and a VNS normal to Fm and parallel to Le (model 2). Thus the Fm-normal Le-parallel view is near parallel to the VNS. Predictions made by models 1 and 3 are inconsistent with the data for the Vermilion District samples. Accordingly, Fm and Le within Vermilion District L-S tectonites can serve as a marker for vorticity with the vorticity axis parallel to Fm and normal to Le or in other words, VNS normal to Fm and parallel to Le. Therefore Fm and Le can be used to determine the optimum plane to interpret shear direction. This view (i.e., the VNS) is the Fm-normal Le-parallel view. In the case of Vermilion District L-S tectonites, Fm and Le evolved as a result of non-coaxial shear sub-parallel to Le.

2.6. Summary and conclusions

Data in this study provide a clear and consistent view of vorticity within seven Vermilion District L-S tectonites. These L-S tectonites each display asymmetric microstructural fabrics within Fm-normal Le-parallel views and no consistent asymmetric fabric within Fm-normal Le-normal views (Figs. 2.3 and 2.4). The long-axes of mantled porphyroclasts are sub-parallel to Le and sub-parallel to the maximum elongation direction calculated via the SVD analysis. Quartz CPO data of sample KS6U display an a-axis maxima griddle normal to S-foliation and parallel to Le. Quartz CPO data of sample KS7J display an a-axis maxima griddle slightly oblique to S, with the pole to the girdle nearly normal to Le. These data are most consistent with monoclinic shear models

with vorticity axis parallel to Fm and normal to Le and non-coaxial shear direction sub-parallel to Le. The data reviewed herein are largely inconsistent with monoclinic shear models with vorticity axis parallel to Le or normal to Fm. Data presented in this study show that non-coaxial shear direction is sub-parallel to Le and that Fm and Le may be used as an indicator for the vorticity axis, VNS, and non-coaxial shear direction within Vermilion district L-S tectonites in particular, and Neoproterozoic L-S tectonites in general. Le orientation within Neoproterozoic L-S tectonites in the Vermilion District of NE Minnesota ranges from steeply plunging to sub-horizontal (Hudleston, 1976; Hudleston et al, 1988; Bauer and Bidwell, 1990; Jirsa, et al., 1992; Goodman, 2008; Erickson, 2008, 2010; Johnson, 2009; Karberg, 2009). However, the relationship between, the vorticity axis, VNS, non-coaxial shear direction, Fm, and Le are consistent irrespective of Le geographic orientation. Accordingly, future studies should give significant consideration to the issue of vorticity and non-coaxial shear direction relative to Fm and Le before kinematic interpretation of L-S tectonites.

Table 2.1

Sample locations and orientations, coordinates in UTM zone 15N, NAD 1983 (also given in decimal degrees).

Sample	mE	mN	Lat (DD)	Long (DD)	Fm	Le	Shear Zone	Method		
								Thin Section	XRCT	CPO
SB141	611891	5316406	47.991161°N	91.500269°W	239, 84NW	031, 75	SLSZ	x	x	
SB293	623680	5322617	48.044847°N	91.340528°W	116, 148, 76SW	65	SLSZ	x	x	
SB104	615607	5320548	48.027752°N	91.449363°W	234, 350, 82NW	81	SLSZ	x	x	
SB191	619760	5321489	48.03545°N	91.393418°W	090, 113, 88S	84	SLSZ	x		
SB245	620283	5321075	48.031629°N	91.386521°W	095, 278, 84SW	17	SLSZ	x		
KS7J	600209	5307126	47.909783°N	91.688367°W	273, 001, 80N	80	KSZ	x		x
KS6U	600199	5306997	47.908467°N	91.659117°W	285, 105, 80N	0	KSZ	x		x

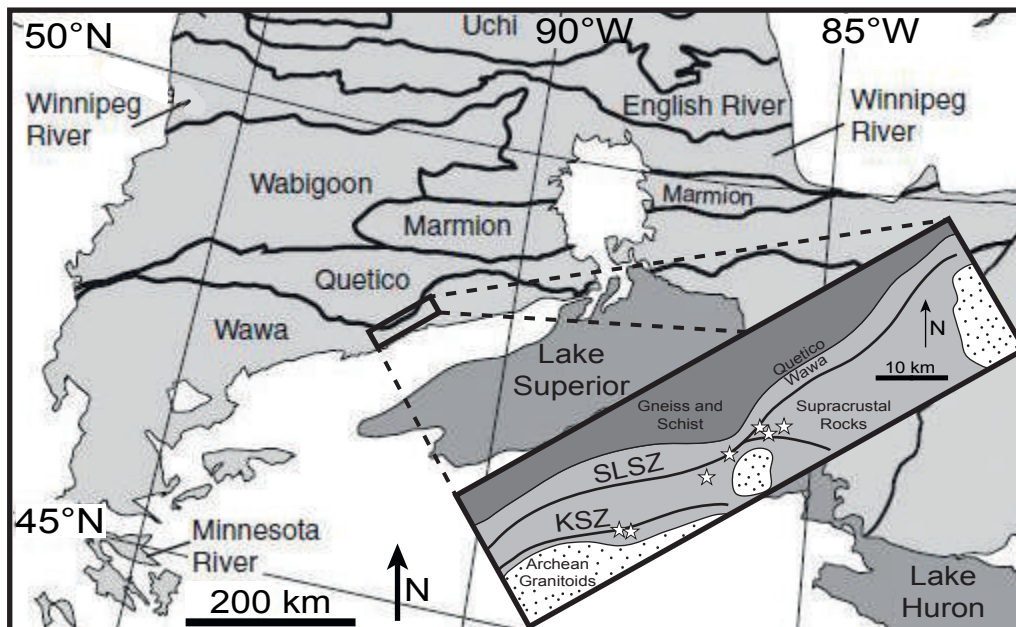


Figure 2.1. Selected subprovinces of the Superior Province, including the Wawa Subprovince. Inset: Generalized geologic map of a portion of the Vermilion District showing the location of the Shagawa Lake shear zone (SLSZ) and Kawishiwi shear zone (KSZ) near the boundary of the Wawa and Quetico Subprovinces. Stars mark the locations of samples used in this study. Sample coordinates located in Table 1. Modified from Thurston et al. (2008).

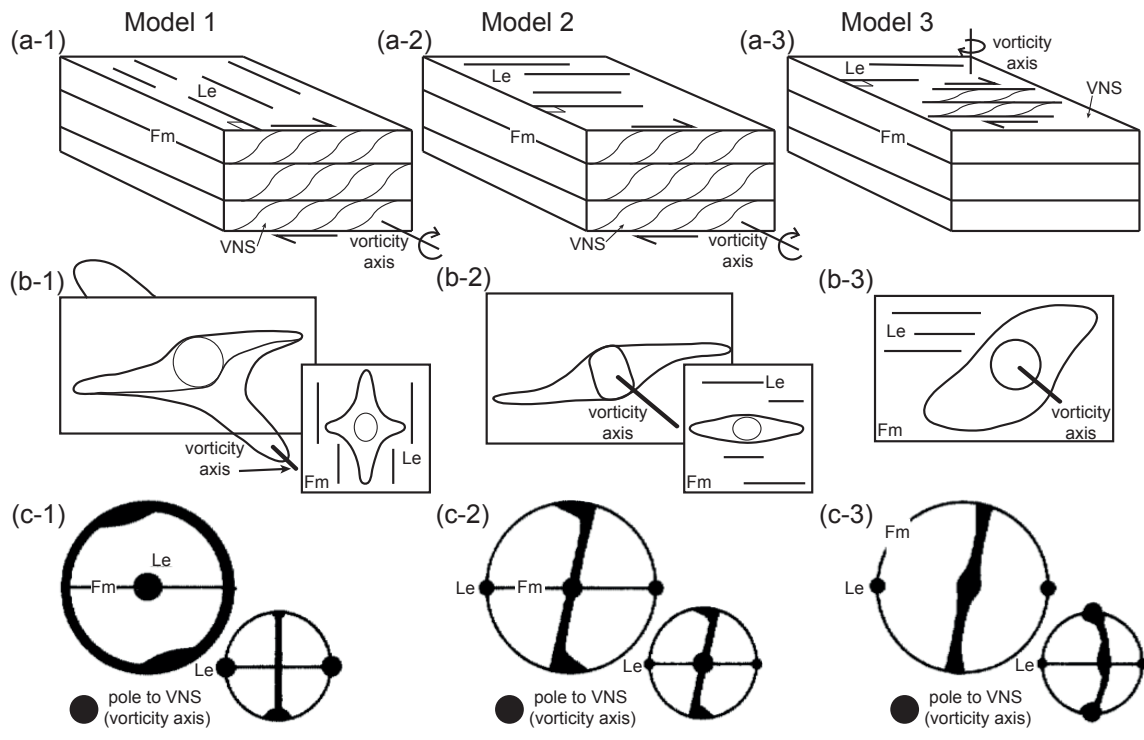


Figure 2.2. Orientation of L-S tectonite elements in three monoclinic shear models. (a) Orientation of fabric elements in the three monoclinic shear geometries. Note the relative orientations of the Fm, Le, VNS, and vorticity axis. (b) Prediction of mantled porphyroclast shapes with respect to fabric elements. (c) Low temperature c-axis preferred orientation patterns. Modified from Passchier, (1998)

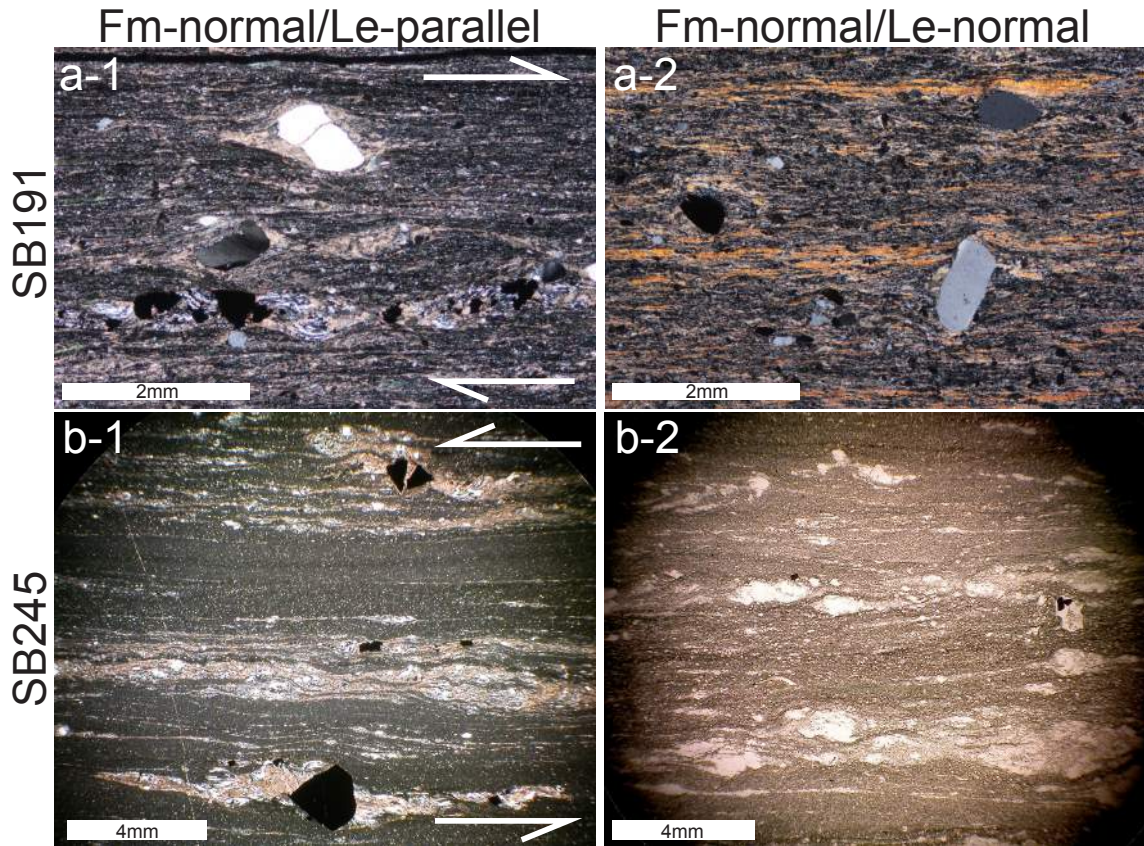


Figure 2.3. Photomicrographs of samples SB191 (row a) and SB245 (row b). Column 1 shows Fm-normal/Le-parallel photomicrographs. Column 2 shows Fm-normal/Le-normal photomicrographs (looking down Le). (a-1) Fm-normal/Le-parallel section showing pyrite clasts with asymmetric quartz/calcite-fiber strain fringes within an S-C fabric indicating a top-to-the-right shear-sense. (a-2) Fm-normal/Le-normal section showing plagioclase and pyrite clasts within a relatively symmetric microstructural fabric. (b-1) Fm-normal/Le-parallel section showing pyrite grains with asymmetric quartz/calcite-fiber strain fringes indicating a top-to-the-left shear-sense. (b-2) Fm-normal/Le-normal section; quartz and plagioclase clasts display dominantly symmetric microstructural fabric within an undifferentiated matrix. Sample orientations are listed in Table 2.1.

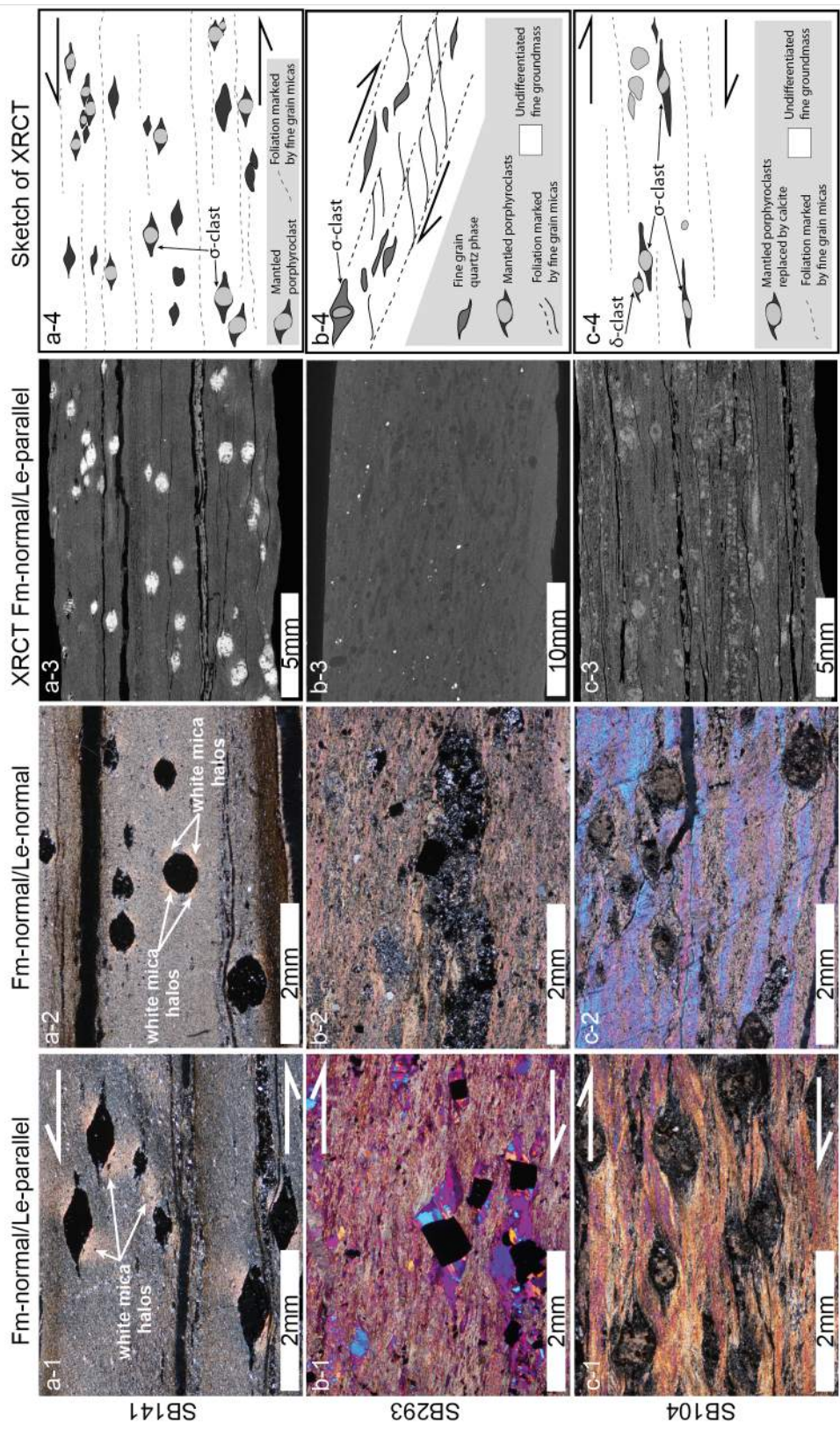


Figure. 2.4. Photomicrographs of samples SB141 (row a), SB293 (row b), and SB104 (row c). Column 1 shows Fm-normal/Le-parallel photomicrographs. Column 2 shows Fm-normal/Le-normal photomicrographs (looking down Le). Column 3, XRCT images in the Fm-normal/Le-parallel view. Column 4, sketches of XRCT images and shear-sense interpretation illustrating foliation, mantled porphyroclasts, and deformed grains. (a-1) Section showing sigmoidal porphyroclasts with asymmetric white-mica halos indicating a top-to-the-left shear-sense; (a-2) section showing ovoid porphyroclasts with symmetric white-mica halos; (a-3) view showing sigmoidal mantled porphyroclasts (white) within a fine matrix of mica, quartz, and plagioclase feldspar (grey). (a-4) Kinematic interpretation of a-3 indicating a top-to-the-left shear-sense. (b-1) section showing roughly rectangular pyrite clasts with asymmetric quartz-fiber strain fringes; (b-2) section showing pyrite clasts without strain fringes; (b-3) view showing sigmoidal mantled porphyroclasts and a deformed fine-grain quartz phase (dark grey) within an undifferentiated fine matrix of mica, quartz, and plagioclase feldspar (light grey). (b-4) Kinematic interpretation of b-3 indicating a top-to-the-right shear-sense. (c-1) Section showing asymmetric sigmoidal porphyroclasts replaced by calcite within a fine-grain mica matrix. Micas define a S-C fabric indicating top-to-the-right shear-sense; (c-2) section showing porphyroclasts without a dominate S-C fabric, (c-3) view showing sigmoidal mantled porphyroclasts (light grey) within an fine matrix of mica (light grey). (c-4) Kinematic interpretation of c-3 indicating a top-to-the-right shear-sense. Sample orientations are listed in Table 2.1.

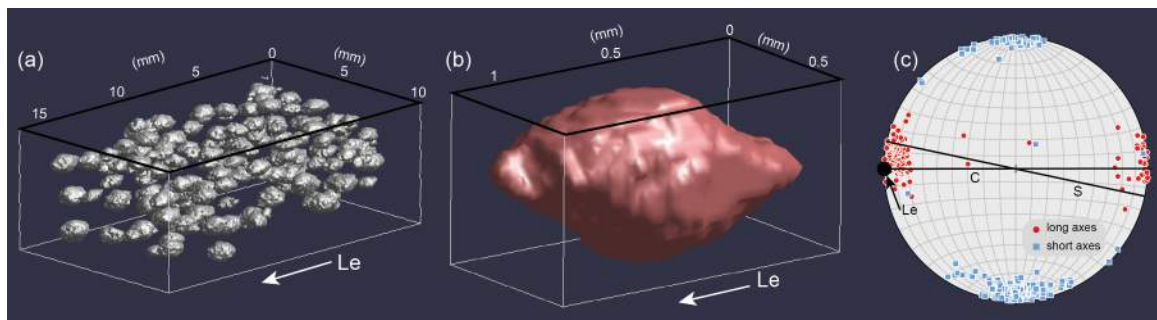


Figure 2.5. 3D-surfaces of porphyroclasts in SB141 generated from BLOB3D. (a) 3D-surfaces of sigmoidal pyrite porphyroclasts replaced by iron-oxide. (b) 3D-surface of an individual sigmoidal porphyroclast replaced by iron-oxide. Black outlines mark Fm orientation and white arrows mark Le orientation. (c) Lower-hemisphere equal-area stereonet (Fm-normal/Le-parallel view) with long-axis (dots) and short-axis (squares) orientations of porphyroclasts. Orientation of C-foliation, S-foliation, and Le as shown.

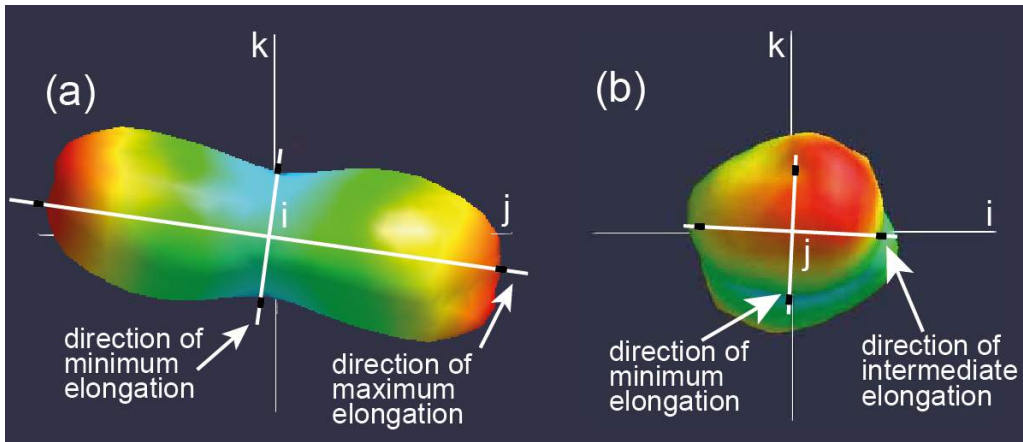


Figure 2.6. 3D-rose diagrams showing relative SVD component magnitudes and eigenvectors representing strain axes generated in QUANT3D for porphyroclasts from SB141. (a) Fm-normal/Le-parallel view; (b) Fm-normal/Le-normal view. (i,j,k) coordinates are for illustrative purposes only.

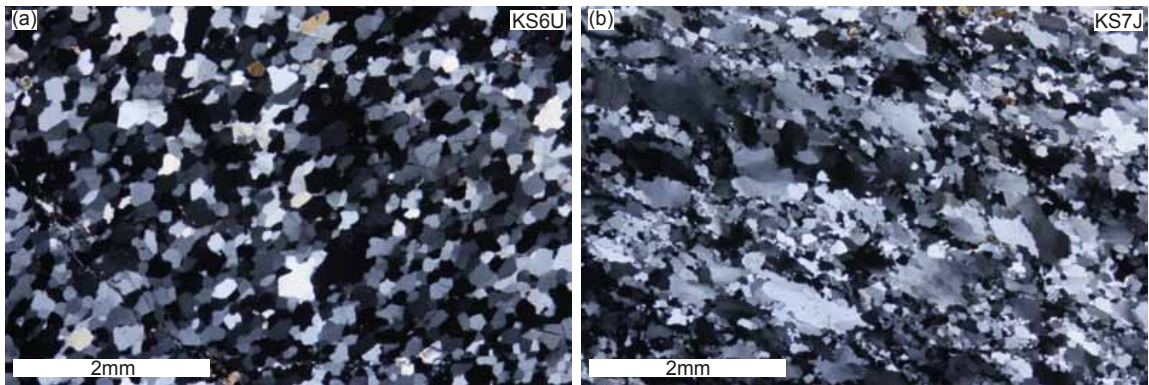


Figure 2.7. Fm-normal/Le-parallel photomicrographs of quartz-rich samples (a) KS6U and (b) KS7J.

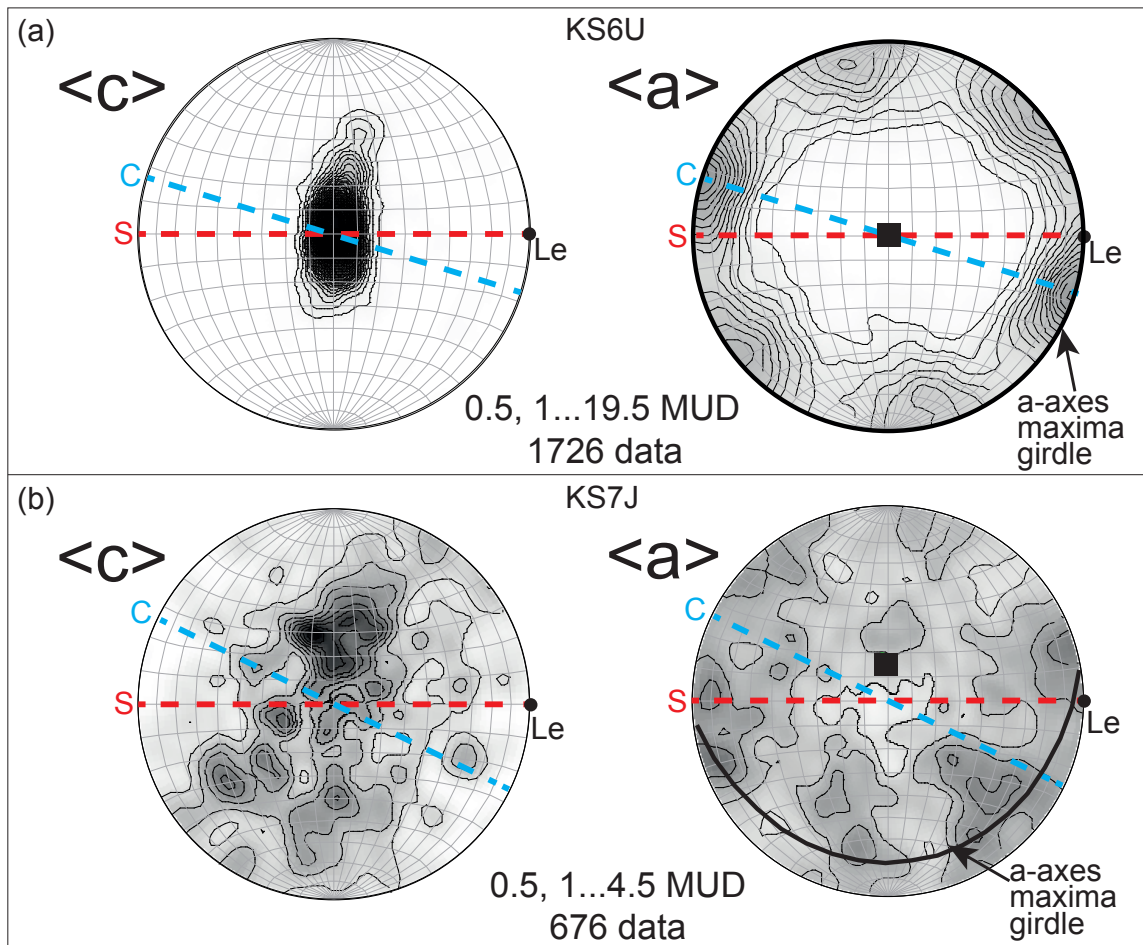


Figure 2.8. Quartz c- and a-axis CPO data for (a) KS6U and (b) KS7J. All data are shown in Fm-normal/Le-parallel views; S-foliation, C-foliation, and Le as indicated. Black great circles represent best-fit a-axis maxima girdles with poles (black squares). Contours are multiples of uniform density (MUD).

3. Structural and kinematic analysis of the eastern Shagawa Lake shear zones, NE Minnesota: Implications for assembly of the southern Superior Province.

3.1. Introduction

Mechanisms governing assembly of the Archean Superior Province remain highly contested. The North American Superior Province is comprised of a series of ENE-trending linear subprovinces with juxtaposed regions of low-grade granite-greenstones against regions of high-grade gneiss and schist (Fig. 3.1). Proposed models for the assembly of the Superior province can be broadly group into three categories: (1) vertical tectonic scenarios involving crustal convective overturn or coupled granitoid diapirism and greenstone sagduction (e.g., Lin, 2005; Parmenter et al., 2006; Bedard et al., 2003, 2006; Harris and Bedard, 2014); (2) plate tectonics scenarios involving accretion of oceanic, volcanic arc, or ocean plume terranes, and/or volcanic arc and/or plume magmatism (e.g., Drury et al., 1984; Windley, 1984; Davis et al., 1988; Card, 1990; Williams, 1990; Desrochers et al., 1993; Kimura et al., 1993; de Wit, 1998; Kusky, 1998; Kusky and Polat, 1999; Lowe, 1999; Daigneault et al., 2002; Chown et al., 2002; Percival et al., 2004); and (3) channel flow induced collapse within a ductile lower crust (Perchuk and Gerya, 2011; Harris et al., 2012). Structural and kinematic histories of shear zones along subprovince boundaries might provide critical clues to the processes responsible for crustal assembly of the Superior Province.

The Vermilion District of NE Minnesota contains multiple shear zones in close proximity to the Quetico/Wawa Subprovince boundary. The displacement history of several of these shear zones remains unconstrained. These shear zones generally form

NE- to ENE-striking, sub-vertical zones of L-S tectonites with metamorphic foliation (Fm) generally parallel to their host zone (near vertical with ENE strike) and steep to moderately-plunging elongation lineation. These shear zones have been variably interpreted as recording (1) unidirectional dextral strike-slip shear (Hudleston et al., 1988; Bauer and Bidwell, 1990; Schultz-Ela and Hudleston, 1992) or (2) dominantly dip-slip shear parallel to elongation lineation with local subsidiary strike-parallel shear, with either or both right- and left-lateral shear (Erickson, 2008, 2010; Goodman, 2008, Karberg, 2009; Johnson, 2009). Interpretation of non-coaxial shear direction and shear-sense has first-order implications for mechanisms governing subprovince assembly within the southern Superior Province.

The topic of this contribution is the Shagawa Lake shear zone (SLSZ), an ~70 km long and ~7 km wide subvertical package of L-S tectonite in close proximity to the Quetico/Wawa Subprovince boundary (Figs. 3.1 and 3.2). The SLSZ cuts greenschist facies metavolcanic and metasedimentary rocks of the Wawa subprovince and is proximal to the Snowbank stock, a massive ovoid granitoid body (Fig. 3.2). Previous studies of the western SLSZ, which spatially overlapped in part, arrived at different conclusions from each other, with regard to non-coaxial shear direction and shear-sense. Shear zone history is currently unconstrained in the eastern SLSZ. Key questions include: (1) What displacement direction and shear-sense(s) are recorded in the eastern SLSZ? (2) Does the SLSZ record unidirectional shear or multiple shear-senses? (3) Does the SLSZ record over-printing or cross-cutting relationships between multiple shear events? In this contribution I present a detailed structural and kinematic analysis of a

portion of the eastern SLSZ and discuss the implications of these results for existing tectonics models.

3.2. Geologic setting

The Vermilion district of northeastern Minnesota, is located in the southern Superior Province and includes parts of the Quetico and Wawa Subprovinces (Figs. 3.1 and 3.2). The Quetico Subprovince is a northeast-trending belt of high-grade gneiss and schist. The Wawa Subprovince is comprised of a package of low-grade metavolcanic and metasedimentary rocks and granitoid plutons of tonalite–trondhjemite–granodiorite composition. The Vermilion District metavolcanic-metasedimentary sequences include tholeiitic pillow basalt, iron formation, and calc-alkalic volcanic rocks overlain by sequence of volcanic flows, breccia, tuff, conglomerate, sandstone, siltstone, and shale, all of which record greenschist facies metamorphism. Metavolcanic rocks range in age from 2.75 to 2.69 Ga and plutonic rocks range in age from 2.74 to 2.65 Ga (Card, 1990 and references therein). The juxtaposition of Quetico high-grade rocks against Wawa greenschist facies rocks marks the subprovince boundary (Fig. 3.2).

The Vermilion District contains multiple ENE-striking shear zones marked by subvertical packages of L-S tectonite. Shear zones occur within the metavolcanic-metasedimentary sequence, and record greenschist facies metamorphic conditions. The shear zones include: (1) the SLSZ (Fig. 3.2); (2) the Kawishiwi shear zone (Fig. 3.2); (3) the Mud Creek shear zone; and (4) the Murray shear zone.

The western portion of the SLSZ was the topic of two focused studies, each of which arrived at different conclusions. Furthest to the west, and the spatially more

focused study concluded that L-S tectonites, defined by a NE-striking subvertical Fm and moderately SW-plunging elongation lineation, record dextral shear (Fig. 3.2) (Bauer and Bidwell, 1990). In contrast, a more recent study, partially overlapping spatially with this earlier study, but extending further to the east, described a NE-striking subvertical Fm and a fanning in the orientation distribution of elongation lineation (Fig. 3.2) (Erickson, 2008, 2010). Elongation lineation plunges: steeply, moderately to the NE and moderately to the SW; gently-plunging elongation lineation occurs locally. L-S tectonites record N-side-up and S-side-up dip- to oblique-shear parallel to elongation lineation with localized left-lateral shear parallel to gently-plunging elongation lineation. Erickson's (2008, 2010) results might be rationalized to be locally consistent with the results of Bauer and Bidwell (1990) because both studies show moderately plunging lineation in similar areas.

3.3. Shagawa Lake shear zone (SLSZ)

The SLSZ is a sub-vertical package of L-S tectonites that extends for ~70 km within the Vermilion District and crosses the United States/Canadian border. The SLSZ extends from the Giant's Range batholith in the west to the Saganaga tonalite in the east (Fig. 3.2). The tectonite fabric cuts metavolcanic and metasedimentary sequences of the Vermilion District (Wawa Subprovince) and broadly parallels the Quetico/Wawa Subprovince boundary (Fig. 3.2).

Structural trajectories interpreted from LiDAR altimetry define the broad (structural) architecture of the SLSZ, and commonly correlate with Fm-trajectories determined by field measurements (Dyess and Hansen, 2014). Regionally, SLSZ Fm trajectories define a northeast trend, however as the zone approaches the Snowbank stock

from the west, Fm-trajectories diverge from the regional trend and appear to wrap around the north and southwest sides of the Snowbank stock (Fig. 3.2). North of the Snowbank stock intersecting structural trajectories stand out from the regional pattern; the region east of the Snowbank stock lacks Fm and hence structural trajectories.

3.3.1 Study area

The study area is centered on a portion of the eastern SLSZ dominated by metavolcanic and metasedimentary sequences adjacent the Snowbank stock (Fig. 3.3). Metavolcanic and metasedimentary sequences include mafic metavolcanic rocks, volcanic flows, breccia, tuff, volcanogenic lithic sandstone, conglomerate, siltstone, and shale (Jirsa et al., 2011). The Snowbank stock, which is mostly covered by Snowbank Lake, is composed of syenite and granite (Sanders, 1929). The Snowbank stock appears massive with no evidence of an L-S tectonite fabric.

The metasedimentary package displays Fm, generally marked by a grain-shape preferred orientation of muscovite, chlorite, quartz, and plagioclase. Fm is locally composed of both S and C foliations (Fig. 3.4). Compositional layering of quartz, plagioclase, calcite and muscovite and an alignment of platy minerals such as chlorite and muscovite marks S and C, respectively (Fig. 3.4). Fm dips steeply with varying strike in a coherent pattern, with Fm striking NE across the central portion of the study area and turning eastward forming an ~2 km-wide zone that wraps around the northeast side of the Snowbank stock (Fig. 3.3). Within the southwest corner of the study area, Fm appears to begin to wrap around the Snowbank stock, however the region is poorly exposed, and

LiDAR data shows no evidence of Fm in this region; therefore the geometric relationship between Fm and the Snowbank stock is unconstrained.

Fm contains a variably developed elongation lineation (Fig. 3.4). Elongation lineation occurs in two forms within the study area: (1) stretching lineations on S-surfaces (Ls) defined by elongated grains, mineral aggregates, and/or pebbles; and (2) ridge-in-groove striations on C-foliation surfaces (Lc) which have the appearance of ductile slickensides (Lin and Williams, 1992; Lin et al., 2007). Where Ls and Lc occur in the same outcrop, Ls and Lc are parallel when viewed parallel to C-foliation.

Because elongation lineation is everywhere contained within Fm, I discuss elongation lineation orientation in terms of pitch. Pitch is the angle between Fm-strike and elongation lineation measured within the Fm-plane. Because Fm is sub-vertical across the field area, high pitch values correspond to steeply-plunging or vertical lineations, and low pitch values correspond to gently-plunging or horizontal lineations. Therefore I employ five terms to describe lineation pitch: (1) horizontal (0-10°); (2) gentle (10-30°); (3) moderate (30-60°); (4) steep (60-80°); and (5) vertical (80-90°) (Fig. 3.5a). Descriptive terms are similar to terms used to describe lineation plunge. However, these descriptive terms apply to pitch in this study because elongation lineation is everywhere contained with a subvertical Fm. If Fm were not subvertical or steeply-dipping, the above pitch domain terms would not apply.

Ls and Lc display similar orientation populations. Both Ls and Lc are dominantly vertical, steeply- to moderately-pitching to the NE, and steeply- to moderately-pitching to the SW with local gentle to horizontal (Fig. 3.3a). Lineation pitch values record a splay

of orientations, however collectively 70% of Ls and Lc are steeply-pitching to vertical (Fig. 3.3b). In general, lineation orientation is consistent within individual outcrops, however, lineation orientation can vary between outcrops. I assume that the L-S tectonites are in place, that is, not reoriented by younger events given the continuity of Fm across the field area; therefore I assume that the variation in elongation lineation is not produced by a younger reorientation of the L-S tectonites but instead provides a kinematic record of the processes by which it formed. The variation in Ls and Lc orientation does not define any recognizable spatial patterns with regard to pitch across the study area, and in some cases the difference in lineation orientation in adjacent outcrops varies quite significantly. For example, locations 93A and 133A, located within 250 m of one another in the central-SW part of the map area, display steeply-SW- and moderately-NE-pitching lineations, respectively, with a 60° difference in pitch between these two locations (Fig. 3.3).

The rocks directly north and east of the Snowbank stock include volcanic flows, tuff, breccia, and conglomerate that preserve primary structures (bedding) and show no evidence of Fm or elongation lineation (Fig. 3.3). This region corresponds to the previously mentioned areas defined by intersecting structural trajectories or a lack of structural trajectories (Fig. 3.2). Although access to the rocks north of the Snowbank stock is limited, rocks east of the Snowbank stock record primary features.

3.3.2. Kinematic analysis

A goal of this study is to determine the shear zone history of the eastern SLSZ. To this end, I collected oriented L-S tectonite samples for microstructural kinematic

analysis. Sample selection was based on the presence of Fm and elongation lineation in outcrop. Outcrops with a well-developed Fm and elongation lineation were consistently sampled, whereas outcrops lacking Fm and elongation lineation were commonly not sampled. Samples were oriented relative to Fm and elongation lineation (e.g., Hansen, 1990).

The vorticity axis and vorticity-normal-section relate non-coaxial shear direction to Fm and elongation lineation within L-S tectonites (Passchier, 1998). The vorticity axis is the line about which mineral grains rotate during non-coaxial shear. The vorticity-normal-section is the plane that records the maximum asymmetric microstructural fabric, forms parallel to non-coaxial shear direction, and is the proper plane in which to interpret shear sense (Fig. 3.4) (Passchier, 1998). Geometric relationships between Fm, elongation lineation, vorticity axis, and vorticity-normal-section can vary under differing conditions. Thus it is important to determine the vorticity axis (or vorticity-normal-section) orientation as a first step in kinematic analysis of L-S tectonites. Vorticity analysis of five L-S tectonite samples from the eastern SLSZ and two samples from the Kawishiwi shear zone record kinematic data that indicate Vermilion District L-S tectonites record: (1) a vorticity axis parallel to Fm and normal to elongation lineation; (2) a vorticity-normal-section normal to Fm and parallel to elongation lineation; and (3) non-coaxial shear within the plane of Fm and parallel to elongation lineation (Dyess et al., in review). Kinematic indicators in thin-section and image slices from X-ray computed tomography consistently record asymmetric microstructural fabrics in foliation-normal lineation-parallel planes, whereas planes normal to foliation and elongation lineation display

dominantly symmetric microstructural fabrics. Mantled porphyroclast 3D-shapes and star-volume distribution analyses indicate that porphyroclast short-axes are normal to foliation and long-axes parallel elongation lineation. Quartz crystallographic preferred orientation data show a-axes maxima sub-parallel to Fm-normal elongation lineation-parallel planes. Kinematic data consistently show a vorticity axis within the foliation plane and normal to elongation lineation; thus non-coaxial shear direction is sub-parallel to elongation lineation. The data are inconsistent with shear models in which non-coaxial shear direction is normal to lineation, or in which the vorticity axis is normal to foliation. Kinematic data indicate that L-S tectonites record non-coaxial shear broadly parallel to elongation lineation; that is, tectonites with steep or vertical elongation lineation record dominantly dip-parallel shear; tectonites with gentle or horizontal elongation lineation record dominantly strike-parallel shear; and tectonites with moderate- elongation lineation record roughly equal components of dip-parallel and strike-parallel shear.

I describe non-coaxial shear direction in terms of dip-parallel and strike-parallel components. Subvertical and steeply-pitching lineations reflect dominantly dip-parallel shear, horizontal and gently-pitching lineations reflect dominantly strike-parallel shear, and moderately-pitching lineations reflect roughly equal components of dip-parallel and strike-parallel shear. I delineate four domains to describe non-coaxial shear direction: (1) strike-parallel; (2) dip-parallel; (3) oblique-NE; and (4) oblique-SW (Fig. 3.5b). I classify shear parallel to horizontal or gently-pitching lineations (i.e. pitch $\leq 30^\circ$) as strike-parallel and shear parallel to vertical or steeply-pitching lineations (i.e. pitch $\geq 60^\circ$) as dip-parallel. Shear parallel to elongation lineations with pitch between 30° and 60° to

the NE or SW is classified as oblique-NE and oblique-SW, respectively.

I performed a petrographic microstructural kinematic analysis of L-S tectonites in order to determine shear-sense. Thin-sections were cut parallel to the vorticity-normal-section, that is, the plane normal to Fm and parallel elongation lineation (Fig. 3.4 and 6a). I examined microstructural fabrics in each thin-section using a petrographic microscope; microstructures are classified according to the classification scheme defined by Passchier and Trouw (2005). I determined a shear-sense for each sample and ranked all kinematic interpretations with a confidence value from low (one) to high (five) confidence (e.g., Hansen, 1989). The confidence index is based on the type of kinematic indicator, the clarity or intensity of development of asymmetric fabric, and the number of different kinematic indicators preserved within samples from a single location. Ratings of 4 and 5 are highly trustworthy, whereas a rating of 1 reflects a potentially ambiguous interpretation.

I used a variety of microstructures to determine shear-sense, all of which are consistent with greenschist facies metamorphic conditions, consistent with the suggestion that deformation accompanied metamorphism. The most useful microstructures include sigmoidal-mantled porphyroclasts, white mica halos, quartz/calcite strain fringes, and S-C fabrics; these structures could occur individually or collectively in any particular sample. Samples with multiple types of microstructures recording similar shear-sense were awarded higher confidence ratings.

All told I collected 176 oriented samples, 38 of which displayed microstructures that could be interpreted with some level of confidence. Sample details are given in Table

1. The samples show a range of elongation lineation orientation, with 27 recording dip-parallel shear, 2 recording strike-parallel parallel, and 6 and 4 samples, respectively, recording oblique-NE- and oblique-NW-shear. Photomicrographs of six samples with high confidence level are illustrated in Figure 3.6, and described briefly below.

Sample 141A, an iron-carbonate schist, consists of a fine undifferentiated matrix of white-mica, carbonate, plagioclase feldspar, and quartz, with white-mica defining Fm (Fig. 3.6b). Sample 141A includes mantled iron oxide replaced porphyroclasts that range from 0.5 – 2 mm long and show σ -geometry with SE-side-up shear. Asymmetric white-mica halos, adjacent to the porphyroclasts, also record SE-side-up shear.

Sample 293A, a white-mica schist, consists of an undifferentiated matrix of white-mica, chlorite, calcite, quartz, and plagioclase feldspar (Fig. 3.6c). Sample 293A includes pyrite clasts (<0.5 mm) and quartz and plagioclase feldspar clasts (< 3 mm). A grain-shape preferred orientation of chlorite and calcite define an asymmetric S-C fabric and, quartz-fiber strain fringes occur adjacent to several pyrite grains. Both the S-C fabric and fringe shapes are consistent with S-side-up shear.

Sample 104A, an iron-carbonate schist, consists of a fine-grained matrix of undifferentiated white-mica, chlorite, carbonate, plagioclase feldspar, and quartz (Fig. 3.6d). Sample 104A includes mantled porphyroclasts replaced by calcite. A grain-shape preferred orientation of white-mica defines an S-C fabric consistent with SE-side-up non-coaxial shear. Porphyroclasts range from 0.5 – 1 mm across with mantles of fine white-mica and quartz. Mantles are of σ -geometry consistent with a SE-side-up shear-sense.

Sample 191A, a fine-grained mica schist, consists of an undifferentiated matrix of white-mica, chlorite, calcite, plagioclase, and quartz, containing pyrite and plagioclase clasts (Fig. 3.6e). Grain-shape preferred orientation of white-mica, chlorite, and calcite define Fm. Several independent microstructures record N-side-up shear parallel to a steeply plunging elongation lineation, and thus this sample is assigned a confidence level of 5. Shear sense indicators include: S-C fabrics, elongate plagioclase feldspar clasts (up to 1 mm long) surrounded by calcite mantles with σ -geometry, and pyrite clasts (up to 0.5 mm across) with asymmetric quartz-fiber strain fringes.

Sample 245A, a fine-grained mafic metavolcanic rock, consists of an undifferentiated matrix of chlorite, plagioclase feldspar, amphibole, and calcite, containing pyrite clasts (Fig. 3.6f). A grain-shape preferred orientation of chlorite, and calcite defines Fm. No obvious asymmetric microstructural fabrics are visible within the dark matrix material. Pyrite clasts (up to 2 mm across) with asymmetric strain fringes of quartz and calcite fibers consistently record with N-side-up shear.

Sample 318A, an iron-carbonate schist, consists of a fine undifferentiated matrix of white-mica, carbonate, plagioclase feldspar, and quartz; white-mica, quartz, and plagioclase grain shape preferred orientation of define Fm. Fm is oriented 068, 89SE and contains an Lc pitching 80°W (Table 1). Fm is deformed by a crenulation, defined by asymmetric folds with hinge lines parallel to Fm and roughly normal to Lc (Fig. 3.7). Crenulations occurs at a macroscopic scale with spacing ranging from 2-28 cm and at the microscopic scale (Figs. 3.7b, 3.7c, and 3.7d). Calcite commonly fills crenulation hinges; both the asymmetry of the crenulations and the calcite fill (marking local extension) are

consistent with SE-side-up shear, parallel to the elongation lineation, or normal to the crenulation axis.

Microstructural kinematic analysis of the SLSZ tectonites reveals several first-order relationships between sample locations with differing shear-sense. Each of the 38 sample analyzed represents a specific location within the study area. Of those 26 samples with dip-parallel shear, 12 samples record N-side-up shear and 14 samples record S-side-up shear (Table 1). Two samples record strike-parallel shear—both recording dextral shear. Of the 4 samples that record oblique-SW shear, 3 record N-side-up/right-lateral shear components and 1 records S-side-up/left-lateral shear components. Of the 6 samples that record oblique-NE shear, 2 record N-side-up/left-lateral shear components, 3 record S-side-up/right-lateral shear components, and 1 records S-side-up/left-lateral shear components (Table 1). Collectively the shear recorded across the field area defines no coherent spatial pattern (Fig. 3.3). Samples that record dip-parallel to oblique shear with N-side-up and S-side-up shear-sense display no recognized spatial patterns across the study area, nor do samples with strike-parallel shear. Furthermore, samples within close proximity to one another locally record opposite shear directions (Fig. 3.3). For example, samples 318A (confidence level 4) and 70A (confidence level 3) record steeply-pitching Lc, opposite shear-senses, and were collected within 250 m of each other (Fig. 3.3; Table 1). In addition, neighboring L-S tectonite samples recording opposite shear-sense do not record visible cross-cutting microstructural fabrics.

Both macro- and microscopic structures indicate that SLSZ L-S tectonites record a progressive deformation with non-coaxial shear parallel to elongation lineation

regardless of lineation geographic orientation. This relationship, combined with the fan of lineation orientations, indicates that the direction of non-coaxial shear is not unidirectional across the study area. That is, non-coaxial shear direction varies across the study area. Although no coherent pattern of shear emerges, the variation in shear direction is not random; in general shear occurred in a plane normal to Fm and broadly in a down-dip, as opposed to strike-parallel (Fig. 3.3). Non-coaxial shear direction is dominantly dip-parallel to oblique, and therefore the SLSZ records dominantly dip- to oblique-slip. Similar to elongation lineation orientation, I recognize no coherent spatial pattern in non-coaxial shear (Fig. 3.3).

Evidence for strike-parallel shear is limited to a few samples or localized zones. Although, the two samples containing strike-parallel elongation lineation record right-lateral shear, of the 10 samples containing oblique-NE or oblique-SW elongation lineation, 6 record right-lateral a shear component and 4 record a left-lateral shear component. Overall the eastern SLSZ records no evidence for ubiquitous unidirectional dip-slip or strike-slip shear.

The SLSZ is defined by a package of L-S tectonite comprised of a dominantly NE-striking steeply-dipping Fm and vertical, steep, and moderately-pitching elongation lineation. Non-coaxial shear direction is parallel to elongation lineation, thus non-coaxial shear direction is dip-parallel to oblique. Individual SLSZ L-S tectonites record N-side-up, S-side-up, right-lateral, and left-lateral shear. Despite the different shear-senses recorded in different tectonites within the SLSZ, these tectonites do not record clear overprinting or cross-cutting relationships. Thus, the picture that emerges is one in which the

SLSZ is best described as zone of localized ductile shear in which the shear was dominantly dip-parallel to oblique, yet without a consistent shear-sense, that is, neither NW-side-up, nor SE-side-up shear occurs across eastern SLSZ. In addition there are no discernable patterns in shear sense across or within the eastern SLSZ, such as NW-side-up on one side and SE-side-up on the other.

3.4. Discussion

Structural and kinematic data from the eastern SLSZ and other Vermilion District shear zones provide a coherent structural and kinematic picture of the Vermilion District. Other Vermilion District shear zones include the western SLSZ, Kawishiwi shear zone, southwest of the study area, and Mud Creek and Murray shear zones west of the SLSZ.

3.4.1. Western Shagawa Lake shear zone

The western SLSZ marks a zone, ~5-7 km wide and ~30 km long, which lies west of the study area (Bauer and Bidwell, 1990; Erickson, 2008, 2010). The western SLSZ strikes NE and dips steeply, with Fm parallel to the shear zone (Fig. 3.2). Local zones of L-S tectonite with moderate-SW- Lc striations record dextral shear (Bauer and Bidwell, 1990). More broadly, elongation lineation is vertical, steep, and moderately-pitching to the NE and SW with local gentle and horizontal (Erickson, 2008, 2010). L-S tectonites record both N-side-up and S-side-up shear with a localized left-lateral horizontal displacement component. Locally S-side-up shear predates N-side-up shear (Erickson, 2008, 2010).

3.4.2. Kawishiwi shear zone

The Kawishiwi Lake shear zone marks a zone, ~5-8 km wide and ~30 km long, which lies southwest of the study area (Goodman, 2008). Fm strikes ENE and dips steeply (Fig. 3.2) (Goodman, 2008). Elongation lineation exhibits a bimodal orientation (pitch) distribution marked by a dominant a down dip ($90^\circ \pm 40^\circ$) population and a subsidiary along-strike ($0^\circ \pm 30^\circ$) population. Structural mapping and kinematic analysis of oriented samples from the Kawishiwi shear zone provide spatial patterns, kinematic constraints, and temporal relations within the Kawishiwi shear zone. L-S tectonites with down-dip elongation lineation record both N-side-up and S-side-up shear. L-S tectonites with along-strike elongation lineation are limited to localized zones and record right-lateral shear (Goodman, 2008). Within the Kawishiwi shear zone strike-parallel shear post-dates dip-parallel shear. The strike-parallel shear, which occurs in narrow localized zones, many have been accompanied by high fluid activity (Goscinak, 2014).

3.4.3. Mud Creek shear zone

The Mud Creek shear zone marks a zone, ~4-7 km wide and ~16 long, along the Quetico/Wawa Subprovince boundary to the west of the SLSZ (Hudleston et al., 1988). Fm strikes ENE and dips steeply. Elongation lineation ranges from vertical to moderately-pitching to the E and W. Elongation lineation pitch values exhibit a splayed orientation distribution with a population centered at a pitch of 80° west (Karberg, 2009). Strain analysis of Mud Creek conglomerates indicates both flattening and constriction; the direction of maximum finite elongation parallels elongation lineation, and direction of minimum finite elongation is normal to Fm (Hudleston et al., 1988; Schultz-Ela and Hudleston, 1991). L-S tectonites record both N-side-up and S-side-up shear parallel to

steeply-pitching elongation lineation, and both right-lateral and left-lateral shear parallel to gently-pitching elongation lineation (Karberg, 2009).

3.4.4. Murray Shear zone

The Murray shear zone marks a zone ~1-4 km wide and ~19 km long. The zone and Fm strikes E and dip steeply. Within the Murray shear zone, elongation lineation is vertical to steep. L-S tectonites record N-side-up, S-side-up, and flattening shear (Johnson, 2009). As in the other shear zones, shear parallel elongation lineation, and although elongation lineation is consistently down-dip, there is there is no dominate shear direction—both N-side-up and south-side-up shear are recorded.

Collectively, Vermilion District shear zones are marked by ENE-striking subvertical packages of L-S tectonite with high length to width ratios. Fm strikes ENE, dips steeply, and is regionally consistent. Within Fm, pitch of elongation lineation is vertical, steep, moderately-pitching to the NE and SW, and gentle to horizontal within individual shear zones. Gentle and horizontal elongation lineations are relatively few in number and restricted spatially. The Murray shear zone records only vertical to steep elongation lineation. L-S tectonites record dip-parallel, oblique, and strike-parallel shear accommodated by a combination of N-sided-up, S-side-up, right-lateral, and left-lateral shear. Neither non-coaxial shear direction nor shear-sense is consistent within or across individual shear zones. Locally, cross-cutting relationships indicate that S-side-up shear pre-dates N-side-up shear (SLSZ) or that strike-parallel shear post-dates dip-parallel shear (Kawishiwi shear zone); however, cross-cutting relationships are few in number and inconsistent from shear zone to shear zone.

Previous studies that characterized strain within some of the Vermilion district shear zones do not specifically address the issue of vorticity relative to Fm and elongation lineation, a critical component to kinematic interpretation of L-S tectonites. Strain data indicating that the direction of maximum finite elongation parallels elongation lineation and direction of minimum finite elongation is normal to Fm are consistent with our structural and kinematic data. However, the interpretation of Vermilion District L-S tectonites as recording unidirectional dextral strike-slip shear is inconsistent with regional lineation orientation and data indicating non-coaxial shear direction is parallel to elongation lineation.

3.5. Implications and evaluation of tectonic models

Structural and kinematic data from the eastern SLSZ impose certain requirements on models for crustal assembly of the Superior Province. Key structural and kinematic data include: (1) a relatively consistent subvertical Fm parallel to the Quetico/Wawa Subprovince boundary; (2) a dominantly vertical to steep elongation lineation with a splay of orientations; (3) L-S tectonites that record non-coaxial shear parallel to elongation lineation despite varying lineation orientation; (4) L-S tectonites that record consistent shear-sense within individual outcrops and differing shear-sense between outcrops; (5) the presence of N-side-up, S-side-up, right-lateral, and left-lateral shear; and (6) roughly isobaric/isothermal greenschist facies metamorphic conditions. Proposed tectonic models for assembly of the southern Superior Province must account for these structural and kinematic data.

The various tectonic models for assembly of the southern Superior Province invoke either dominantly vertical and/or horizontal mechanisms for reorganization of the crust and for subprovince assembly. Proposed models for the assembly of the Superior province can be broadly group into three categories: (1) vertical tectonic scenarios involving crustal convective overturn or coupled granitoid diapirism and greenstone sagduction (e.g., Lin, 2005; Parmenter et al., 2006; Bedard et al., 2003, 2006; Harris and Bedard, 2014); (2) plate tectonics scenarios involving accretion of oceanic, volcanic arc, or ocean plume terranes, and/or volcanic arc and/or plume magmatism (e.g., Drury et al., 1984; Windley, 1984; Davis et al., 1988; Card, 1990; Williams, 1990; Desrochers et al., 1993; Kimura et al., 1993; de Wit, 1998; Kusky, 1998; Kusky and Polat, 1999; Lowe, 1999; Daigneault et al., 2002; Chown et al., 2002; Percival et al., 2004); and (3) channel flow induced collapse within a ductile lower crust (Perchuk and Gerya, 2011; Harris et al., 2012). Below I evaluate each of these tectonic models and discuss implications for assembly of the southern Superior Province.

3.5.1. Sagduction-diapirism and crustal overturn

Sagduction-diapirism refers to the process by which dense greenstones sink adjacent to rising granitoid diapiric domes (Lin, 2005; Parmenter et al., 2006; Bedard et al., 2003, 2006; Harris and Bedard, 2014). Crustal overturn refers to the process by which production of less dense granitoid material beneath a dense layer of greenstones causes a vertical reorganization of the crust (e.g., Bedard, 2006). Both sagduction-diapirism and crustal overturn models invoke a density driven, dominantly vertical reorganization of Archean crust, and both make similar structural predictions.

Sagduction-diapirism/crustal overturn models predict the formation of (1) narrow belts of metavolcanic and metasedimentary rock (greenstones) between ovoid granitoid domes producing a dome-and-keel pattern in map-view; (2) L-S tectonite packages within the greenstones that strike parallel to granitoid/greenstone boundaries; (3) foliation triple-points; and (4) consistent greenstone-down/granitoid-up shear (McGregor 1951; Anhaeusser et al. 1969; Collins et al. 1998; Chardon et al. 2002, 2008; Hickman 2004; Rey et al. 2003; Van Kranendonk et al. 2004; Robin and Bailey 2009).

Although, Vermilion district shear zones record a dominant component of vertical displacement, it is unlikely that sagduction-diapirism/crustal overturn processes are responsible for formation of the L-S tectonite fabrics. If the eastern SLSZ represented a granitoid-greenstone boundary, then the eastern SLSZ should record consistent north-side-up shear recording sinking of the greenstone sequence (Wawa Subprovince) adjacent to rising of granitoids within the Quetico Subprovince. Structural and kinematic data from the eastern SLSZ do not record consistent N-side-up shear.

Sagduction-diapirism/crustal overturn models also predict the formation of concentric L-S tectonite around granitoid bodies with L-S tectonites recording a consistent granitoid-up greenstone-down shear-sense. I recognized no Fm or elongation lineation east of the Snowbank stock; furthermore L-S tectonites closest to the Snowbank stock do not record consistent Snowbank stock-up shear (generally s-side up) as predicted by sagduction-diapirism/crustal overturn models. In addition, there are no recognized foliation triple-points in the field area, and, to our knowledge, no foliation triple-points have been described within the Vermilion District.

3.5.2. *Plate tectonic/terrane accretion models*

Plate tectonic/terrane accretion models postulate that the Superior Province subprovinces are assembled by accretion of terranes to a growing continental block due to subduction of oceanic lithosphere; individual subprovinces represent accreted volcanic arcs, or oceanic plateaus, variably modified by volcanic arc or plume processes after accretion. Although details of terrane composition and timing might vary between models, plate tectonic/terrane accretion models predict the formation of unidirectional dip-slip shear zones that record significant pressure-temperature gradients across shear zones or unidirectional strike-slip shear zones at terrane boundaries. Differences in predicted shear zone displacement are based on differences in predicted subduction style (i.e. subduction normal to the plate-margin or oblique subduction).

Plate-tectonic/terrane accretion models calling for subduction normal to the plate margin predict the formation of unidirectional dip-slip shear zones that record significant pressure-temperature gradients across shear zones. Vermilion District shear zones record multiple shear directions and shear-senses, and do not record unidirectional dip-slip. Although shear is largely dip-parallel, Vermilion District shear zones record N-side-up, S-side-up, right-lateral, and left-lateral shear within one broad event (i.e. not two or more distinct crosscutting unidirectional shear events.) Despite accommodating significant dip-slip to oblique slip, the SLSZ and Vermilion District shear zones record broadly isobaric and isothermal greenschist facies metamorphic conditions. Plate-tectonic/terrane accretion models predict the formation of significant pressure-temperature gradients across shear zones. For example, a 5 km-wide vertical shear zone with unidirectional

shear strain of 2 would accommodate 10 km of vertical displacement across the shear zone; given a 25 °C/km geothermal gradient, the shear zone should record a 250 °C change across its 5 km structural thickness. To our knowledge there is no documentation of this magnitude of thermal gradient across the SLSZ, nor do the L-S tectonites considered in this study record such a thermal gradient.

Terrane accretion as a result of oblique subduction is one possible way to reconcile the terrane accretion process with the roughly isobaric/isothermal conditions recorded within Vermilion District shear zones. Terrane accretion through oblique subduction predicts partitioning of strain into unidirectional dip-slip shear zones at trench and unidirectional strike-slip shear zones through the accretionary complex (Jarrard, 1986). Accreted terranes might record roughly isobaric/isothermal conditions because shear zone displacement is dominantly strike-parallel along terrane boundaries. Vermilion District shear zones were previously interpreted as dextral strike-slip shear zones formed as a product of terrane accretion via oblique subduction, an interpretation held up as evidence for plate tectonic processes in Archean (Hudleston et al., 1988; Sleep, 1990; Jirsa et al., 1992).

As previously stated, the eastern SLSZ records a broad deformation event characterized by shearing in multiple directions with multiple shear-senses, and does not record partitioned zones of unidirectional dip-slip or strike-slip. If Vermilion District shear zones did record significant amounts of strike-slip displacement, then L-S tectonites should record a gentle to horizontal elongation lineation within individual shear zones or across shear zones; and shear should be consistently left-lateral or right-lateral across the

entire SLZS. In contrast to these predictions, elongation lineation is broadly vertical to steeply-pitching with Vermilion District shear zones, and shear is dominantly dip-parallel to oblique with both N-side-up and S-side-up shear, local strike-parallel shear—with both right-lateral and left-lateral shear.

Plate tectonic/terrane accretion models also require crust that is rheologically strong enough to support the existence of rigid lithospheric plates. Numerical modeling of Earth's early cooling history postulates that Archean crust was ~2-3 times warmer and ~5-8 times weaker than present (Rey and Coltice, 2008). Further numerical modeling postulates that a significantly warm Archean crust would be weakened by emplacement of sub-lithospheric melts and therefore would be too weak to initiate self-sustaining one-sided subduction (Sizova et al., 2010).

3.5.3. Rheological implications

Structural and kinematic data from the eastern SLSZ and other Vermilion District shear zones have first-order rheological implications. Broadly, Vermilion District shear zones record single shear events; however, these events accommodate a multitude of shear directions, including dominantly dip- to oblique-slip with localized areas of strike-slip. Dip-slip shear accommodated both both N-side-up and S-side-up shear. Localized strike-slip shear occurred as both right-lateral and left-lateral shear. Shearing occurring under roughly isobaric/isothermal conditions. Collectively these results raise a key question. How can Vermilion District shear zones accommodate dominantly dip-slip displacement without recording significant gradients in pressure/temperature conditions?

In the case of rheologically weak crust, one might expect that as the crust is

deformed into various domains that would slide past other domains, perhaps focused by small (and changing) differences in local rheology (due to composition, fluids, strain history, anisotropy, etc.) in a way that accommodates the overall strain across the zone of deforming crust. Depending on the broader tectonic environment, displacement might be dominantly dip-parallel, or strike-parallel. In the case of the SLSZ and other Vermilion District shear zones, it appears that such a deformation was dominantly dip-parallel, with localized zones of strike-parallel shear. Given that the deformation would be accommodated by opposite slip direction across various domains, the entire package would result in shortening, but with little change in crustal level across the shear zone; thus such deformation would occur within isobaric/isothermal conditions, and the resulting tectonites would not record pressure/temperature gradients.

Vermilion District shear zones are wider than Proterozoic greenschist facies shear zones. At high metamorphic grades, middle amphibolite to granulite facies, shear zones widen due to softening of the wall rock whereas at cooler greenschist to lower-amphibolite facies shear zones are weaker than the wall rocks producing discrete relatively narrow (<1.5 km wide to tens of meters wide) shear zones (e.g. Hammer et al., 1992; Davidson et al., 1995). Vermilion District shear zones range in width from ~1-8 km; where individual shear zones are adjacent, the cumulative width of L-S tectonite packages exceeds 10 km (Fig. 3.2), an order of magnitude wider than some Proterozoic greenschist facies shear zones (e.g. Hammer et al., 1992; Davidson et al., 1995). Broadly Vermilion District L-S tectonites record ductile deformation at greenschist facies metamorphic conditions across relatively large areas.

The rheological requirement set forth by the structural and kinematic data that deformation took place with a weak crust and relatively large shear zone widths seem to be at odds with the consistent greenschist facies metamorphic conditions recorded across the Vermilion District. However, these data could be reconciled if the Neoproterozoic crust was warmer than modern crust. Numerical modeling of Earth's early cooling history postulates that Archean crust was ~2-3 times warmer than present crust (Rey and Coltice, 2008). Such warming would produce a Neoproterozoic crust ~5-8 times weaker than modern crust and possibly increase shear zone width by reducing the rheological contrast between the shear zone and wall rocks. In the context of this rheologically weak crust, I can reconcile the structural and kinematic data with the roughly isobaric/isothermal greenschist facies metamorphic conditions and relatively large shear zone widths. Suggested tectonic models for the formation of the Vermilion District shear zones must accommodate deformation within a rheologically weak crust at roughly isobaric/isothermal greenschist facies metamorphic conditions.

3.5.4. Channel flow induced collapse during regional shortening

Channel flow induced collapse of a rheologically weak crust during regional shortening may provide a mechanism for subprovince assembly and the rheological conditions required by structural and kinematic data from the eastern SLSZ. Channel flow models predict that subprovince assembly is driven by exhumation of ductile high-grade crustal material to shallow crustal levels juxtaposing linear belts of high-grade material (Quetico Subprovince) against low-grade granite-greenstone sequences (Wawa Subprovince). Channel flow is referred to here as the lateral flow of a weak, viscous

crustal layer between relatively rigid yet deformable bounding crustal slabs due to a horizontal gradient in lithostatic pressure created by differences in crustal thickness or by erosion and focused denudation (Godin et al., 2006; Grujic, 2006). Silicone box models representing channel flow induced collapse during regional shortening provide a broad three-step sequence of events for subprovince assembly (Fig. 3.8) (Duretz et al., 2011; Harris et al., 2012). At time 1, regional layer-parallel shortening produces thickening and folding of the greenstone layer allowing lower ductile crust to flow into anti-formal crests along with indentation of the lithospheric mantle into the lower ductile crust (Fig. 3.8 a). Erosion of the thickened greenstone layer during time 2 decreases the lithostatic load allowing for the exhumation of relatively high-grade, felsic ductile material to shallow crustal levels at time 3 (Figs. 3.8b and 3.8c). The result of this exhumation is the juxtaposition of low-grade granite-greenstone sequences and relatively linear belts of high-grade felsic gneissic rocks (Fig. 3.8d) (Harris et al., 2012). This juxtaposition of low-grade granite-greenstones and high-grade felsic gneisses is similar to the juxtaposition low-grade (i.e., Wawa) and high-grade (i.e., Quetico) subprovinces within the Superior Province with the boundary between the exhumed high-grade crust and low-grade granite-greenstones representing a subprovince boundary (Fig. 3.8d).

Rheological conditions required by structural and kinematic data from Vermilion District shear zones are consistent with the rheological requirements of the channel flow model. During regional shortening and exhumation of high-grade crustal material, deformable greenstone sequences adjacent to exhumed high-grade crustal material could accommodate shortening by broad non-coaxial shear in multiple directions with multiple

shear-sense. I expect such a shear event to produce: (1) a regionally consistent steeply-dipping Fm parallel to the subprovince boundary; (2) variable elongation lineation orientation; (3) variable shear-senses indicators, and (4) isobaric/isothermal greenschist facies metamorphic conditions. Effectively, various crustal domains would slide past one another without significant changes in crustal level.

Structural features predicted by the channel flow model are consistent with the structural and kinematic data of this study and from other Vermilion District shear zones. The channel flow model provides a tectonic setting for deformation within a weak crust and accounts for the presence of a range of elongation lineation orientations and shear-senses. Furthermore, the channel flow model provides an explanation for the juxtaposition of the high-grade Quetico Subprovince against the low-grade Wawa Subprovince with subprovince-bounding shear zones recording dominantly dip-slip in multiple directions while maintaining greenschist facies metamorphic conditions. Accordingly, I interpret the SLSZ to have formed as a result of channel flow induced collapse and exhumation of the Quetico Subprovince adjacent to the Wawa Subprovince during regional shortening.

3.6. Summary and conclusions

Structural and kinematic data from the eastern SLSZ have first-order implications for assembly of the southern Superior Province. The eastern SLSZ is defined by a package of subvertical NE-striking L-S tectonites. Fm strikes NE and E across the study area with vertical, steep, moderate-SW, moderate-NE, and local gentle elongation lineation. Non-coaxial shear direction is sub-parallel to elongation lineation; SLSZ

tectonites record dominantly dip-parallel to oblique-slip and local strike-slip parallel to elongation lineation. Macro- and microscopic kinematic indicators record opposite shear-sense between outcrops and display no coherent spatial patterns. These structural and kinematic data indicate that the eastern SLSZ records broad dip- to oblique-slip shear event with L-S tectonites recording multiple shear-senses at greenschist facies metamorphic conditions. This assessment is consistent with structural and kinematic data from other Vermilion District shear zones.

Data presented in this study are inconsistent with sagduction-diapirism/crustal overturn models that require the formation of foliation triple-points and a consistent greenstone-down/granitoid-up shear-sense. The SLSZ does not appear to display a dome-and-keel like geometry and appears to be related to the adjacent Quetico/Wawa subprovince boundary. Sagduction-diapirism/crustal overturn processes operate on the scale of individual domes and keels and provide no viable explanation to account for the juxtaposition of low- and high-grade subprovinces.

Data presented herein are largely inconsistent with plate-tectonic models that require the formation of unidirectional dip-slip or strike-slip shear zones. As previously stated, the SLSZ does not record unidirectional slip, significant pressure/temperature gradients, or partitioned strike-slip shear zones. Furthermore, Archean crust was likely too weak to support rigid lithospheric plates.

Channel flow induced collapse during regional shortening is consistent with structural and kinematic data from the eastern SLSZ. Exhumation of high-grade gneissic material during channel flow induced collapse can account for the juxtaposition of the high-grade

Quetico Subprovince against the low-grade Wawa Subprovince. Such a mechanism may be applicable to other parts of the Superior Province. Deformation within greenstones adjacent to areas of exhumed high-grade material could produce the variability in elongation lineation orientation and shear-sense recorded within the SLSZ and other Vermilion District shear zones.

Table 1. Microstructural and kinematic data.

Sample	Location		Foliation	Lineation	Pitch (from W)	Shear-sense Indicators (from W)	Shear Sense	
	mE	mN					Dip-parallel	Strike-parallel
245A	620283	5321075	095, 84SW	Lc 278, 17	17	S-C; quartz/calcite strain fringes	N-side-up	right-lateral
302A	622442	5320061	123, 83SW	Lc 302, 18	18	S-C; quartz strain fringes	N-side-up	right-lateral
172A	617861	5322849	247, 76NW	Lc 261, 29	30	S-C-C'; shear band fragmented plagioclase clasts	S-side-up	left-lateral
87A	613838	5318550	235, 80NW	Lc 242, 34	35	S-C	N-side-up	right-lateral
171A	618159	5322887	226, 84NW	Ls 231, 35	35	S-C	N-side-up	right-lateral
126A	617807	5321309	260, 83NW	Lc 269, 52	53	S-C	N-side-up	right-lateral
221A	622918	5321234	274, 89N	Lc 276, 70	71	S-C; mantled σ -clasts; chlorite mats	N-side-up	
70A	611931	5317280	247, 82NW	Lc 271, 72	73	S-C; quartz strain fringes	N-side-up	
93A	614239	5319044	036, 72SE	Lc 165, 67	76	S-C; mantled σ -clasts	N-side-up	
205A	621634	5321464	264, 71N	Lc 315, 68	76	quartz strain fringes; kink bands	N-side-up	
85A	613720	5318515	044, 70SE	Lc 168, 66	77	S-C; quartz strain fringes	S-side-up	
149A	611262	5316729	066, 82SE	Lc 213, 75	78	S-C; quartz strain fringes	N-side-up	
318A	611943	5316845	068, 89SE	Lc 241, 80	80	S-C; quartz strain fringes; kink bands	S-side-up	
139A	612563	5317016	238, 84NW	Lc 273, 80	82	S-C; quartz strain fringes; muscovite mats	S-side-up	
197A	620229	5321388	275, 83N	Lc 332, 81	85	S-C; shear band fragmented plagioclase clasts	N-side-up	
237A	611950	5316087	240, 80NW	Lc 303, 79	85	S-C	N-side-up	
307A	612302	5315526	286, 81NE	Ls 348, 79	85	quartz strain fringes	N-side-up	
284A	625692	5321428	106, 52SW	Lc 203, 54	86	S-C; mantled σ -clasts; quartz strain fringes	S-side-up	
286A	625639	5321613	101, 70SW	Lc 193, 70	89	S-C	N-side-up	
102A	614186	5319421	231, 80NW	Ls 337, 79	93	S-C; quartz strain fringes	S-side-up	
178A	618635	5323152	054, 89SE	Ls 073, 85	94	quartz strain fringes	S-side-up	
165A	617648	5322285	230, 87NW	Ls 018, 84	95	quartz strain fringes	S-side-up	
191A	619760	5321489	090, 88S	Lc 113, 84	95	S-C; mantled σ -clasts; quartz strain fringes	N-side-up	
119A	616587	5321205	235, 83NW	Lc 008, 80	97	quartz strain fringes	S-side-up	
121A	616097	5320921	250, 87NW	Lc 047, 82	97	mantled σ -clasts; quartz strain fringes	S-side-up	
203A	621291	5321412	268, 56N	Lc 012, 55	99	S-C; shear band fragmented plagioclase clasts	S-side-up	
141A	611891	5316406	239, 84NW	Lc 031, 75	102	σ -clasts; muscovite halos	S-side-up	
104A	615607	5320548	245, 77NW	Lc 054, 75	104	S-C; mantled σ -clasts; quartz strain fringes	S-side-up	
290A	625003	5322133	109, 57S	Lc 170, 54	106	S-C-C'; quartz strain fringes	S-side-up	
109A	615625	5320625	055, 76SE	Lc 089, 65	110	S-C; quartz strain fringes	N-side-up	
276A	621275	5322169	282, 90	Lc 102, 70	110	S-C	N-side-up	
293A	623680	5322617	085, 60S	Ls 140, 54	110	S-C; mantled σ -clasts; quartz strain fringes	S-side-up	
100A	614048	5319319	225, 49NW	Ls 002, 37	125	S-C; mantled σ -clasts	S-side-up	left-lateral
133A	614424	5318996	043, 85SE	Ls 008, 43	136	S-C; kink bands	N-side-up	left-lateral
231A	620699	5321948	265, 86NW	Lc 081, 44	136	S-C; quartz strain fringes	S-side-up	right-lateral
272A	622377	5322431	271, 77N	Lc 078, 41	137	S-C; chlorite mats	N-side-up	left-lateral
153A	609547	5315335	086, 90	Lc 086, 35	145	quartz strain fringes; muscovite mats	S-side-up	right-lateral
55A	625185	5319354	283, 83N	Ls 098, 33	146	S-C; quartz strain fringes	S-side-up	right-lateral

Coordinates given in UTM Zone 15N, NAD 1983.

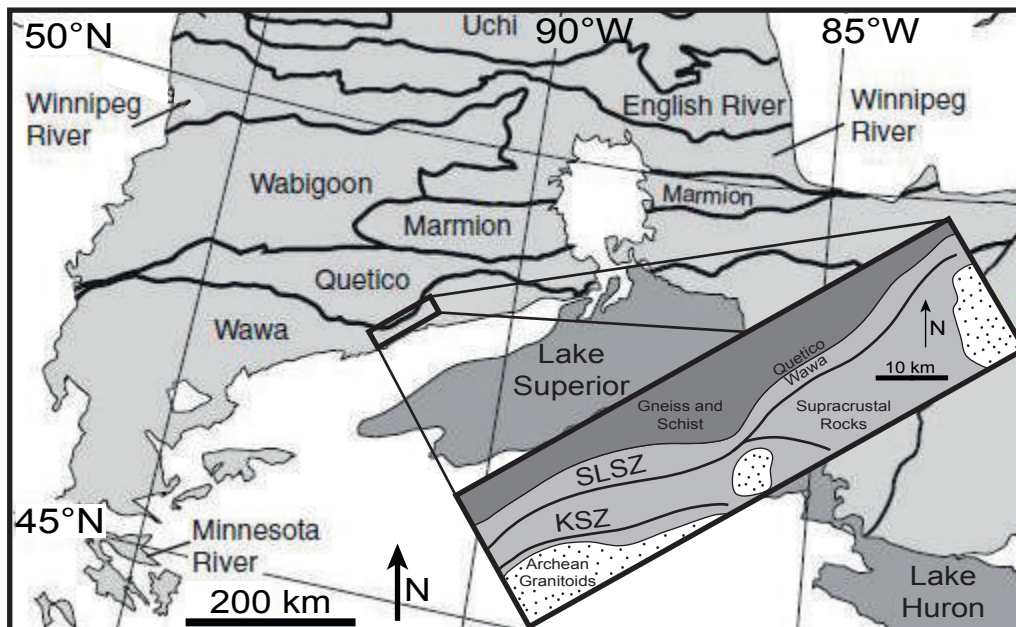


Figure 3.1. Selected subprovinces of the Superior Province. Black box marks the location of Figure 2. Inset: generalized geology of a portion of the Vermilion District showing the approximate location of the Shagawa Lake (SLSZ) and Kawishiwi (KSZ) shear zones. Modified from Thurston et al. (2008).

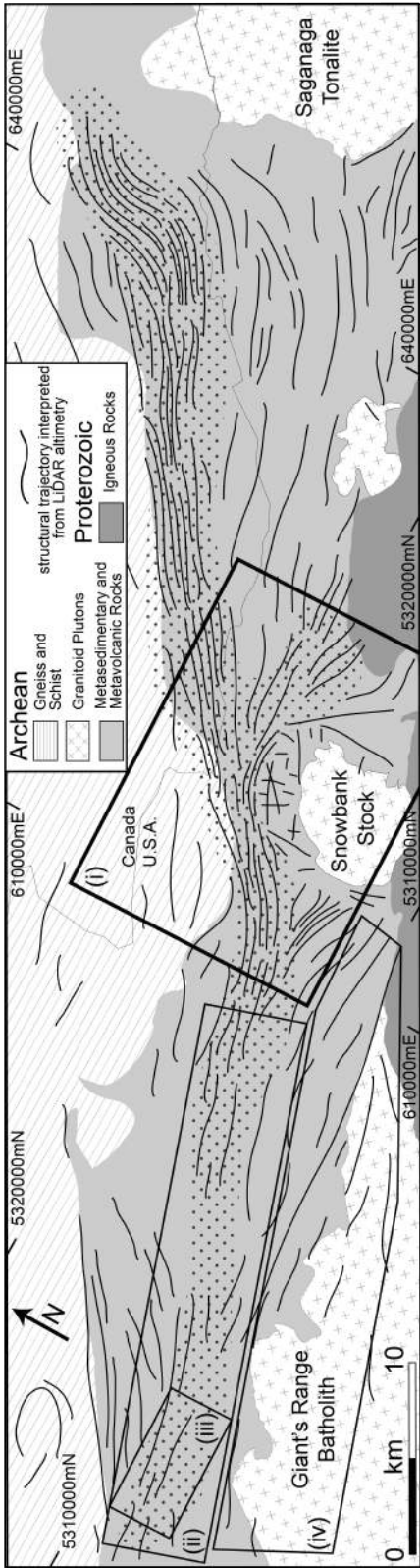


Figure 3.2. Regional geologic map of the SLSZ showing regional structural trajectories interpreted from LiDAR altimetry. Stippled area marks the interpreted extend of the SLSZ. Thick box marks the location of the study area and Figure 3. Thin boxes mark the location of previous studies. (ii) Erickson, 2008; 2010 (iii) Bauer and Bidwell, 1990; (iv) Goodman, 2008.

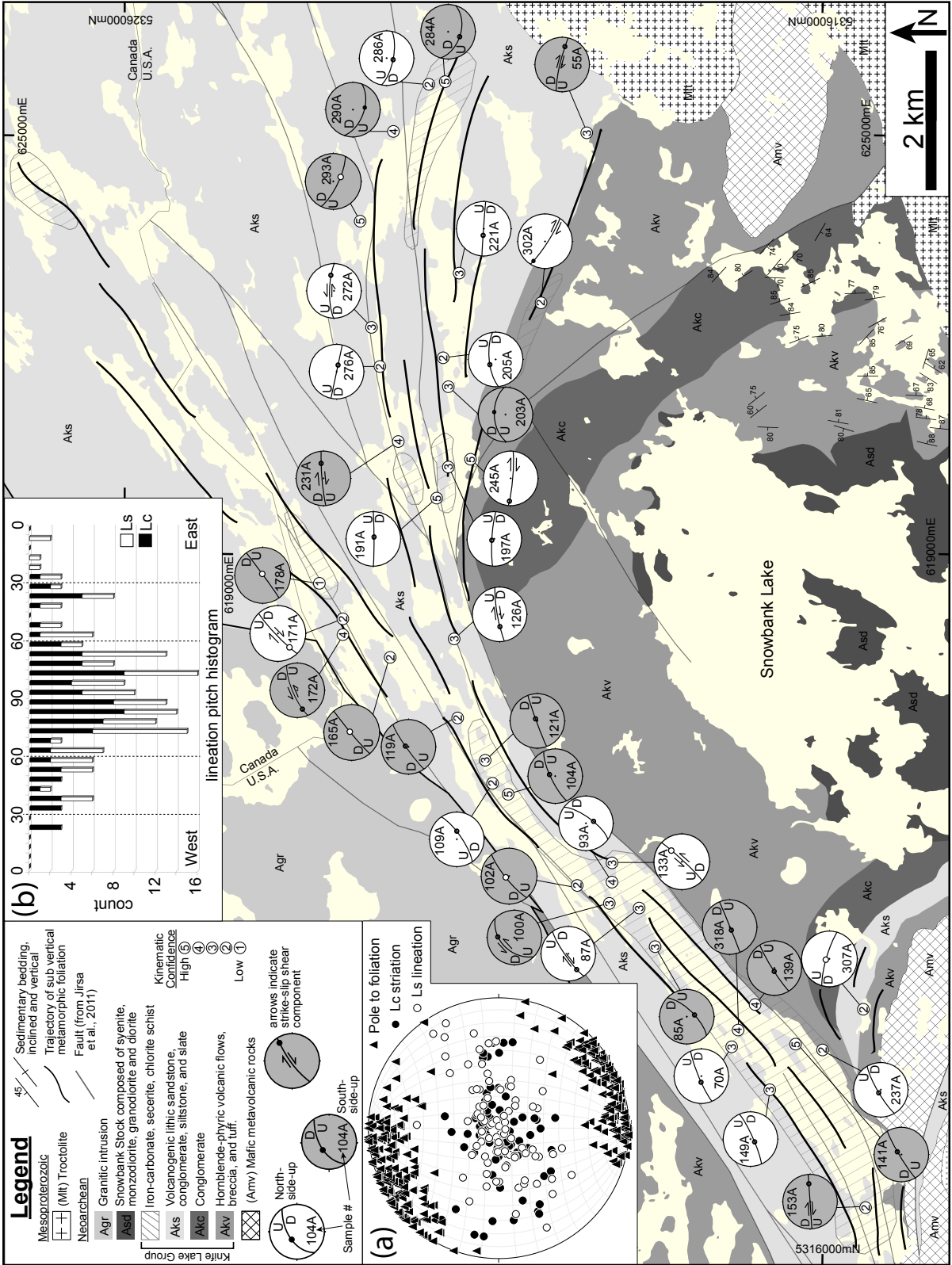


Figure 3.3. Geologic map of the SLSZ illustrating Fm trajectory (black lines), Lc and Ls orientation, and microstructural kinematic interpretations with sample numbers and kinematic confidence levels. Small lower-hemisphere equal-area stereonet record the orientation of Fm and Ls or Lc, respectively for individual samples. White stereonets represent N-side-up shear-sense and grey stereonets represent N-side-down shear-sense. (a) Orientations of poles to Fm (black triangles n=279), Lc (black circles n=94), and Ls (white circles n=88) shown on a lower-hemisphere equal-area stereonet. (b) Elongation lineation pitch histogram in degrees from west showing the distribution of Lc (black) and Ls (white) pitch values within Fm.

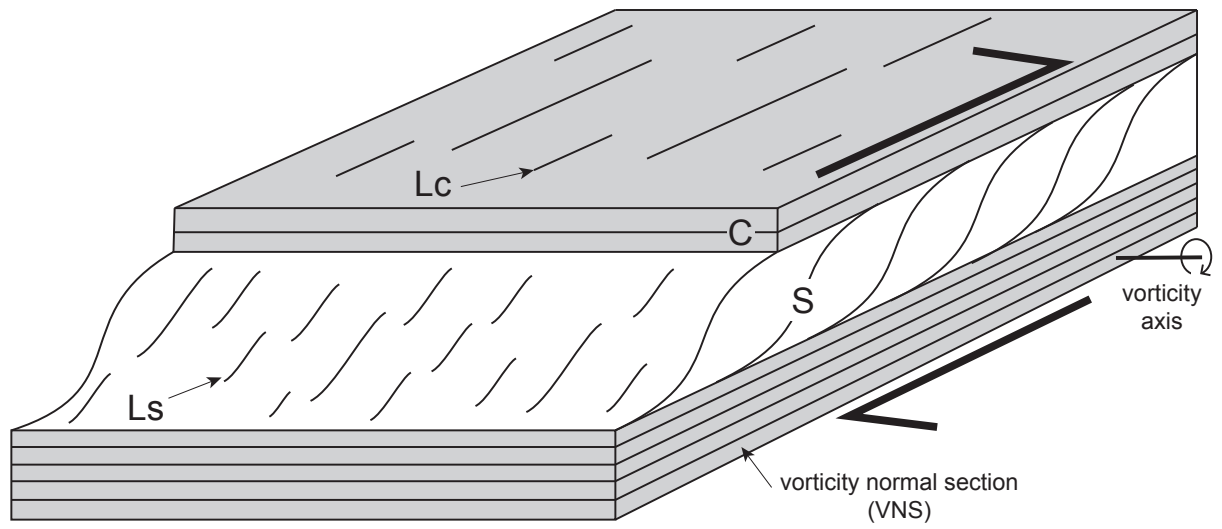


Figure 3.4. Schematic block diagram showing the structural elements of a L-S tectonite. Note the orientation of the vorticity-normal-section and vorticity axis relative to C, S, Ls, and Lc.

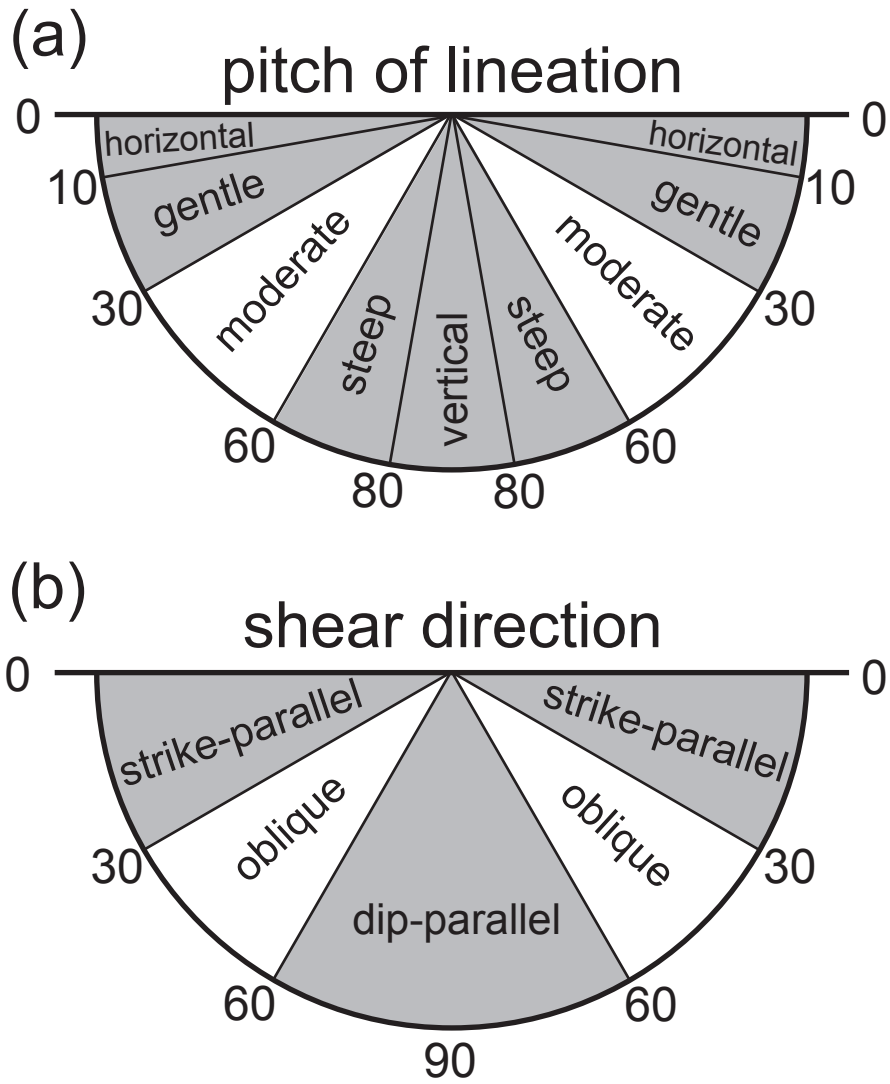


Figure 3.5. Diagram showing pitch domains for (a) elongation lineation and (b) non-coaxial shear direction. Pitch is measured in degrees from horizontal.

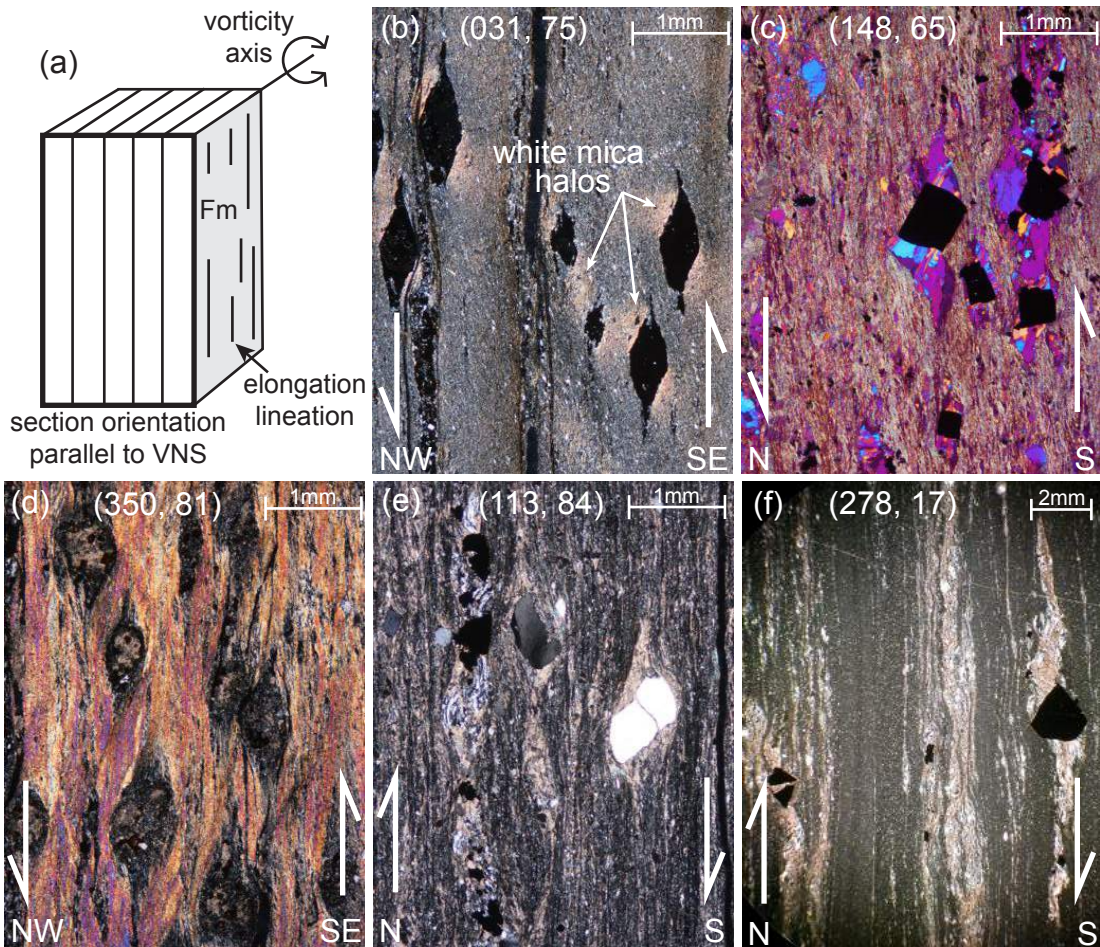


Figure 3.6. Photomicrographs of thin-sections cut parallel to the vorticity-normal-section (VNS). Trend and plunge of Ls or Lc included with each photomicrograph. (a) Schematic block diagram showing the orientation of the VNS relative to Fm and elongation lineation. (b) Photomicrograph showing sigmoidal iron-oxide replaced porphyroclasts with asymmetric white mica halos indicating a SE-up-shear. (c) Photomicrograph showing roughly rectangular pyrite grains with asymmetric quartz strain fringes indicating a S-up-shear. (d) Photomicrograph showing asymmetric sigmoidal porphyroclasts replaced by calcite within a fine-grain mica matrix. Micas define a S-C fabric indicating a NW-down-shear. (e) Photomicrograph showing pyrite grains with asymmetric quartz/calcite strain fringes within an S-C fabric indicating a N-up-shear. (f) Photomicrograph showing pyrite grains with asymmetric quartz/calcite strain fringes indicating a N-up-shear.

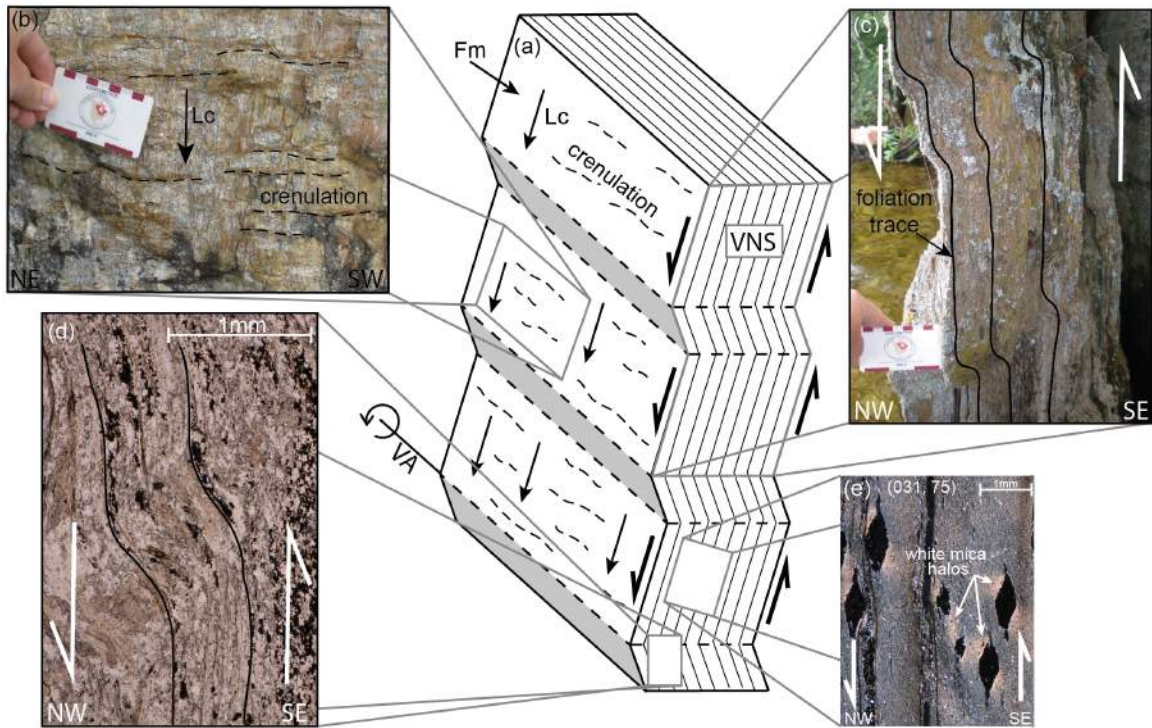


Figure 3.7. L-S tectonites showing a consistent NW-down shear-sense parallel to Lc. (a) Schematic block diagram of a L-S tectonite showing the relative orientations of Fm, Lc, crenulations, the vorticity-normal-section (VNS) vorticity axis (VA), and interpreted shear-sense. (b) Photograph looking into the Fm plane showing the relative orientations of Lc and crenulation indicating SE-down-shear. (c) Photograph looking into the plane normal to Fm and parallel to Lc (i.e. the VNS) of crenulation indicating SE-down-shear. (d) Photomicrograph looking into the VNS of crenulations filled with calcite indicating SE-down-shear. (e) Photomicrograph looking into the VNS of pyrite replaced porphyroclasts indicating SE-down-shear.

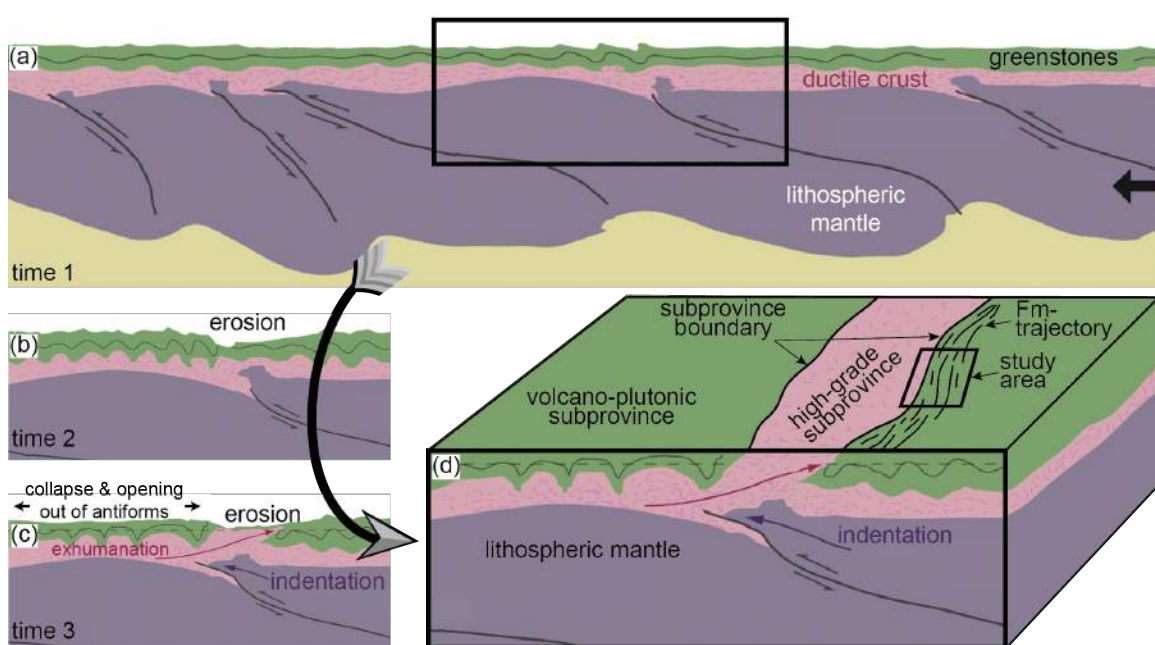


Figure 3.8. Evolution of Archean crust experiencing erosion-induced channel flow, exhumation of high-grade felsic gneisses, and development of arch and cusped folds in greenstones in the upper crust during imposed regional shortening. (a) Cross-section showing indentation of the lithospheric mantle into the ductile crust at time 1. Black box marks the location of (b), (c), and (d). (b) Enlarged subset of cross-section showing erosion of the greenstone sequence above the indented lithospheric mantle at time 2. (c) Exhumation of high-grade ductile crust at time 3. (d) Block diagram showing the juxtaposition of low-grade granite-greenstone and high-grade gneiss subprovinces in 3D. Fm-trajectories (black lines) represent L-S tectonite packages striking parallel to the subprovince boundary. Black box marks the interpreted location of our study area within the erosion-induced channel flow model. Modified from Harris et al. (2012).

4. Bibliography

- Bauer, R. L and Bidwell, M. E., 1990. Contrasts in the response to dextral transpression across the Quetico-Wawa subprovince boundary in northeastern Minnesota. *Canadian Journal of Earth Sciences* 27, 1521-1535.
- Bedard, J.H., Brouillette, P., Madore, L., Berclaz, A., 2003. Archean cratonization and deformation in the northern Superior Province, Canada: an evaluation of plate tectonic versus vertical tectonic models. *Precambrian Research*, 127, 61-87.
- Bedard, J.H., 2006. A catalytic delamination-driven model for coupled genesis of Archean crust and sub-continental lithospheric mantle. *Geochimica*, 70, 1188-1214.
- Berthé, D., Choukroune, P., Jegouzo, P., 1979. Orthogneiss, mylonite and non coaxial deformation of granites: the example of the South Armorican Shear Zone. *Journal of Structural Geology* 1 no. 1, 31-42.
- Card, K.D., 1990. A review of the Superior Province of the Canadian Shield, a product of Archean accretion. *Precambrian Research*, 48, 99-156.
- Chardon, D., Peucat, J., Jayananda, M., Choukroune, P., Fanning, C. M., 2002. Archean granite-greenstone tectonics at Kolar (South India): Interplay of diapirism and bulk inhomogeneous contraction during juvenile magmatic accretion. *Tectonics*, 21, no. 3, 1016.
- Chardon, D., Jayananda, M., Chetty, T.R.K., 2008. Precambrian continental strain and shear zone patterns: South Indian case. *Journal of Geophysical Research*, 113.

- Chardon, D., Gapais, D., Cagnard, F., 2009. Flow of ultra-hot orogens: A view from the Precambrian, clues for the Phanerozoic. *Tectonophysics*, 477, 105-118.
- Chown, E.H., Harrap, R., Moukhsil, A., 2002. The role of granitic intrusions in the evolution of the Abitibi belt, Canada. *Prec. Res.* 115, 291–310.
- Collins, B.C. and Sitar, N., 2008, Processes of costal bluff erosion in weakly lithified sands. *Pacifica, California, USA: Geomorphology*, v. 97, p. 483-501.
- Cowin, S.C., 1986. Wolff's law of trabecular architecture at remodeling equilibrium. *Journal of Biomechanical Engineering* 108, 83-88.
- Cruz-Orive, L.M., Karlsson, L.M., Larsen, S.E., Wainschtein, F., 1992. Characterizing anisotropy: a new concept. *Mm Microscopica Acta* 23, 75-76.
- Davidson, I., McCarthy, M., Powell, D., Torres, H.H.F., Santos, C.A., 1995. Laminar flow in shear zones: the Pernambuco Shear Zone, NE-Brazil. *Journal of Structural Geology*, 17, No. 2, 149-161.
- Davis, W.J., Sutcliffe, R.H., Trowell, N.F., 1988. Geochronological constraint on the tectonic evolution of a Late Archaean greenstone belt, Wabigoon subprovince, northwest Ontario, Canada. *Prec. Res.* 39, 171–191.
- de Wit, M.J., 1998. On Archean granites, greenstones, cratons and tectonics: does the evidence demand a verdict? *Precambrian Research*, 91, 181–226.
- Daigneault, R., Mueller, W.U., Chown, E.H., 2002. Oblique Archean subduction: accretion and exhumation of an oceanic arc during dextral transpression, Southern Volcanic Zone, Abitibi Subprovince Canada. *Prec. Res.* 115, 261–290.

- Desrochers, J.-P., Hubert, C., Ludden, J.N., Pilote, P., 1993. Accretion of Archean oceanic plateau fragments in the Abitibi greenstone belts, Canada. *Geology* 21, 451–454.
- Dimroth, E., Imreh, L., Goulet, N., Rocheleau, M., 1983a. Evolution of the south-central segment of the Archean Abitibi Belt, Quebec Part II tectonic evolution and geomechanical model. *Can J Earth Sci* 20, 1355-1373.
- Dimroth, E., Imreh, L., Goulet, N., Rocheleau, M., 1983b. Evolution of the south-central segment of the Archean Abitibi Belt, Quebec Part III plutonic and metamorphic evolution and geotectonic model. *Can J Earth Sci* 20 1374-1 388.
- Drury, S.A., Harris, N.B., Holt, R.W., Reeves-Smith, G.J., Wightman, R.T., 1984. Precambrian tectonics and crustal evolution on South India. *J. Geol.* 92, 3–20.
- Duretz, T., Kaus, B.J.P., Schulmann, K., Gapais, D., Kermarrec, J.-J., 2011. Indentation as an extrusion mechanism of lower crustal rocks: insight from analogue and numerical modelling, application to the Eastern Bohemian Massif. *Lithos* 124, 158–168.
- Dyess, J.E., Hansen, V.L., and Goscinak C., 2014. Determination of vorticity in Neoproterozoic tectonites. Submitted to *Precambrian Research*.
- Dyess, J.E., and Hansen, V.L., 2014. Application of LiDAR to resolving tectonic and glacial fabrics in glaciated terrain: An example from an Archean granite-greenstone belt, NE Minnesota. *Geosphere*, in press.

- Erickson, E., 2008. Structural and kinematic analysis of the Shagawa Lake shear zone, Superior Province, northeastern Minnesota. M.S. Thesis, University of Minnesota Duluth, MN.
- Erickson, E., 2010. Structural and kinematic analysis of the Shagawa Lake shear zone, Superior Province, northern Minnesota: implications for the role of vertical versus horizontal tectonics in the Archean. *Canadian Journal of Earth Sciences*, 47, 1463-1479.
- Godin, L., Grujic, D., Law, R.D., Searle, M.P., 2006. Channel flow, ductile extrusion and exhumation in continental collision zones: an introduction. In: Law, R.D., Searle, M.P., Godin, L. (Eds.), *Channel Flow, Ductile Extrusion and Exhumation in Continental Collision Zones*, Special Publication 268. Geological Society, London, pp. 1–23.
- Goodman, S., 2008. Structural and Kinematic Analysis of the Kawishiwi Shear Zone, Superior Province. M.S. Thesis, University of Minnesota Duluth, MN.
- Goodwin, A.M. and Ridler, R.H., 1970. The Abitibi orogenic belt In *Symposium on Basins and Geosynclines of the Canadian Shield*. Geol Surv Can Pap 70-40, 1-24.
- Gosciniak, C., 2014. Quartz fabric analysis of the Kawishiwi Shear Zone, NE Minnesota. M.S. Thesis, University of Minnesota Duluth, MN.
- Grujic, D., 2006. Channel flow and continental collision tectonics: an overview. In: Law, R.D., Searle, M.P., Godin, L. (Eds.), *Channel Flow, Ductile Extrusion and Exhumation in Continental Collision Zones*, Special Publication 268. Geological Society, London, pp. 25–37.

- Gruner J.W., 1941. Structural Geology of the Kinf Lake Area of Northeastern Minnesota. *Bull. Geol. Soc. Am.*, 52, 1577-1642.
- Hammer, S. 1992. Great Slave Lake shear zone, NW Canada: Mylonitic record of early continental convergence, collision, and indentation. *Journal of Structural Geology*, 14, No. 7, 757-773.
- Hansen, V.L. 1989. Structural and kinematic evolution of the Teslin suture zone, Yukon: record of an ancient transpressional margin. *Journal of Structural Geology*, 11(6): 717-733.
- Hansen, V.L., 1990. Collection and preparation of thin sections of oriented samples. *Journal of Geological Education*, vol. 38, 294-297.
- Harrigan, T.P., Mann, R.W., 1984. Characterization of microstructural anisotropy in orthotropic materials using a second rank tensor. *Journal of Materials Science* 19, 761-767.
- Harris, L.B., Godin, L., and Yakymchuk, C., 2012. Regional shortening followed by channel flow induced collapse: A new mechanism for “dome and keel” geometries in Neoproterozoic granite-greenstone terrains. *Precambrian Research*, 212-213, 139-154.
- Harris, L.B. and Bedard, J.H., 2014. Crustal Evolution and Deformation in a Non-Plate-Tectonic Archean Earth: Comparisons with Venus. In: *Evolution of Archean Crust and Early Life*, Springer Press.

- Haugerud, R.A., Harding, D.J., Johnson, S.Y., Harless, J.L., Weaver, C.S., Sherrod, B.L.,
2003. High-resolution topography of Puget Lowland, Washington-A Bonanza for
Earth Science: GSA Today, 13, no. 6, 4-10.
- Henderson, D.B., Ferrill, D.A., and Clarke, K.C., 1996, Mapping geological faults using
image processing techniques applied to hill-shade digital elevation models:
Proceedings of the IEEE Southwest Symposium on Image Analysis and
Interpretation, p. 240-245.
- Hirth, G., Tullis, J., 1992. Dislocation creep regimes in quartz aggregates. *Journal of
Structural Geology* 14, no. 2, 145-159.
- Hobbs, H.C. and Goebel, J.E., 1982. S-01 Geologic map of Minnesota, Quaternary
geology. Minnesota Geological Survey, <http://purl.umn.edu/60085>
- Hudleston, P.J., 1976. Early deformational history of Archean rocks in the Vermilion
District, Northeastern Minnesota. *Canadian Journal of Earth Sciences* 13, 579-
592.
- Hudleston, P.J., Schultz-Ela, D., Southwick, D. L., 1988. Transpression in an Archean
greenstone belt, northern Minnesota. *Canadian Journal of Earth Sciences* 25,
1060-1068.
- Jarrard, R.D., 1986. Terrane motion by strike-slip faulting of forearc slivers, *Geology*, 14,
780-783.
- Jirsa, M.A., Southwick, D.L., Boreboom, T.J., 1992. Structural evolution of Archean
rocks in the western Wawa subprovince, Minnesota: refolding of precleavage
nappes during D2 transpression. *Can J. Earth Sci* 29, 2146-2155.

- Jirsa, M.A., Boerboom, T.J., Chandler, V.W., Mossler, J.H., Runkel, A.C., Setterholm, D.R., 2011. S-21 Geologic Map of Minnesota-Bedrock Geology, Minnesota Geological Survey.
- Jirsa, M.A. and Miller Jr. J.D., 2004. Bedrock Geology of the Ely and Basswood Quadrangles, Northeast Minnesota. MNGS, M-148, scale 1:100,000
- Johnson, T., 2009. Structural, Kinematic, and Hydrothermal Fluid Investigation of the Gold-Bearing Murray Shear Zone, northeastern Minnesota. M.S. Thesis, University of Minnesota Duluth, MN.
- Karberg, S.M., 2009. Structural and kinematic analysis of the Mud Creek shear zone, northeastern Minnesota; implications for Archean (2.7 Ga) tectonics. M.S. Thesis, University of Minnesota Duluth, MN.
- Karlsson, L.M., Cruz-Orive, L.M., 1993. Characterizing structural anisotropy using the star volume distribution. In: Stereology in Materials Science: Demonstration of some methods. Unpublished PhD thesis, Royal Institute of Technology, Stockholm.
- Ketchum, R.A., Ryan, T., 2004. Quantification and visualization of anisotropy in trabecular bone. *Journal of Microscopy* 213, 158-171.
- Ketchum, R.A., 2005. Three-dimensional grain fabric measurements using high-resolution X-ray computed tomography. *Journal of Structural Geology* 27, 1217-1228.
- Kimura, G., Ludden, J. N., Desrochers, J.-P., and Hori, R., 1993. A model of ocean-crust accretion for the Superior Province, Canada. *Lithos*, 30, 337-355.

- Kusky, T.M., 1998. Tectonic setting and terrane accretion of the Archean Zimbabwe craton. *Geology* 26, 163–166.
- Kusky, T.M., and Polat, A. 1999., Growth of granite–greenstone terranes at convergent margins, and stabilization of Archean cratons. *Tectonophysics*, 305, 43–73.
- Langford, F.F. and Morin, M.A. 1976. The development of the Superior Province of Northwestern Ontario by merging island arcs. *Am J Sci* 276, 1023-1034.
- Launeau, P., Robin, P.-Y.F., 1996. Fabric analysis using the intercept method. *Tectonophysics* 267, 91-119.
- Lin, S., Williams, P.F., 1992. The origin of ridge-in-groove slickenside striae and associated steps in an S-C mylonite. *Journal of Structural Geology* 14, 315-321.
- Lin, S., Jiang, D., Williams, P.F., 1998. Transpression (or transtension) zones of triclinic symmetry: natural example and theoretical modeling. *Geo Soc London Special Publications* 135, 41-457.
- Lin, S., 2005. Synchronous vertical and horizontal tectonism in the Neoproterozoic: Kinematic evidence from a synclinal keel in the northwestern Superior craton, Canada. *Precambrian Research*, 135, 181-194.
- Lin, S., Jiang, D., Williams, P., 2007. Importance of differentiating ductile slickenside striations from stretching lineations and variation of shear direction across a high-strain zone. *Journal of Structural Geology*, 29, 850-862.
- Lister, G.S. and Hobbs, B.E., 1980. The simulation of fabric development during plastic deformation and its application to quartzite: the influence of deformation history. *Journal of Structural Geology*, 2, 355-371.

- Lowe, D.R., 1999. Geologic evolution of the Barberton greenstone belt and vicinity. In: Lowe, D.R., Byerly, G.R. (Eds.), *Geologic Evolution of the Barberton Greenstone Belt, South Africa*, Geol. Soc. Am. Spec. Paper, vol. 329, pp. 87–312.
- Ludden, J.N., Hubert, C., Gariépy, C., 1986. The tectonic evolution of the Abitibi greenstone belt of Canada. *Geol Mag* 123, 153-166.
- McNab, W.H. and Avers, P.E., 1994. *Ecological Subregions of the United States*, section description. USDA Forest Service, Ecosystem Management.
- Mulvey, L., Ross, C., Zeitler, J., Pendleton, M., McCarthy, A., Copp, L., Nowak, R., Hudak, G., Peterson, D., 2009. *Bedrock Geologic Map of the Disappointment Lake Area, Lake County, Northeastern Minnesota*, Precambrian Research Center Map Series, PRC/MAP-2009-02.
- Notebaert, B., Verstraeten, G., Govers, G., and Poesen, J., 2009, Qualitative and quantitative applications of LiDAR imagery in fluvial geomorphology: *Earth Surface Processes and Landforms*, v. 34, p. 217-231.
- Odgaard, A., Kabel, J., van Reitbergen, B., Dalstra, M., Huiskes, R., 1997. Fabric and elastic principal directions of cancellous bone are closely related. *Journal of Biomechanics* 30, 487-495.
- Parmenter, A.C., Lin, S., and Corkery, M.T., 2006. Structural evolution of the Sross Lake greenstone belt in the northwestern Superior Province, Manitoba: Implications for relationship between vertical and horizontal tectonism. *Canadian Journal of Earth Sciences*, 43, 767-787.
- Passchier, C.W., 1998. Monoclinic model shear zones. *Journal of Structural Geology*. 20

(8): 1121-1137.

Passchier, C.W., Trouw, R.A.J., 2005, *Microtectonics* Second Edition Springer: Berlin.

Pavlis, T.L. and Bruhn, R.L., 2011. Application of LIDAR to resolving bedrock structure in areas of poor exposure: An example from the STEEP study area, southern Alaska. *GSA Bulletin*, 123, 206-217.

Percival, J. A., and Williams, H. R., 1989. Late Archean Quetico accretionary complex, Superior Province, Canada. *Geology*, 17, 23-25.

Percival, J.A., McNicoll, V., Brown, J.L., Whalen, J.B., 2004. Convergent margin tectonics, central Wabigoon subprovince, Superior Province, Canada. *Prec. Res.* 132, 213–244.

Perchuk, L.L. and Gerya, T.V., 2011. Formation and evolution of Precambrian granulite terranes: A gravitational redistribution model. *Geological Society of America Memoirs*, 207, 289-310.

Rey, P.F., and Coltice, N., 2008. Neoproterozoic lithospheric coupling of Earth's geochemical reservoirs. *Geology*. 36, No. 8, 635-638.

Roering, J.J., 2008, How well can hill-slope evolution models explain topography? Simulating soil transport and production with high-resolution data: *Geological Society of America Bulletin*, v. 120, p. 1248-1262.

Sanders C.W., 1929, A composite stock at Snowbank Lake in northeastern Minnesota. *Journal of Geology*, 37, 135-149.

Schmid, S.M., Casey, M., 1986. Complete fabric analysis of some commonly observed quartz c-axis patterns. In: Hobbs, B.E. & Heard, H.C. (eds) *Mineral and Rock*

- Deformation: Laboratory Studies – The Patterson Volume. American Geophysical Union, Geophysical Monograph, 36, 263-286.
- Schmidt, N.H., and Olesen, N.O., 1989. Computer-aided determination of crystal lattice orientation from electron channeling patterns in the SEM. *Canadian Mineralogist* 27, 15-22.
- Schultz-Ela, D.D. and Hudleston, P.J., 1991. Strain in an Archean greenstone belt of Minnesota. *Tectonophysics* 190, 233-268.
- Sharp, R.P., 1953. Glacial Features of Cook County, Minnesota, *American Journal of Science*, 251, 855-883.
- Sims, P.K., 1976. Early Precambrian tectonic-igneous evolution in the Vermilion District, northeastern Minnesota. *Geol. Soc. Am. Bull.* 87, 379-389.
- Sizova, E., Gerya, T., Brown, M., and Perchuk, L.L., 2010. Subduction styles in the Precambrian: Insight from numerical experiments. *Lithos*, 116, 209-229.
- Sleep, N., 1992. Archean plate tectonics: what can be learned from continental geology?. *Canadian Journal of Earth Sciences*, 29, 2066-2071.
- Smit, T.H., Schneider, E., Odgaard, A., 1998. Star length distribution: a volume-based concept for the characterization of structural anisotropy. *Journal of Microscopy* 191, 249-257.
- Stipp, M., Stunitz, H., Heilbronner, R., and Schmid, S. M., 2002, The eastern Tonale fault zone: a ‘natural laboratory’ for crystal plastic deformation of quartz over a temperature range from 250 to 700 °C: *Journal of Structural Geology* 24, 1861–1884.

- Sullivan, W.A., Beane, R.J., Beck, E.N., Fereday, W.H., Roberts-Pierel, A.M., 2011. Testing the transpressional hypothesis in the western part of the Cheyenne belt, Medicine Bow Mountains, southeastern Wyoming. *Rocky Mountain Geology* 46, no. 2, 111-135.
- Sylvester, P.J., Attoh, K and Schulz, K.J., 1987. Tectonic setting of late Archean bimodal volcanism in the M1- chipicoten (Wawa) greenstone belt, Ontario. *Can J Earth Sci* 24, 1120-1134.
- Talbot, C.J., 1973. A plate tectonic model for the Archean crust. *Philos Trans Soc London* 273, 413- 427.
- Thurston, P.C., Ayer, J.A., Goutier, J., Hamilton, M.W., 2008. Depositional Gaps in Abitibi Greenstone Belt Stratigraphy: A Key to Exploration for Syngenetic Mineralization, *Economic Geology*, 103, 1097-1134.
- Wallace, J., Morris, B., and Howarth, P., 1993, Identifying structural trend with fractal dimension and topography: *Geology*, v. 34, p. 901-904.
- Whitehouse, W.J., 1974. The quantitative morphology of anisotropic trabecular bone. *Journal of Microscopy* 101, 153-168.
- Williams, H., 1990. Subprovince accretion tectonics in the south-central Superior Province. *Can. J. Earth Sci.* 27, 570–581.
- Windley, B.F. 1984. *The Evolving Continents*. 2nd ed. Wiley, London.
- Wolf, D. E., 2006. The Burntside Lake and Shagawa/Knife Lake shear zones: Deformation kinematics, geochemistry and geochronology; Wawa Subprovince, Ontario, Canada. Masters Thesis, Washington State University.

Xypolias, P., 2010. Vorticity analysis in shear zones: A review of methods and applications. *Journal of Structural Geology* 32, 2072-2092.

Zhou, Q., 1992, Relief shading using digital elevation models: *Computers and Geoscience*, v. 18, No. 8, p. 1035-1045.